

Process and Material Modifications to Enable New Material for Material Extrusion  
Additive Manufacturing

Callie Elizabeth Zawaski

Dissertation submitted to the faculty of the Virginia Polytechnic Institute and State  
University in partial fulfillment of the requirements for the degree of

Doctor of Philosophy  
In  
Mechanical Engineering

Christopher B Williams  
Timothy E Long  
Zhiting Tian  
Abby R Whittington

May 5, 2020  
Blacksburg, VA

Keywords: Additive Manufacturing; 3D Printing; Fused Filament Fabrication;

Copyright

# Process and Material Modifications to Enable New Material for Material Extrusion Additive Manufacturing

Callie Elizabeth Zawaski

## ABSTRACT

The overall goal of this work is to expand the materials library for the fused filament fabrication (FFF) material extrusion additive manufacturing (AM) process through innovations in the FFF process, post-process, and polymer composition. This research was conducted at two opposing ends of the FFF-processing temperature: low processing temperature ( $<100\text{ }^{\circ}\text{C}$ ) for pharmaceutical applications and high processing temperatures ( $>300\text{ }^{\circ}\text{C}$ ) for high-performance structural polymer applications. Both applications lie outside the typical range for FFF ( $190\text{-}260\text{ }^{\circ}\text{C}$ ). To achieve these goals, both the material and process were modified.

Due to the low processing temperature requirements for pharmaceutical active ingredients, a water-soluble, low melting temperature material (sulfonated poly(ethylene glycol)) series was used to explore how different counterions affect FFF processing. The strong ionic interaction within poly(PEG8k-co-CaSIP) resulted in the best print quality due to the higher viscosity ( $10^5\text{ Pa}\cdot\text{s}$ ) allowing the material to hold shape in the melt and the high-nucleation producing small spherulites mitigating the layer warping. Fillers were then explored to observe if an ionic filler would produce a similar effect. The ionic filler (calcium chloride) in poly(PEG8k-co-NaSIP) altered the crystallization kinetics, by increasing the nucleation density and viscosity, resulting in improved printability of the semi-crystalline polymer.

A methodology for embedding liquids and powders into thin-walled capsules was developed for the incorporation of low-temperature active ingredients into water-soluble materials that uses a higher processing temperature than the actives are compatible with. By tuning the thickness of the printed walls, the time of internal liquid release was controlled during dissolution. This technique was used to enable the release of multiple liquids and powders at different times during dissolution.

To enable the printing of high-temperature, high-performance polymers, an inverted desktop-scale heated chamber with the capability of reaching over  $300\text{ }^{\circ}\text{C}$  was developed for FFF. The design was integrated onto a FFF machine and was used to successfully print polyphenylsulfone which resulted in a 48% increase in tensile strength (at  $200\text{ }^{\circ}\text{C}$ ) when compared to printing at room temperature.

Finally, the effects of thermal processing conditions for printing ULTEM<sup>®</sup> 1010 were studied by independently varying the i) nozzle temperature, ii) environment temperature, and iii) post-processing conditions. The nozzle temperature primarily enables flow through the nozzle and needs to be set to at least  $360\text{ }^{\circ}\text{C}$  to prevent under extrusion. The environment temperature limits the part warping, as it approaches  $T_g$  ( $217\text{ }^{\circ}\text{C}$ ), and improves the layer bonding by decreasing the rate of cooling that allows more time for polymer chain entanglement. Post-processing for a longer time above  $T_g$  (18 hrs at  $260\text{ }^{\circ}\text{C}$ ) promotes further entanglement, which increases the part strength (50% increase in yield strength); however, the part is susceptible to deformation. A post-processing technique was developed to preserve the parts' shape by packing solid parts into powdered salt.

# Process and Material Modifications to Enable New Material for Material Extrusion Additive Manufacturing

Callie Elizabeth Zawaski

## GENERAL AUDIENCE ABSTRACT

Fused filament fabrication (FFF) is the most widely used additive manufacturing (also referred to as 3D printing) process in industry, education, and for hobbyists. However, there is a limited number of materials available for FFF, which limits the potential of using FFF to solve engineering problems. This work focuses on material and machine modifications to enable FFF for use in both pharmaceutical and structural applications. Specifically, many pharmaceutical active ingredients require processing temperatures lower than what FFF typically uses. A low-temperature water-soluble material was altered by incorporating salt ions and ionic fillers separately. The differences in the printability were directly correlated to the measured variations in the viscosity and crystallization material properties. Alternatively, a technique is presented to embed liquids and powders into thin-walled, water-soluble printed parts that are processed using typical FFF temperatures, where the embedded material remains cool. The release time of the embedded material during dissolution is controlled by the thickness of the capsule structure. For structural applications, a machine was developed to allow for the processing of high-performance, high-temperature polymers on a desktop-scale system. This system uses an inverted heated chamber that uses natural convection to be able to heat the air around the part and not the electric components of the machine. The heated environment allows the part to remain at a higher temperature for a longer time, which enables a better bond between printed layers to achieve high-strength printed parts using high-performance materials. This machine was used to characterize the thermal processing effect for printing the high-performance polymer ULTEM<sup>®</sup> 1010. The nozzle temperature, environment temperature, and post-processing were tested where i) a higher nozzle temperature (360 °C) increases strength and prevents under extrusion, ii) a higher environment temperature ( $\geq 200$  °C) increases the strength by slowing cooling and decreases warping by limiting the amount of shrinkage that occurs during printing, and iii) post-processing in powdered salt (18 hrs at 260 °C) increases part strength (50%) by allowing the printed roads to fuse.

## Acknowledgments

I consider myself fortunate to have had the opportunity to be a Ph.D. student at Virginia Tech Mechanical Engineering DREAMS Lab. My parents have been a huge support in my childhood not limiting my interests or creativity which have allowed me to gain the confidence to enter the world of engineering. I want to thank my grandparents Dr. James P Rodman and Margaret (Maggie) Rodmen for the love and inspiration given to me. My fiancé Joseph Kubalak has also provided support, both scientifically and emotionally, as we have gone through this long process together.

I would like to recognize and thank my committee chair, Dr. Christopher B. Williams. Dr. Williams is appreciated for establishing the DreamVendor project which introduced me to 3D printing and began my interest and inspired my research for additive manufacturing (AM). He has served as a knowledgeable mentor in AM technology, presentation skills, and scientific editing. I would also like to thank him for allowing me to try my crazy ideas that sometimes work and sometimes fail, but always gaining knowledge I could not have gotten any other way.

I would like to acknowledge my committee for the collaboration and support in this work. Dr. Timothy Long is acknowledged for collaboration in chemical synthesis of materials and materials expertise. Dr. Zhiting Tian is acknowledged for collaboration and knowledge in thermal conductivity. Finally, Dr. Abby Whittington is acknowledged for collaboration in the incorporation of active ingredients and expertise in dissolution.

A special acknowledgment goes to the Center for Enhancement of Engineering Diversity (CEED) at Virginia Tech, specifically to Dr. Bevelee Watford and Susan Arnold-Christian. CEED has provided support to me as a student in my undergraduate career as well as financial support and leadership experience in my graduate career.

Finally, I would like also like to thank and acknowledge the many people who helped with this work: Camden Chatham for teaching me about polymer characterization, his collaboration in printing new polymers and for helping with I-Corps, Viswanath Meenakshisundaram for participating in the I-Corps program with me, Emily Wilts for material supply and analysis of the SPEGs and fillers, Yifeng Lin for discussions on extrusion and help with SEM, Benjamin Tyler White for collaborative work on PEU, Xi Chen for collaborative work on PEG<sub>4K</sub>-diCyA, Hadi Miyanaji for help and advice using high-temperature processing, Jaideep Pandit for helping access and assist with ANSYS, Dr. Andre Stevenson for collaborative work incorporating active ingredients to SPEG, Jack Bryant for discussions on material characterizations and powder packing, John Will for help with SEM, Chen Li for thermal conductivity measurements, the team of Jake Fallon, Eric Gilmer, Arit Das, and Cailean Pritchard for work with high performance polymers, Dr. Allison Pekkanen for collaborative work developing the SPEG series, Evan Margaretta for preliminary work in initial work with printing new materials, Zane Haley for materials characterization, Dr. Robert Moore for teaching crystallization kinetics, Dr. Michael Bortner for teaching about rheology, Dr. Thomas Staley for training materials characterization, the Materials Science and Engineering Lab for access to use their machines, equipment, and training, the Macromolecule's Innovation Institute (MII) at Virginia Tech for creating the interdisciplinary team that made this work possible, and the DREAMS Lab for the collaborations and discussions of scientifically (and not scientifically) related topics.

# Table of Contents

Abstract .....	ii
General Audience Abstract.....	iii
Acknowledgments.....	iv
List of Figures.....	ix
List of Tables .....	xiv
1. Introduction.....	1
1.1 Material extrusion additive manufacturing .....	1
1.2 Research gap.....	1
1.2.1 Printing personalized medicine .....	2
1.2.2 Printing a high-performance polymer .....	2
1.3 Overall research goal.....	2
1.4 Research Question 1 and Hypothesis.....	3
1.4.1 Impact.....	4
1.5 Research Question 2 and Hypothesis.....	4
1.5.1 Impact.....	5
2. Tuning the material properties of a water-soluble ionic polymer using different counterions for material extrusion additive manufacturing .....	6
2.1 Introduction .....	6
2.2 Methods.....	7
2.2.1 Materials Material Preparation and Synthesis .....	7
2.2.2 Material Characterization.....	8
2.2.3 Print Quality .....	9
2.3 Results and Discussion.....	11
2.3.1 Material Properties.....	11
2.3.2 Effects of counter ions on printed tensile properties .....	17
2.3.3 Effects of counter ions on printability.....	19
2.4 Conclusions and Future Work .....	21
3. Using different fillers to tune material properties of an ion containing semi-crystalline poly(ethylene glycol) for fused filament fabrication additive manufacturing processing .....	22
3.1 Introduction .....	22
3.2 Methods.....	23
3.2.1 Materials.....	23
3.2.2 Thermal Analysis .....	24

3.2.3	Oscillatory Rheology .....	24
3.2.4	Crossed-Polarized Light Microscopy .....	24
3.2.5	Processing.....	24
3.2.6	Print Quality .....	25
3.3	Results and Discussion.....	26
3.3.1	Thermal Characterization.....	26
3.3.2	Rheological Properties .....	27
3.3.3	Crystallization.....	28
3.3.4	Tensile.....	32
3.3.5	Printing Quality .....	33
3.4	Conclusion.....	35
4.	Embedding of liquids into water soluble materials via additive manufacturing for timed release.....	37
4.1	Introduction .....	37
4.2	Embedding into Fused Filament Fabricated Parts .....	38
4.2.1	Design Considerations for Embedding Liquids into Fused Filament Fabricated Parts	39
4.3	Methods.....	40
4.3.1	Materials.....	41
4.3.2	Filament Processing .....	42
4.3.3	Fused Filament Fabrication Printing.....	42
4.3.4	Liquid Embedding .....	42
4.3.5	Powder Embedding.....	43
4.3.6	Test Specimen Geometry Design .....	43
4.3.7	Dissolution measurement .....	44
4.4	Results/Discussion .....	45
4.4.1	Dissolution vs wall thickness .....	45
4.4.2	Controlling release .....	47
4.5	Summary & Future Work.....	51
5.	Design of a low-cost, high-temperature build environment for a fused filament fabrication .	52
5.1	High Temperature Fused Filament Fabrication.....	52
5.1.1	Introduction .....	52
5.1.2	Review of existing high temperature environment machines .....	52
5.1.3	Objective .....	54

5.2 Design Problem of a Heated Environment System .....	54
5.2.1 Design Considerations/Customer Needs .....	54
5.2.2 Discussion of Design Tradeoffs.....	55
5.3 Inverted Printer Design for a High-Temperature Build Environment .....	56
5.3.1 Design .....	56
5.3.2 Verification via Computational Fluid Dynamics Model.....	57
5.4 Experimental Validation .....	59
5.4.1 Method .....	60
5.4.2 Results .....	61
5.5 Summary .....	66
6. The effect of Fused Filament Fabrication Thermal Processing Conditions on the mechanical strength and dimensional accuracy on Ultem 1010 .....	68
6.1 Introduction .....	68
6.1.1 Thermal Processing Effects of FFF parts.....	68
6.1.2 Thermal Post-Processing Effects on FFF Parts .....	69
6.2 Methods.....	69
6.2.1 Materials and Thermal Characterization .....	70
6.2.2 Processing.....	70
6.2.3 Characterization .....	74
6.3 Results and Discussion.....	77
6.3.1 Thermal Characterization .....	77
6.3.2 Effects of Nozzle Temperature on Processability and Strength .....	78
6.3.3 Effects of Environment Temperature on Strength and Curling.....	81
6.3.4 Effects of Post-Processing Conditions on Strength and Dimensional Accuracy ....	84
6.3.5 Light Absorption as an Indicator of Part Strength.....	89
6.4 Summary and Future Work .....	91
7. Summary.....	92
7.1 Summary of Research .....	92
7.1.1 Research Question 1 .....	92
7.1.2 Research Question 2 .....	93
7.2 Publications .....	95
7.3 Contributions .....	97
7.3.1 Intellectual merits .....	97
7.3.2 Broader impacts .....	97

7.4 Future Work.....	98
7.4.1 Pharmaceutical.....	98
7.4.2 Tailored Dissolution.....	98
7.4.3 Structure-process-property relationship .....	99
7.4.4 Development.....	99
7.4.5 Modeling high-temperature FFF.....	99
7.4.6 Designing and Building the Inverted FFF system .....	99
7.4.7 Further investigation .....	99
References .....	101

## List of Figures

Figure 1. Melt transesterification of poly(ethylene glycol) and sulfonated isophthalate (SIP) to yield ion-containing poly(ether ester)s and the ion exchange of poly(PEG <sub>8k</sub> -co-NaSIP) to a range of counterions through dialysis [24].	8
Figure 2: Schematic of printed single-road prisms for evaluating layer bond strength. Lighter lines illustrate layered structure. Dashed lines show outline of tensile bar specimen punch for (a) XY tensile specimens and (b) Z tensile specimens.	10
Figure 3: The features used to test the various elements of printability of the different counterion SPEGs.	11
Figure 4: DSC traces depicting the cooling after the first heat and the second heat heating at 10 °C/min with 100 °C/min cooling of the SPEG materials containing four different counterions. Exothermal up.	12
Figure 5: Oscillatory rheology of the SPEG materials containing four different counterions using parallel plates at constant temperature 70 °C and 1% strain.	14
Figure 6: Oscillatory rheology of the SPEG materials containing four different counterions using parallel plates at 1% strain and 1 rad/s (near zero shear) temperature step down from 70 °C to 50 °C.	14
Figure 7: Thermal diffusivity of the SPEG materials containing four different counterions using laser-induced transient thermal grating (TTG) technique.	15
Figure 8: Images of SPEGs containing the four different counterions taken using polarized light microscopy. The timestamps shown are referenced to the first observed spherulite. The total time from observed spherulitic formation until impingement was evenly divided into four parts; images are shown at each time increment. The scale bar shows 150 μm.	16
Figure 9: The spherulitic growth rate of three of the SPEG polymers containing different counterions. Poly(PEG <sub>8k</sub> -co-CaSIP) is not shown because the spherulites are too small for quantitative image analysis.	16
Figure 10. Crystallization half-time as a function of isothermal temperature for SPEG containing four different counterions.	17
Figure 11: Evaluation of the tensile strength for poly(PEG <sub>8k</sub> -co-NaSIP), poly(PEG <sub>8k</sub> -co-CaSIP), poly(PEG <sub>8k</sub> -co-ZnSIP), poly(PEG <sub>8k</sub> -co-MgSIP) for melt pressed, and printed in a horizontal (xy) and vertical (z) orientation by a) the elastic modulus, b) the ultimate tensile strength, and c) the elongation at break.	18
Figure 12: Part printed out of SPEG containing four different counterions using filament material extrusion. All parts were printed at 70 °C at 5 mm/s. (Note: *were printed at 2 mm/s rather than 5 mm/s).	19
Figure 13: The one step chemical synthesis of poly(PEG <sub>8k</sub> -co-NaSIP) and two step chemical synthesis of poly(PEG <sub>8k</sub> -co-CaSIP) [24].	22
Figure 14: DSC for the base polymer, poly(PEG <sub>8k</sub> -co-NaSIP), and target polymer property, poly(PEG <sub>8k</sub> -co-CaSIP), and the poly(PEG <sub>8k</sub> -co-NaSIP) containing different fillers. Exotherm up.	27

Figure 15: Oscillatory rheology of the SPEG materials (a) compared to the poly(PEG <sub>8k</sub> -co-NaSIP) with 5 wt% filler material at 1% strain and (b) the poly(PEG <sub>8k</sub> -co-NaSIP) with different wt% of the CaCl <sub>2</sub> at 1% strain and near zero shear ~0.1 rad/sec (n=1). .....	28
Figure 16: Crystallization of the polymers cooling from 70 °C to 25 °C shown at 4 different time stamps using cross polarized light microscopy on an Olympus BX51 microscope with a linkam hot stage. The scale bar shows 100 μm. ....	30
Figure 17: The spherulite growth measured from microscope images at different instances in time (n=1). ....	31
Figure 18. Crystallization halftimes versus isothermal temperature for four filled materials and unfilled control (n=1). ....	32
Figure 19: Tensile properties of the sPEG materials in comparison to the poly(PEG <sub>8k</sub> -co-NaSIP) with fillers looking at both pressed films and printed tensile properties (n=5). ....	33
Figure 20: Printed features to compare the difference between the different materials printability. (*Printed slower at 2 mm/sec) .....	35
Figure 21: The general process for embedding where a) a part is designed with an internal void, b) the part is partially printed, c) the liquid is inserted during printing, and d) the embedded component is enclosed inside of the printed part. (Based on Meisel’s steps for embedding [98]) .....	39
Figure 22: A process diagram for 1-2) creating filament, 3) printing the filament into a hollow capsule geometry 4) in-situ embedding a liquid into the capsule and 5-6) timed dissolution of the printed capsule. ....	41
Figure 23: The thermal characterization of Mowiflex using A) TA Instruments TGA Q500 at 10 °C/min from 23 °C to 550 °C and B) TA Instruments Q2000 DSC from -80 °C to 200 °C second heat cycle at a heating rate of 10 °C/min. ....	42
Figure 24: The assumed cross-section shape of stacked printed roads, where the top gray box represents the assumed shape, for A) one road thick and B) two roads thick printed walls .....	44
Figure 25: The outline of the continuous toolpath for each layer of the parts with walls that are A) one road thick, B) two roads thick, and C) three roads thick. D) Shows a multi-chamber part containing two chambers that are one and two roads thick. (the top and bottom layers are infilled). ....	44
Figure 26: An example of a dissolution image with the color swatch and blank swatch RGB values used to detect the release time. ....	45
Figure 27: The time of release for the capsules with wall thicknesses of A) one road, B) two roads, and C) three roads, where all of the cubes are 10x10x10 mm in size. The vertical line indicates where the predetermined release threshold was crossed for the release time measurement. ....	47
Figure 28: Box and whisker plot of the release time of specimens with a wall thickness of one, two, and three roads. The trend line is plotted using the averages of the respective measurements. ....	47
Figure 29: Varying shapes used to test the release profiles with A) an over extruded road wall to be 1.5 times the nozzle diameter on the cube (10 mm <sup>3</sup> ) and B) a capsule design using a 30 ° angle with varying wall thicknesses, where the volume is constant, but the surface area changes [15]. ....	49

Figure 30: A capsule containing two chambers (using the toolpath described in Figure 25). The top images are of the cube (10x10x10 mm) with liquid embedded inside each chamber where yellow has a one road thick wall and blue has a two-road thick wall. The graph shows an example of the tracking of the delay in release for the two chambers. The liquid/powder filled part is a larger double chamber (10x16x10 mm) that contains the blue liquid and a powder material (NaCl). .....50

Figure 31: The release time for the varying shapes in comparison to the trend line created from the cube specimens. The over-extruded part had n=1 and the angled parts had a minimum of n=3. The multi-release from the two chamber capsules are marked with a line between the first and second release. (\*Data from previous experiments, with slight variation in dissolution method [15]).....51

Figure 32: The advertised maximum temperature for and cost for FFF systems featuring bed and/or environment heating [121]–[130]. .....53

Figure 33: Three design concepts for handling the components compatibility to enable printing in high temperature environments. ....55

Figure 34: High environment temperature system design, where the printer is inverted to allow for an open bottom to the heated print area for the print head to be able to access without inhibiting movement. ....57

Figure 35: The simulation output for the a) the experimental set up, b) temperature profile, and c) the velocity profile for the inverted heat chamber. ....59

Figure 36: The temperature profile of different sized heat chamber using a 2D Fluent model. ...59

Figure 37: Functional prototype of a custom delta printer modified with the inverted heated build chamber. ....60

Figure 38: Experimental and modeled temperatures from the center of the bed outward where the chamber bed and walls were set to 50-350 °C, in the inverted heat chamber. The markers represent the measured temperatures, while the line represents the temperature values from the simulation. ....62

Figure 39: The measured temperatures at different displacements from the bed at temperature controller set temperatures are between 50-350°C, with a non-inverted heat chamber. The markers represent the experimental data, while the line represents the simulated data.....62

Figure 40: Printed tensile bars using the inverted printer printed at 25 °C and 200 °C. The tensile bars are 63.5 mm in length, 9.53 mm in width, and 3.17 mm in height. ....64

Figure 41: Tensile properties of tensile bars printed on inverted FFF system at environment temperatures of 25 °C (n=4) and 200 °C at 15 mm/s with a 200 μm layer height and 95% rectilinear +45/-45 infill (n=5). The horizontal line indicates reported Stratasys strength [135]..65

Figure 42: A standard part (3D Benchy) was printed to demonstrate the ability to print more complex parts in the inverted high temperature system. ....66

Figure 43: A schematic of the delta-style inverted printer with a heated build chamber used for printing (adapted from [150]). .....71

Figure 44: A scaled visualization of the parts packed into the cylindrical container. Set 3 also contained a temperature sensor placed below the complex part and toward the center of the cylinder. ....73

Figure 45: The temperature ramp and cooling cycle of the post-processing technique as measured by an embedded thermocouple. The post-processing time was set to 6, 12, 18, and 24 hrs. ....	73
Figure 46: Visualization of the printed tensile bars and how they were printed on the printer bed where a) represents the horizontal XY tensile specimens and b) represents the vertical YZ plane specimens. ....	74
Figure 47: The length dimensions measured before and after post-processing to evaluate dimensional accuracy. ....	75
Figure 48: A visualization of light absorbance for a) a printed road, b) a printed part, and c) a well-bonded printed part. D) Example of the collected data for a printed cylinder, using a color map to show absorbance. Data for the analysis was taken from the center of the well plate in a 12x12 array. ....	77
Figure 49: Thermal characterization of ULTEM® 1010 via A) TGA using a 10 °C/min ramp rate to 800 °C, B) DSC first heat and cooling cycle at 10 °C/min (Exo Down), and C) oscillatory rheology at 1% strain at various temperatures. ....	78
Figure 50: SEM images of freeze fractured printed squares that were printed with nozzle temperatures varying from 330-370 °C with the environment temperature set to 180 °C. ....	79
Figure 51: The mechanical properties of ULTEM® 1010 printed using nozzle temperatures between 330-370 °C, where the environment was set to 180 °C. The letters above each column indicate that there is no significant difference between columns with the same letter ( $p>0.05$ ), where XY specimens are only compared to XY specimens and Z specimens are only compared to Z specimens. ....	80
Figure 52: The mass of the printed square specimens used for SEM in relation to the nozzle temperature ( $n=3$ ). ....	80
Figure 53: SEM images of freeze fractured printed squares that were printed with environment temperatures varying from 50-225 °C with the nozzle temperature set to 360 °C. ....	81
Figure 54: The mechanical properties of ULTEM® 1010 printed using different environment temperatures. The letters above each column indicate that there is no significant difference between columns with the same letter ( $p>0.05$ ), where XY are only compared to XY and Z are only compared to Z. ....	82
Figure 55: Images of tensile bar curling when printed in a heated environment at various temperatures. (Nozzles temperature was 360 °C) ....	83
Figure 56: The sum of the curling on both ends of the XY tensile bars printed using a nozzle temperature of 360 °C in various environment temperatures. ....	83
Figure 57: Image of the printed parts after post-processing at 260 °C for A) 6 hrs., B) 12 hrs., C) 18 hrs., and D) 24 hrs. ....	84
Figure 58: SEM images of freeze fractured printed squares that were post-processed at 260 °C for times ranging from 0 to 24hrs. ....	86
Figure 59: SEM images of the exterior of a printed part that a) used no post-processing and b) was post-processed at 260 °C for 24 hrs. ....	87
Figure 60: The mechanical properties of ULTEM® 1010 post-processed at 260 °C for different periods of time. The letters above each column indicate that there is no significant difference between columns with the same letter ( $p>0.05$ ), where XY are only compared to XY and Z are only compared to Z. ....	88

Figure 61: The neck of XY and Z tensile bars post-processed for 24 hrs. The cross-section of each neck is ~3.175 mm. ....88

Figure 62: The percent change for the dimensional measurements (length and mass) taken before and after post-processing parts shown A) by post-processing time and by B) the layer in which the parts were packed in salt (where set 1 was on the bottom and set 5 was on top, Figure 44). .89

Figure 63: Absorbance measurements of light for the varying a) nozzle temperatures, b) environment temperatures, and c) post-processing time. The letters above each column indicate that there is no significant difference between columns with the same letter ( $p>0.05$ ). ....91

## List of Tables

Table 1: Materials developed and commercially available for FFF. ....	1
Table 2: The material properties taken from DSC and thermal conductivity testing. ....	12
Table 3. SEM images of ionic and non-ionic fillers before mixing.....	23
Table 4: The thermal properties extracted from the DSC curve, including the melting temperature, crystallization temperature, and the percent crystallinity (n=1). ....	27
Table 5: The experimental processing conditions were varied to test the effects of thermal processing on part properties. ....	70
Table 6: Controlled printing process parameters used to test the effects of thermal processing conditions. ....	71

# 1. Introduction

## 1.1 Material extrusion additive manufacturing

Material extrusion (ME) additive manufacturing (AM) is the process in which a material is selectively extruded through a nozzle [1]. ME machines predominantly use amorphous thermoplastic material wherein the material is heated to a malleable state, deposited, and cooled to a solid-state [2]. This can be accomplished by using a pressure-driven melt reservoir, a screw-driven pellet or powder feed, or gear driven filament feed.

The most prevalent machine type in industry and education uses filament feedstock, and the process is called fused filament fabrication (FFF) [3]. FFF is available on both desktop (~500 x 600 x 800 mm<sup>3</sup> in size) and industrial-scale (~1.3 x 0.9 x 2.0 m<sup>3</sup> in size) systems, where the machine and the material are generally less expensive when compared to the other AM processes. This has provided opportunities to democratize manufacturing, where parts and tools can be made locally rather than in a larger plant with distributed shipping. Examples where this is useful include developing countries' manufacturing tools [4], hospitals manufacturing custom replacements [5], and pharmacists manufacturing tailored drug delivery solutions for each patient [6].

There is a growing number of materials that are available for FFF. Table 1 lists some materials that are available as filament for FFF and an example manufacturer. These materials provide a variety of characteristics and material properties that can be applied to different applications, though some materials require specific types of FFF machines for processing (e.g. high-temperature, direct-drive extrusion, etc.).

Table 1: Materials developed and commercially available for FFF.

Material	Extrusion Temperature	Example Manufacturer
Acrylonitrile butadiene styrene (ABS)	230 ± 10 °C	MatterHackers
Poly(lactic acid) (PLA)	205 ± 15 °C	MatterHackers
Polyethylene terephthalate (PETG)	245 ± 10 °C	MatterHackers
Nylon	240 – 260 °C	MatterHackers
Polycaprolactone (PCL)	70 – 100 °C	VOGTEL
Thermoplastic polyurethane (TPU)	210 – 225 °C	Ninjatek
Polyether ether ketone (PEEK)	375 – 410 °C	3DX TECH
bioPolyphenylsulfone (PPSF or PPSU)	Not listed	Stratasys
ULTEM (1010 and 9085)	Not listed	Stratasys
Polycarbonates (PC)	Not listed	Stratasys

## 1.2 Research gap

Although the available materials for ME are growing they are generally limited to thermoplastic materials with limited molecular weight, melt rheology, and process between 190 °C - 250 °C. In order to take full advantage of AM's design freedom, a wider variety of materials available for the technology is required. This allows for the optimization of both the physical design and the material for a specific application.

To enable further development of new materials, a better understanding is needed of the FFF process-structure-property relationships. To address this, new materials that push the boundaries of FFF processing would provide insight that would result in a better understanding of the relationship. Therefore, the overall goal of this research is to expand materials through process and materials innovation. This was done for materials at two opposing extremes of processing temperatures: low-temperatures (<100 °C) for pharmaceutical applications and high-temperatures (>300 °C) for processing high-performance polymers. The full literature review related to each subject is located in the introduction of their relating chapter (Chapters 2-6). A brief summary of the research gap is described below.

### 1.2.1 Printing personalized medicine

AM's ability to offer complex part geometry and customizes manufacturing affords the opportunity to create personalized medicine. The dissolution rate, time of release, dosage, and drug combinations can be tailored for a patient's biological needs. The AM fabrication of oral-dose pharmaceuticals has been researched for the binder jetting, material jetting, and material extrusion AM technologies [7]–[10]. FFF offers distinct advantages in creating stronger parts that have low or no friability compared to the other AM processes [11]. However, FFF processing of the active ingredients is challenging because many actives are incompatible with the high processing temperatures (>100 °C) needed for most FFF thermoplastics [12]. The process and/or materials of FFF need to be adapted in-order to incorporate the low-temperature actives. By focusing on the incorporation of the low-temperature actives the lower thermal limits of the FFF process can be tested to better understand the FFF process-structure-property relationships.

### 1.2.2 Printing a high-performance polymer

ULTEM<sup>®</sup> is a high-performance polyetherimide (PEI) polymer class with high-strength and chemically resistant qualities that are dimensionally stable in high-temperature environments. The FFF processing of ULTEM<sup>®</sup> 9085 has been approved of use in aerospace applications [13]. ULTEM<sup>®</sup> 1010 has properties are advantageous for automotive (under the hood), outdoor construction, electrical devices, and energy storage applications [14]. When choosing to FFF print with these high-strength polymers, it is important that the final part exhibits the desired high-strength. Using higher processing temperatures causes increased molecular mobility which produces stronger bonds between discretely printed roads and layers. However, the processing temperatures are limited by thermal degradation of the material and the ability of the part to maintain its shape when above the glass transition temperature ( $T_g$ ). There exists a tradeoff in the FFF thermal processing between the mechanical strength and dimensional accuracy. A better understanding of this tradeoff for materials that are processed on the upper-limits of FFF will enable a better understanding of the overall FFF process-structure-property relationships.

## 1.3 Overall research goal

**The overall research goal of this work is to expand the library of materials that can be printed using material extrusion additive manufacturing.** The research gap is approached for two different general material needs: *a water-soluble material for incorporating actives* for programmable release applications and *a high-temperature (>300 °C) high-performance polymer* for structural applications.

The first material need for a *dissolvable material for incorporating actives* is approached by both i) *modifying the material* and ii) *modifying the process*. *Modifying the material* is done partly in collaboration with the Long Group in the Virginia Tech Department of Chemistry. This interdisciplinary research is focused on designing a new material for printing oral drug delivery

systems. The collaboration consists of the Long Group developing and synthesizing materials and the author analyzing the materials and their ability to be printed using FFF. The contributions of this portion of the research include the development of a low processing temperature, water-soluble material for tailored drug delivery, and insight to the broader understanding of the process-structure-property relationship to guide future design of ionic semi-crystalline materials (Chapter 2). This is then used to evaluate the incorporation of different filler materials to enable and improve processing via FFF while removing the need for a chemical processing step (Chapter 3). *Modifying the process* demonstrates how liquids and powders can be incorporated into a FFF part by embedding the substance inside of the printed part. This allows for the incorporation of active ingredients that could not otherwise be manufactured via FFF (Chapter 4). This solution focuses on the application for drug delivery; however, the process could be applied to other applications that require the incorporation of a material that cannot be FFF printed.

The second material need, *processing high-temperature (>300 °C) high-performance polymers*, is approached by first *modifying the machine* to enable the processing of polymers that require a high processing temperature (Chapter 5) and then using the machine to characterize and optimize the high-performance polymer Ultem 1010 (Chapter 6). The broad goal of this portion of the research is to create a tool that enables different processing conditions that allow for new materials to be printed via FFF and gain a better understanding of the effects of the build environment on the process-structure-property relationship. A specialized temperature-controlled chamber is designed, modeled, and fabricated to enable the printing of specialized materials in different temperature environments (Chapter 5). The design developed in this work enables the printing of high-processing temperature materials for FFF on a desktop-scale system, at an inexpensive cost. This broadens the market and increases the accessibility of this technology and material to new researchers to further optimize for and develop new materials and new users to have access to print these materials using improved operating conditions. The machine modification is used to improve printing by optimizing the thermal processing conditions for Ultem 1010. The part strength is additionally improved by the development of a post-processing technique in a heated oven above  $T_g$  by supporting printed parts with packed powder. This allows the bonding between the parts roads and layers to improve beyond what printing alone can achieve without sacrificing the shape of the part.

#### 1.4 Research Question 1 and Hypothesis

The first research question is focused on enabling the incorporation of active ingredients into printed parts. Sub-Question 1.1 is motivated by enabling a low processing temperature water-soluble material for FFF 3D printing that could later include active ingredients within the material. The unique feature of the developed SPEG series is the ionic interaction with the counterions. Changing the counterion changes the ionic strength, thus altering the material properties. Hypothesis 1.1.1 is that this can be used to tune the material properties for FFF processing. A separate approach to Sub-Question 1.1 (Hypothesis 1.1.2) is to modify the material by incorporating an additive. Additives can be processed with the sulfonated PEG and can interact with the ionic salt and alter the material properties. The ionic salt added to the PEG polymer backbone provides opportunities to alter the material properties for processability.

Sub-Question 1.2 is motivated by the idea of incorporating active ingredients into a printed part, without direct incorporation into filament. Previous work has shown active ingredients have been incorporated in-situ [15], [16] and in post-processing [17]. The proposed hypothesis here is to incorporate multiple actives during the print and use the geometry of the part to tailor the time the release of multiple actives during dissolution.

<b>Research Question 1</b>	
How can active ingredients, that cannot be processed at high temperatures (<100 °C), be incorporated into a water-soluble 3D part processed by FFF for tailored release?	
<b>Sub-Question 1.1</b>	
How can a low processing temperature dissolvable material be modified to be process-able via FFF?	
<b>Hypothesis 1.1.1</b>	<b>Hypothesis 1.1.2</b>
An ionic salt can be added to an existing polymer chain of a low processing temperature dissolvable material (PEG) to create discrete points of polar charges. Different counterions in the salt have different ionic interaction strength. Changing the ionic interaction strength changes the material properties to allow the ability to tune a material's properties to enable material extrusion FFF.	An ionic filler added to a low processing temperature dissolvable ionic polymer can influence the ionic interactions within the material. Using an ionic filler with a stronger ionic charge can influence the material properties in a similar way as changing counterions within a sulfonated ionic polymer. This allows for the ability to tune material properties using a filler material, in place of material synthesis.
<b>Sub-Question 1.2</b>	
How can active ingredients be incorporated into a printed part, without adding the actives directly into the material for tailored release?	
<b>Hypothesis 1.2</b>	
Active ingredients in a liquid or powder form can be embedded into a printed soluble material, where the wall thickness of the printed part will create a time delay for the release of multiple active ingredients.	

#### 1.4.1 Impact

The work generated from answering Sub-Question 1.1 aims to identify how counterions affect printability, quantitatively and qualitatively, and use these observations to determine how changes in the material properties affect FFF printing. The importance of this work is to show how modifying the material on the molecular level, or by incorporating a filler, can affect the macroscale properties and process-ability of a material for AM. Insight is also gained on how to print semi-crystalline polymers and how crystallization kinetics affect printability.

The work from Hypothesis 1.2 demonstrates the ability to modify the process to enable the incorporation of new materials and improve part quality. The incorporation of liquids and powders that cannot be printing via FFF in printed parts allows for controlled release, it also establishes design guidelines for creating thin-walled liquid-tight parts via FFF.

#### 1.5 Research Question 2 and Hypothesis

The second research question is focused on the FFF printing of the high-temperature, high-performance amorphous polymer ULTEM® 1010. Sub-Question 2.1 was created in order to develop a system to enable the printing of polymers that have high processing temperatures. This was used for Hypothesis 2.2 to study the effects of thermal processing and post-processing conditions on ULTEM® 1010 printed parts.

<b>Research Question 2</b>	
How does (post-) processing temperature affect the mechanical strength and dimensional accuracy for FFF printing a high-temperature, high-performance amorphous polymer (ULTEM <sup>®</sup> 1010)?	
	<b>Sub-Question 2.1</b>
	How can a desktop material extrusion machine be modified to enable high-performance materials?
	<b>Hypothesis 2.1</b>
	A heated environment is essential for printing high-performance polymers. An inverted heat chamber with an open bottom will trap heat within only the printing area, while an open bottom allows for free movement of the print head.
<b>Hypothesis 2.2</b>	
The strength and dimensional accuracy of a printed part can be improved by tuning the nozzle and environment temperatures. Incorporating post-processing above T <sub>g</sub> can improve the part strength further.	

#### 1.5.1 Impact

The impact of the low-cost, high-temperature machine in this work provides an open-architecture tool for materials development, optimization, and accessibility. Development of new materials that require specific environment temperatures can be created using this machine design. The simple, inexpensive design allows for the accessibility of this tool and the materials it can print to more users, democratizing manufacturing. The value of this machine is shown by answering the research posed in Sub-Question 2.2. Increasing of the quality of a high-performance polymer part by optimizing the processing and post-processing yields properties that are more similar to desired bulk material properties for applications that require the use of the high-performance polymer.

## 2. Tuning the material properties of a water-soluble ionic polymer using different counterions for material extrusion additive manufacturing

### 2.1 Introduction

Additive manufacturing (AM) of pharmaceuticals provides a distinct advantage compared to traditional oral medication manufacturing processes because it enables the fabrication of personalized dosages for each patient's individual needs. Customizing tablet geometry and chemistry enables the opportunity to tailor dissolution time, rate, quantity of drugs, and drug combinations for a patient's biological needs, which can vary based on gender, height, weight, diet, activity level, and other medications he/she is taking.

In 2015, the oral tablets SPRITAM (levetiracetam) became the first FDA approved drug that is manufactured using AM [18]. Research in the use of AM for fabricating customized oral dose medicine spans binder jetting, material jetting, and material extrusion technologies [7]–[10]. Each of these technologies have tradeoffs for printing pills. Binder jetting allows for very precise placement of multiple jetted drugs and the powder bed provides structural support for printing complex geometries [19]–[21]; however, the parts can be fragile and have high friability. Hot melt material jetting allows for precise placement of multiple materials without powder [22]; however, material jetting is limited to processing materials with sufficiently low viscosity for jetting. Material extrusion, can fabricate stronger parts that have low or no friability [11], and fused filament fabrication (FFF) (a subset of material extrusion) has been used to produce oral dose pills [23]. FFF machines are widely available as both inexpensive desktop-scale machines, for home or portable use, and larger industrial-scale machines [3]. However, fabricating tailored soluble pharmaceuticals can be challenging because the high processing temperatures (>100 °C) needed for melting most thermoplastics may degrade the active ingredient or cause loss of its potency [12].

To address this limitation, the authors previously developed a sulfonated poly(ethylene glycol) (SPEG) polymer series that melt processes at 70 °C and dissolves in less than 3.0 mg/min in water [24]. The melting temperature of this series is low enough that active ingredients can be added during thermal processing of pressed films, molds, and extrusion while retaining activity [25].

Using FFF to print semi-crystalline materials, such as SPEG, is challenging mainly due to crystallization resulting in discrete volume change and severe warping as the polymer cools from the melt state to the solid state. FFF traditionally uses amorphous materials that have a gradual change between a rubbery state and glassy state. Extruded material property changes as a function of temperature and occur gradually as the material cools, which deems the added stresses from volume change are also gradual. Conversely, semi-crystalline materials have a sharper transition between the malleable and solid state, where there is a discontinuity in the material properties as a function of temperature. Thus curling the part more severely as the material density increases during crystallization [26].

Another challenge specific to printing SPEGs is that their low melting temperature result in a small processing window between the extrusion and environment temperatures. This phenomenon causes the material to initially cool at a slower rate compared to traditional FFF materials that feature a processing temperature window of more than 100 °C. The slower rate consequently creates a longer time to solidify, resulting in the requirement for the material to be able to hold its extrudate shape for longer in the malleable state during the printing process. The extruded material must be able to bond with the previous roads without coalescing and losing form, remaining in the desired deposited shape.

The ability to vary a counterion that ionically modifies a polymer to alter the material properties [24], [27], [28], provides a unique advantage in developing a polymer for 3D printing and further customization and tailored design opportunities for adapting the material for specific printing applications. This paper aims to 3D print the SPEG series with varying counterions that result in variations in material properties. This allows for the ability to determine the ideal material properties for printing a low-temperature, semi-crystalline polymer and for identifying relationships between the print quality and the polymer properties. Specifically, the authors assess the structure-property-process relationships of four SPEG variants: poly(PEG<sub>8k</sub>-co-NaSIP), poly(PEG<sub>8k</sub>-co-CaSIP), poly(PEG<sub>8k</sub>-co-ZnSIP), and poly(PEG<sub>8k</sub>-co-MgSIP). A key contribution of this paper is to demonstrate how small changes in modifying a material on the molecular level can affect the macroscale properties and process-ability of a material for FFF. This is accomplished by measuring the SPEG series' material properties (e.g., thermal transitions, rheology, thermal diffusivity, and crystallization kinetics) and relate them to their 'printability' (e.g., layer bonding and quality of a variety of printed features).

## 2.2 Methods

Material characterization was conducted to provide insight as to how the different counterions affect the polymer behavior during processing. The thermal transitions inform (i) the state of the material at different temperatures and (ii) appropriate temperatures for processing the material. Rheological properties inform constraints on processing, including extrusion rate. Zero shear viscosity provides insight on a material's ability to hold its shape in the melt state after the deposition of each layer. Thermal diffusivity is directly related to thermal conductivity, which is an important material property for understanding how quickly a material melts and cools when it is at different temperatures. Finally, crystallization kinetics for a polymer reveal how the crystals nucleate and spherulites grow, which affects solidification behavior (e.g., rate, shrinkage, and residual stress) following extrusion.

The material properties of the polymers are then related to their printability by measuring the layer bonding of the resultant printed parts as well as evaluating the quality of different printed features (Section 2.3).

### 2.2.1 Materials Material Preparation and Synthesis

Poly(ethylene glycol) (PEG<sub>8k</sub>) (Sigma-Aldrich,  $M_n = 8,000$  g/mol), dimethyl 5-sulfoisophthalate sodium salt (SIP, Sigma-Aldrich, 98 %), and sodium acetate (NaOAc) (Sigma-Aldrich,  $\geq 99.0$  %) were dried in a vacuum oven at 50 °C overnight before use. Titanium tetra(isopropoxide) (Sigma-Aldrich) was dissolved in anhydrous 1-butanol and used as a stock solution at 0.01 g/mL or 0.013 g/mL. All solvents were received from Spectrum and used without further purification.

The synthesis of sulfonated PEG (SPEG) was adopted from a previously reported procedure [24]. Briefly, 8k poly(ethylene glycol) (PEG<sub>8k</sub>) (1 eq.) and dimethyl 5-sulfoisophthalate sodium salt (1 eq.) (SIP) were placed into a round-bottomed flask equipped with a mechanical stirrer. The reaction mixture was heated to 180 °C and stirred for 3 hours under N<sub>2</sub> and 30 min at 0.1 mbar to yield poly(PEG<sub>8k</sub>-co-NaSIP). The sodium counterion was then exchanged with calcium, zinc, and magnesium salts in separate batches through dialysis to form three distinct polymers. The dissolved polymer was then frozen and lyophilized into a white, fluffy polymer, which was melted via extrusion processing into filament (Section 2.2.3.1). Figure 1 shows a scheme of the chemical synthesis, including an ion exchange, used to make the family of SPEGs utilized in this work. They contain the counterions: Na<sup>1+</sup>, Ca<sup>2+</sup>, Zn<sup>2+</sup>, and Mg<sup>2+</sup>.

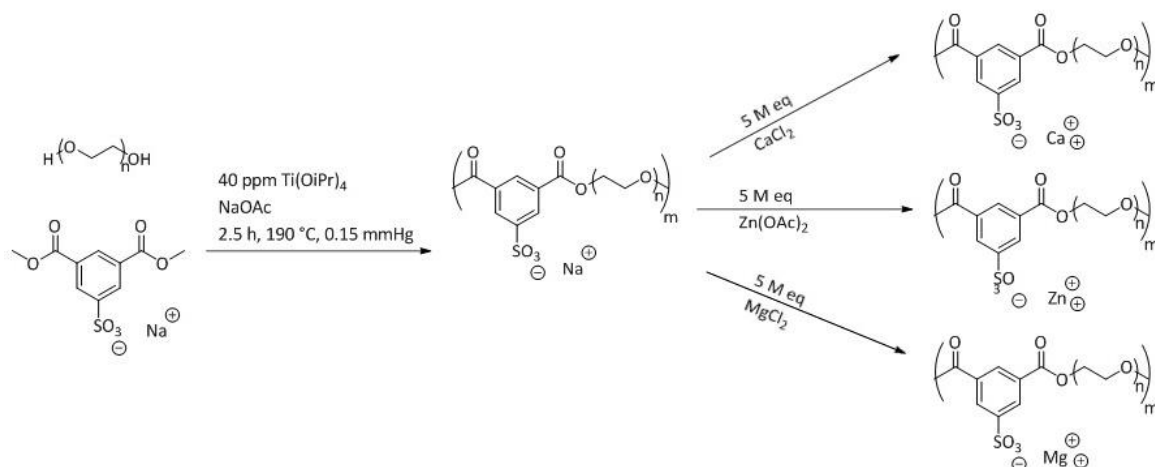


Figure 1. Melt transesterification of poly(ethylene glycol) and sulfonated isophthalate (SIP) to yield ion-containing poly(ether ester)s and the ion exchange of poly(PEG<sub>8k</sub>-co-NaSIP) to a range of counterions through dialysis [24].

## 2.2.2 Material Characterization

For the material analysis in the following methods, 70 °C was used as a reference temperature for all experiments as 70 °C was sufficient for complete melting during extrusion printing.

### 2.2.2.1 Thermal Analysis

Differential scanning calorimetry (DSC) was performed with a nitrogen flow of 50 mL/min at a heating rate of 10 °C/min and quench cooling on a TA instruments Q1000 DSC from -80 °C to 100 °C. Melting temperatures were measured as the maximum of the melting endotherm and the crystallization temperatures at the max of the exothermal peak.

### 2.2.2.2 Oscillatory Rheology

Rheological analysis was performed on a TA Instruments Discovery HR-1 with 25 mm parallel plates under air. The experiments were in a controlled temperature environment with liquid nitrogen cooling for the temperature ramp. Frequency sweep experiments were performed at 70 °C with angular frequencies ranging from 0.1 – 100 rad/s with a constant strain of 1 %. Rheological cooling was run at an angular frequency of 1 rad/s oscillation with constant strain of 1 % using a temperature ramp from 70 °C down to 45 °C taking data every 5 °C.

### 2.2.2.3 Thermal Diffusivity

The laser-induced transient thermal grating (TTG) technique [29]–[35] was used to measure the thermal diffusivity. In this method, two pump pulse beams (pulse duration 4-8 ps, frequency 1 kHz, wavelength 532 nm, pulse energy 75 μJ) with the same phase and frequency interfere in the sample and create a spatially periodic temperature distribution profile called thermal grating. The decay of the thermal grating is monitored via the diffraction of a chopped continuous-wave (CW) probe beam (chopped pulse duration 200 μs, chopping frequency 1 kHz, wavelength 514 nm, CW power 500 mW), which can give the thermal diffusivity with high accuracy. In the measurements, the transmission geometry in the TTG setup was used, and the signals were enhanced by heterodyne detection. Since the solutions are transparent and colorless, <1 wt% blue dye was added into the solutions to absorb part of the pump pulse beams in order to generate thermal grating in the sample. The effect of the dye on thermal diffusivity was confirmed to be minimal and the

concentration of dye was kept the same for different solutions. The sample solution was placed in a 1 mm-thick cuvette. A water bath was used to control the sample temperature. The concentrations of all the four SPEG samples are 0.37 g/ml. The sample temperatures were estimated based on the temperature gradient in the cuvette and the laser heating effect.

#### 2.2.2.4 Polarized Light Microscopy

Spherulitic growth of all SPEG counterion samples were observed via an Olympus BX51 microscope with crossed-polarizers and Linkam hot stage. Each SPEG was melted at 70 °C and naturally cooled to room temperature on the Linkam hot stage to provide the same thermal history for each sample that is similar to printing conditions. A video was collected during dynamic cooling of each sample at 80 °C/min to room temperature following a 1 min isotherm at 70 °C. Representative images from the video capture were selected to show spherulitic growth at different stages. Radius measurements were made for each sample at each time step to create a spherulitic growth rate plot. These experimental conditions were selected to mimic printing conditions.

### 2.2.3 Print Quality

#### 2.2.3.1 Processing Filament

The lyophilized SPEGs were processed using a desktop single-screw extruder (Filabot Wee) into filament strands with a 1.75 mm target diameter. The materials were ground to roughly pellet size pieces. The temperature was set to approximately 70 °C for each SPEG and the feed screw is a single speed of 35 rpm. The filament was extruded out of a 2 mm diameter nozzle and cooled on a Teflon conveyor belt pulling the material to reduce the diameter. Along the belt, forced convection was used as needed to cool the extruded filament. Filament was processed to 1.75±0.15 mm, where shorter sections of filament could be used for printing with an accuracy of ±0.05 mm.

#### 2.2.3.2 Print Parameters

The specimen .stl files were converted to a gcode file using Slic3r (Slic3r v1.1.7), an open-source slicing engine for FFF systems. The extruder temperature was set to 70 °C based on DSC and rheology. A constant print speed was chosen to extrude the material at 5 mm/s. Blue painters tape was placed onto the print bed to provide additional adhesion for the extruded polymers. Before each print, the filament diameter being fed into the machine was measured and input into Slic3r to calculate the correct federate for each filament strand.

#### 2.2.3.3 Measuring Layer Bonding

Interlayer adhesion has been measured by a variety of techniques [36]–[38]. The method used for this work resembles Yan's method [36]. A prism was printed with a single-road wall thickness and no infill; dogbone tensile bars were punched from each of the printed prism's thin walls. Each wall of the structure produced a single tensile bar, creating five or six tensile specimens per print. Figure 2 shows the design of the part, and an example of where a tensile bar is punched from one wall for both for XY and Z tensile bar specimens. This method was chosen for the following reasons:

- *Minimal material consumption:* This technique requires less than 1 cm<sup>3</sup> of material to complete the entire build while also fabricating multiple specimens with different layering direction for evaluation. Minimizing material consumption is critical when designing novel materials as synthesized batches are only available in small quantities.
- *Minimize road variation:* Creating a thin wall eliminates the variation in road path and therefore the time between each layer, creating more uniform layer bonding. In addition, each layer consists of only a single, continuous-printed road, which standardizes the amount

of time the polymer resides in the hot extruder, thus and improves uniformity of the bonding between layers.

- *Minimize curling effect:* Curling is minimized by depositing a single printed road, which minimizes the likelihood of curling often found when printing a number of long continuous roads. This approach enables the evaluation of bond strength for materials that have limited process-ability.

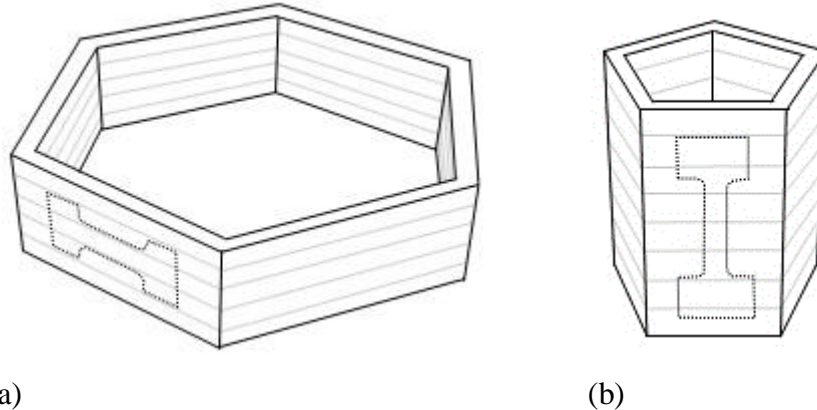


Figure 2: Schematic of printed single-road prisms for evaluating layer bond strength. Lighter lines illustrate layered structure. Dashed lines show outline of tensile bar specimen punch for (a) XY tensile specimens and (b) Z tensile specimens.

The tensile bars measured approximately 22.75 mm by 7.75 mm. The neck region was 7.0 mm in length and 2.5 mm in width. The cross section was measured for each tensile bar to calculate the engineering stress. The thickness was measured using a micrometer. Specimens were broken using an Instron 5500R machine at 5 mm/s. Due to the small size of the specimens, the strain was calculated by using the change in the distance between the grips added to the length of the neck region (7 mm). Ultimate tensile strength, elongation, and modulus of elasticity were evaluated using Bluehill and MATLAB.

#### 2.2.3.4 Evaluation Quality of Printed Features

The print quality was qualitatively measured by attempting to print different features with the four materials. These features were designed to evaluate a polymer's ability to print independent of process parameters or printer configuration. The same print settings were used for the different parts and all parts were printed on the same printer. The print speed was set to 5 mm/s, and the extruder temperature was set to 70 °C. As SPEG has a low melting temperature relative to the environmental temperature, no additional heating (e.g., through a heated bed or a heated print environment) was used. Forced convection was used (via small fans mounted on the side of the printer) during most prints, which accelerated extrudate solidification and thus improved retention of shape. Further discussion on the importance of cooling is in Section 2.3.1.1.

Five different features were printed using each material: (1) large thin walled and (2) solid structures, (3) small thin walled and (4) solid structures, and a (5) bridge across a gap (Figure 3). For these tests, "large" is defined as features between 20-61.5 mm; this is large enough for a material to demonstrate curling, while using a minimal amount of material. Small features are defined as < 10 mm. The thin-walled structures were designed as solid parts and printed with 0% infill with one perimeter wall in the Slic3r settings. The solid parts were printed at 90% density infill; this was chosen because i) some of the materials thermally expanded while printing and ii)

the filaments had slight variation in diameter, which can cause issues when printing 100% dense parts.

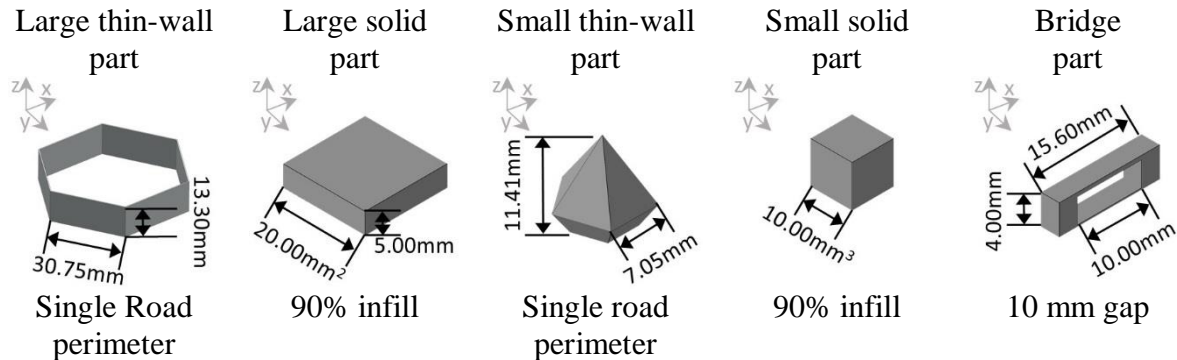


Figure 3: The features used to test the various elements of printability of the different counterion SPEGs.

- (1) The large, thin-walled part is used for creating tensile specimens as described in Section 2.2.3.3.
- (2) The large, solid part is 20 x 20 x 5 mm. This geometry allows for analysis of part curling for dense parts (e.g., at the corners where part curling is most likely to occur).
- (3) The small, thin-walled (i.e., one road thickness) part tapers at a 30° angle to evaluate printing of small feature sizes (e.g., as the features become smaller there is less time between layers to cool).
- (4) A cube was used for the small, solid part, where the edges and corners serve as defined small features to see if the material can hold those features when there is less time between layers and the solid infill will not cool as fast as a thin wall. The flat top will show the road definition and surface finish of the material printing a small feature.

A bridge geometry, which requires the extruded material to span a 10 mm gap without support material, is printed to observe the materials' potential for fabricating complex shapes without support material.

## 2.3 Results and Discussion

### 2.3.1 Material Properties

Material properties were measured to quantify the variations in the SPEGs caused by the different counterion ionic interactions.

#### 2.3.1.1 Thermal Analysis

DSC measured the peak melting temperature, peak crystallization temperature, crystallinity, and specific heat capacity ( $C_p$ ) of poly(PEG<sub>8k</sub>-co-NaSIP), poly(PEG<sub>8k</sub>-co-CaSIP), poly(PEG<sub>8k</sub>-co-ZnSIP), and poly(PEG<sub>8k</sub>-co-MgSIP) (Table 2). Figure 4 depicts the DSC traces for each polymer system. Both the first cooling and second heat are shown. Among the different counterions, the variance in the melting temperature ( $T_m$ ) was 6 °C and the variance in the crystallization temperature ( $T_c$ ) was 12 °C. These transition temperatures can be approximated to be the same because the polymer backbones are the same. However, for each sample there is a gap of  $31.5 \pm 5.8$  °C between the  $T_m$  and the  $T_c$ , which impacts how much the material must cool before solidifying.

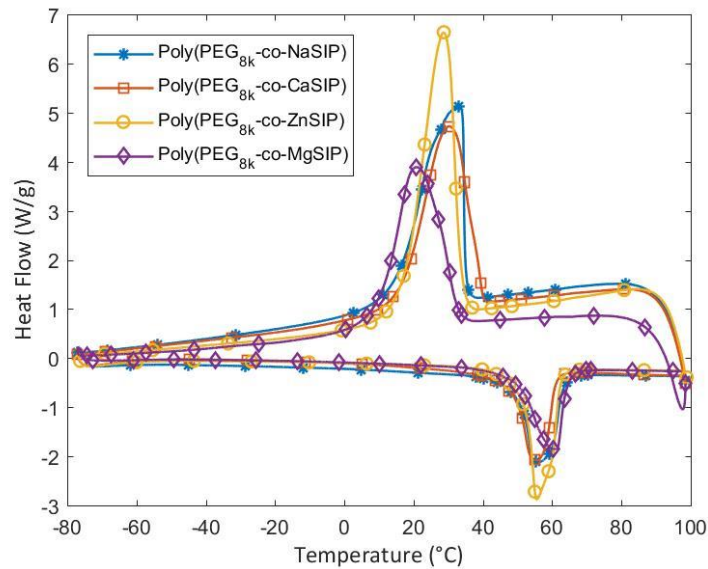


Figure 4: DSC traces depicting the cooling after the first heat and the second heat heating at 10 °C/min with 100 °C/min cooling of the SPEG materials containing four different counterions. Exothermal up.

Table 2: The material properties taken from DSC and thermal conductivity testing.

Sample	T <sub>c</sub> (°C)	T <sub>m</sub> (°C)	Crystallinity (%)	C <sub>p</sub> @ 25 °C (J/g °C)	C <sub>p</sub> @ 70 °C (J/g °C)
Poly(PEG <sub>8k</sub> -co-NaSIP)	33	62	58.9	1.88	2.51
Poly(PEG <sub>8k</sub> -co-CaSIP)	30	60	53.4	1.36	2.32
Poly(PEG <sub>8k</sub> -co-ZnSIP)	29	56	69.5	0.910	1.40
Poly(PEG <sub>8k</sub> -co-MgSIP)	21	61	53.7	0.959	1.28

The T<sub>m</sub> and T<sub>c</sub> are important in the printing process because the polymer must be melted in order to flow when extruding out of the print nozzle and crystallize, post-deposition, in order to hold shape. Setting the processing temperature at ~10 °C degrees above the polymer T<sub>m</sub> ensures the heat conducts completely through the thickness of the filament faster than the material is extruded. Although the crystallization temperature measured is dependent on the cooling rate of the DSC, it can be approximated from the data in Table 1 that the SPEG series must cool ~40 °C below the extrusion temperature to crystallize and solidify. Because the crystallization temperatures are near room temperature, the time it takes for the material to solidify is significantly longer than traditional FFF materials that are printed at higher temperatures (e.g., ABS is typically extruded above 230 °C). This behavior can be seen when observing the general heat transfer equation for transient thermal cooling.

$$T = T_{\infty} + (T_i - T_{\infty})e^{-\frac{hA_s t}{\rho V c}} \quad [1]$$

where  $T$  is the temperature of the material,  $T_{\infty}$  is the environment (room) temperature,  $T_i$  is the initial (extrusion) temperature,  $h$  is the convection coefficient,  $A_s$  is the surface area,  $t$  is time,  $\rho$  is the density,  $V$  is the volume, and  $c$  is the thermal heat capacitance. Note that this is a simplified model to examine the impact of the temperature difference in  $T_m$  and the  $T_c$ .

When comparing the different materials, it can be assumed that the convection coefficient, surface area, and volume are equivalent as they are not intrinsic material properties. The rate of cooling is only dependent on the density and the specific heat capacity. The ability for the material to hold shape is dependent on the temperature of the material as it controls the molecular mobility of the polymer.

When considering a traditional 3D printing material, Acrylonitrile butadiene styrene (ABS), the print temperature is somewhere around 220-270 °C and the ambient temperature is as high as 100 °C. The print temperature is set well above the glass transition point (~105 °C), to enable a low enough viscosity for the material to flow out of the nozzle. This means that the material is viscous enough to not flow out of the nozzle, and presumably viscous enough to hold its shape around 200 °C. This temperature is reached fairly quickly (<5 s) as the material extrudes from the nozzle and the temperature exponentially decays from 220 °C to 100 °C.

The cooling rate is slower for the SPEG series. The difference between the melting temperature and the environment temperature is much smaller than ABS, therefore the cooling rate is expected to be slower when the material first leaves the nozzle. The crystallization temperature is ~4 °C from room temperature, in the asymptotic region of the exponential decay rather than the early region, where the rate of temperature change is much faster. This indicates that the material must maintain its shape in the malleable state for longer than traditionally FFF materials, because it will take longer for the material to cool to a solid state.

### 2.3.1.2 Rheology

The viscosity profile measured for poly(PEG<sub>8k</sub>-co-NaSIP) is a magnitude lower than any of the others in the series. The zero shear viscosity, shown in Figure 5, is similar to ABS, a known standard printable material, at a print temperature of 250 °C and approximate printing shear rates (10-100 1/s) [39]. The divalent counterions caused an increase in the viscosity, which is consistent with observations seen in previous work [24]. The hypothesis is that the higher charge in the divalent cations create stronger ionic complexes resulting from the coordination of PEG oxygens and the divalent cations [40].

Shear thinning behavior can be seen in the Ca<sup>2+</sup>, Zn<sup>2+</sup>, and Mg<sup>2+</sup> counterions after a Newtonian plateau (Figure 5). Shear thinning is desirable for material extrusion because the material has a lower viscosity as it exists the nozzle and a higher zero shear viscosity to hold the extrudate's shape while it cools and solidifies [41]. With traditional higher temperature (>200 °C) amorphous materials, it is desirable to have a low viscosity (~2000 Pa·s) at the processing temperature and shear rate; however, too low of a viscosity can cause extrusion backflow and nozzle clogging [42]. In order for SPEGs to sufficiently hold their shape after deposition and before crystalizing, higher zero-shear viscosities may be necessary.

Figure 6 depicts a rheological study, which monitors the viscosity of the material from 70 °C to 40 °C. The temperature range was chosen to study the viscosity profile as the material approaches its crystallization temperature, which gives insight into the material behavior immediately after deposition. From 70 °C to 50 °C, the zero shear viscosity increases exponentially 158 ± 39 % for the SPEG series before crystallization occurs. Although the material is increasing

in viscosity, the zero shear viscosity of poly(PEG<sub>8k</sub>-co-NaSIP) at the processing temperature is a magnitude lower than the traditional FFF material ABS, which has a zero shear viscosity of around 10<sup>4</sup> Pa·s [39]. This may indicate that the viscosity of the Na<sup>+</sup> counterion may be too low to be able to hold its shape after deposition.

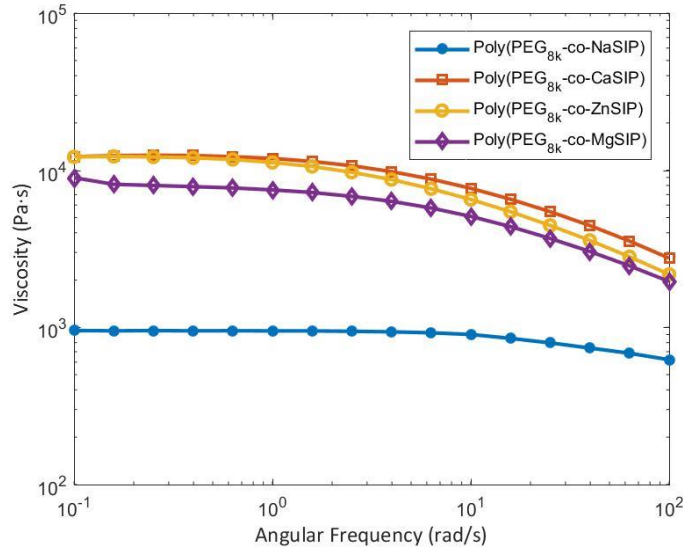


Figure 5: Oscillatory rheology of the SPEG materials containing four different counterions using parallel plates at constant temperature 70 °C and 1% strain.

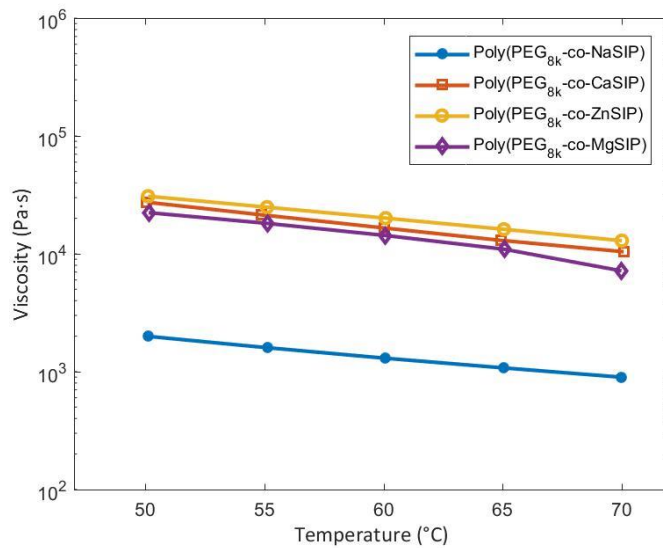


Figure 6: Oscillatory rheology of the SPEG materials containing four different counterions using parallel plates at 1% strain and 1 rad/s (near zero shear) temperature step down from 70 °C to 50 °C.

### 2.3.1.3 Thermal Diffusivity

The thermal diffusivity increased slightly with increasing temperature for all of the different counterions, as seen in Figure 7. The Na<sup>1+</sup>, Ca<sup>2+</sup>, and Mg<sup>2+</sup> counterions all showed a similar thermal diffusivity. However, the Zn<sup>2+</sup> counterion has a ~0.01 mm<sup>2</sup>/s lower thermal diffusivity. Thermal diffusivity has a direct relationship to thermal conductivity, which has a direct influence on the

temperature of the material during processing [43]. A higher thermal diffusivity will conduct heat faster, enabling the material to melt quickly and cool quickly. However, when considering layer bonding, having a lower thermal diffusivity could also be desirable, keeping the previous layers at a higher temperature helps interlayer adhesion [36]. Higher temperatures result in a higher weld strength, which require more energy to tear the layers [44]. With these materials, a higher thermal diffusivity is desirable because the printing temperature is already very close to the environment temperature, as previously described in Section 2.3.1.1.

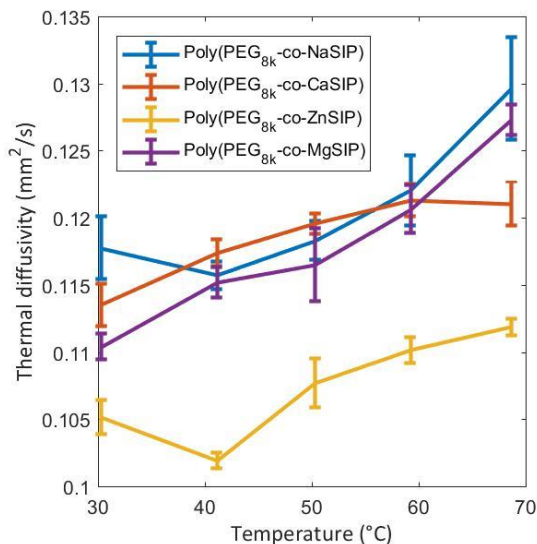


Figure 7: Thermal diffusivity of the SPEG materials containing four different counterions using laser-induced transient thermal grating (TTG) technique.

#### 2.3.1.4 Cross Polarized Microscopy

Changing counterions on the SPEG polymer alters the observed nucleation and spherulitic growth behavior, as seen in other polymer systems [28]. Figure 8 contains images depicting spherulites for the four counterion samples with a timestamp to indicate the elapsed time for observed spherulite formation. All counterions demonstrate heterogeneous nucleation behavior; however, the choice of counterion influences the final spherulite size. This ranges from the Ca<sup>2+</sup> sample resulting in spherulites too small to measure (radii < 10 μm) to the Zn<sup>2+</sup> sample resulting in spherulites with radii above 200 μm. The Na<sup>1+</sup> and Mg<sup>2+</sup> counterions result in average final radii of 66 ± 20 μm and 93 ± 31 μm respectively. The Mg<sup>2+</sup> counterion also results in spherulites with coarser texture than those of the other three counterions.

Because the percent crystallinity is similar among the SPEG series, but the spherulite growth rate and final size differ, the crystallization kinetics and spherulite size, and not the total percent crystallinity, appear to have the greatest effect on the printability of semi-crystalline polymers. Unsurprisingly, due to the large size of its spherulites, brittle behavior was observed in the Zn<sup>2+</sup> counterion SPEG. This corresponds with the low nucleation density observed and large spherulite interfaces. Conversely, the Ca<sup>2+</sup> counterion resulted in a high nucleation density and small final spherulite size. The small spherulitic morphology is expected to be stronger where the spherulites and interfaces are tightly interlocked [45]. The small spherulites also may reduce macroscopic part curling. The similarity between the crystalline morphology produced by Na<sup>1+</sup> and Mg<sup>2+</sup> counterions also show similarities on the macro scale (Section 2.3.3, Figure 12).

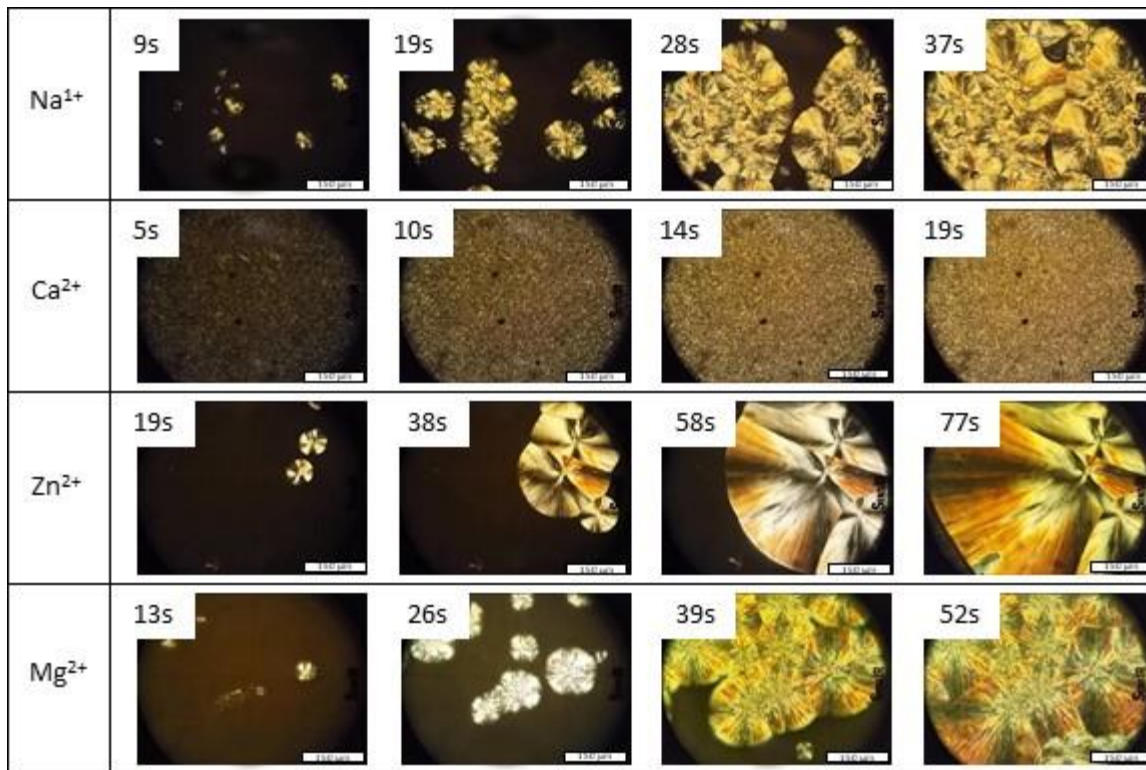


Figure 8: Images of SPEGs containing the four different counterions taken using polarized light microscopy. The timestamps shown are referenced to the first observed spherulite. The total time from observed spherulitic formation until impingement was evenly divided into four parts; images are shown at each time increment. The scale bar shows 150  $\mu\text{m}$ .

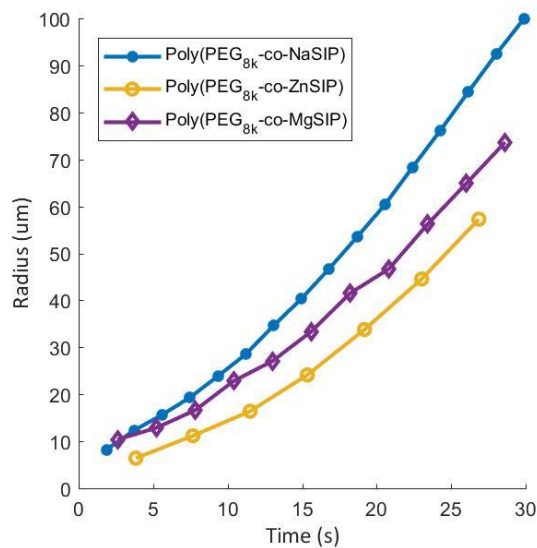


Figure 9: The spherulitic growth rate of three of the SPEG polymers containing different counterions. Poly(PEG<sub>8k</sub>-co-CaSIP) is not shown because the spherulites are too small for quantitative image analysis.

A typical isothermal plot of spherulitic growth rate results in a linear relationship between radius and time. The non-linearity observed in Figure 9 is due to the non-isothermal nature of the experiment, which mimics the non-isothermal cooling conditions during printing. A slower growth rate was observed at earlier times, increasing as the experiment continues. Given that these data represent dynamic cooling, this is equivalent to a faster growth rate at lower temperatures, thereby indicating the temperature range relevant to printing (70 °C – 25 °C) is in the nucleation-controlled regime. This is corroborated by the isothermal crystallization half-time plot, shown in Figure 10.

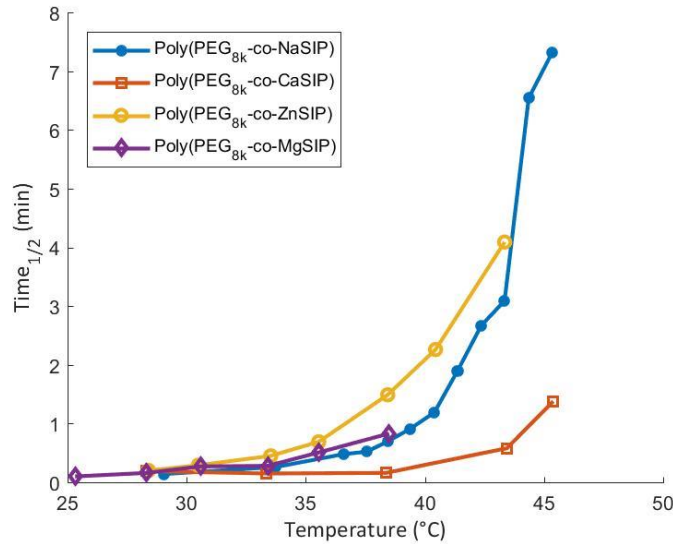


Figure 10. Crystallization half-time as a function of isothermal temperature for SPEG containing four different counterions.

### 2.3.2 Effects of counter ions on printed tensile properties

As expected, the printed specimens oriented in the vertical direction were weaker than the specimens printed in the horizontal direction and the melt pressed material [46], as shown in Figure 11. The poly(PEG<sub>8k</sub>-co-ZnSIP) tensile bars oriented along the Z plane were too brittle to punch and handle and were therefore omitted from the data. The large spherulites that formed during solidification (Figure 8) cause the brittleness. This is also reflected in the weak pressed films and the large scatter in the XY print specimens. The XY printed parts had both a higher elastic modulus and ultimate tensile strength, because the layers prevented any initial cracking or tearing from propagating across the tensile bar.

Poly(PEG<sub>8k</sub>-co-CaSIP) material was the strongest material in the film state. Although Ca<sup>2+</sup>, Zn<sup>2+</sup>, and Mg<sup>2+</sup> are all divalent counterions, the ultimate tensile strength from the film is 20.5 % and >2000 % higher than Mg<sup>2+</sup> and Zn<sup>2+</sup> respectively. Consistently, Zn<sup>2+</sup> was the weakest, followed by Mg<sup>2+</sup> and Na<sup>1+</sup>, then Ca<sup>2+</sup>. This trend is the same as the spherulite sizes shown in Figure 8. Typically, the raw material is stronger than printed parts because of the gaps the roads introduce into the part, which is observed in the ultimate tensile strength [47]. However, the Ca<sup>2+</sup> part had larger elongation at break for the XY printed material rather than the pressed film. This was caused by the weak layer weld bonding in the Z direction from laying a hot layer on a cold layer [44], and the part was only composed of a single road. As the material was pulled it plastically deformed after yielding and dramatically reduced the cross-section. When the cross-section deformed, the bonds between the layers broke first, and the material continued to stretch along each road, until each road broke. This was repeatable across all of the printed samples at these

print parameters. This was consistent with the ultimate tensile data, where the Z specimen is 45 % weaker than the XY specimen, and therefore was likely to fail under the horizontal strain caused by the plastic deformation. This result may not hold true if multiple roads are printed side by side in multi-walled structures.

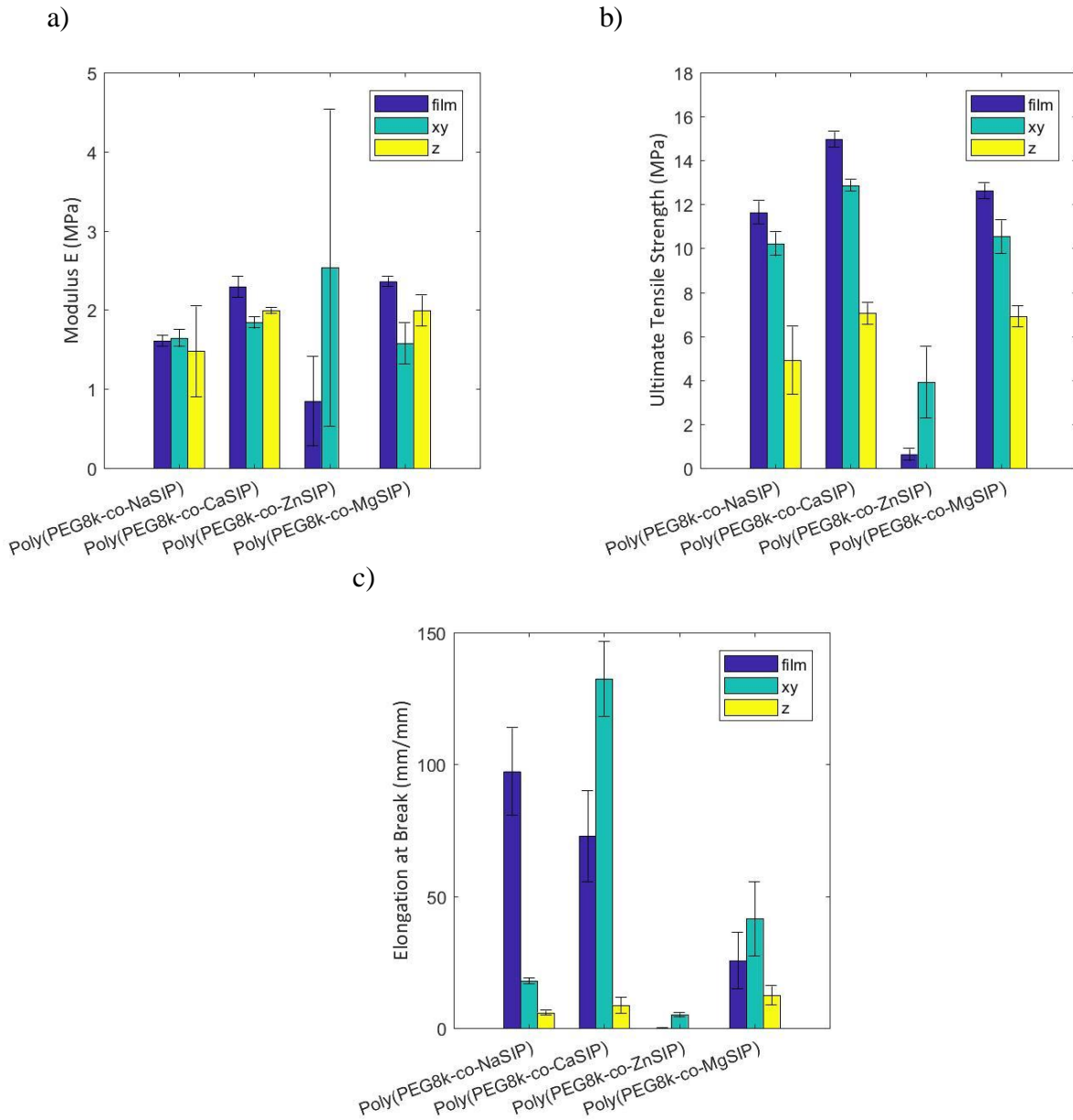


Figure 11: Evaluation of the tensile strength for poly(PEG<sub>8k</sub>-co-NaSIP), poly(PEG<sub>8k</sub>-co-CaSIP), poly(PEG<sub>8k</sub>-co-ZnSIP), poly(PEG<sub>8k</sub>-co-MgSIP) for melt pressed, and printed in a horizontal (xy) and vertical (z) orientation by a) the elastic modulus, b) the ultimate tensile strength, and c) the elongation at break.

### 2.3.3 Effects of counter ions on printability

The printability of each counterion material was tested by printing different small feature parts. The brittle  $\text{Zn}^{2+}$  counterion material caused the filament strands to break into short pieces unable of printing complete specimen. Figure 12 shows images of the different feature tests.

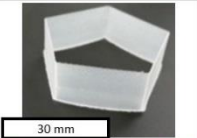
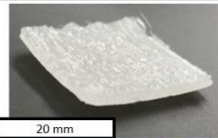
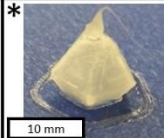
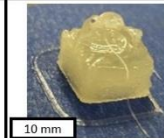
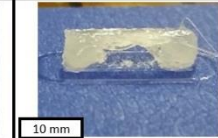
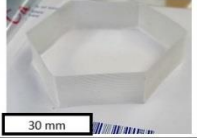
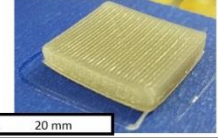
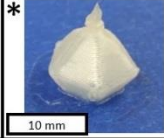
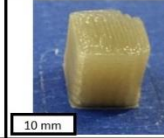
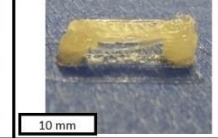
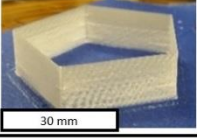
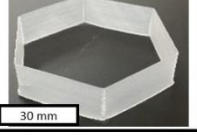
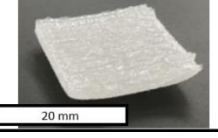
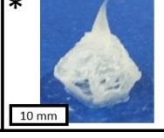
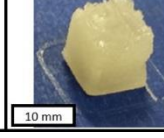
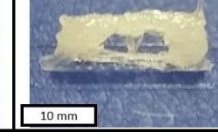
	Large thin wall part	Large 90% solid wall part	Small thin wall part	Small 90% solid part	10mm bridge
$\text{Na}^{1+}$			* 		
$\text{Ca}^{2+}$			* 		
$\text{Zn}^{2+}$		Filament too brittle to complete all prints			
$\text{Mg}^{2+}$			* 		

Figure 12: Part printed out of SPEG containing four different counterions using filament material extrusion. All parts were printed at 70 °C at 5 mm/s. (Note: \*were printed at 2 mm/s rather than 5 mm/s)

#### 2.3.3.1 Large parts analysis

The large thin wall and solid parts produced a larger curling effect than the smaller parts. This correlates with the crystallization of the material, as previously discussed in section 2.3.1.4, where the larger spherulites produced more curling. The small spherulites in the  $\text{Ca}^{2+}$  counterion reduced the internal stresses in the part during the shrinking process. The high nucleation density allowed the crystals to form in place. The  $\text{Na}^{1+}$  and  $\text{Mg}^{2+}$  counterion materials, with larger spherulites than the  $\text{Ca}^{2+}$  counterion material, both curled on the corners of the large printed parts. The effect was most noticeable on the solid part because the larger part size amplifies the internal stresses while cooling, causing the part to curl in order to relax the stress. The  $\text{Zn}^{2+}$  counterion material had the largest spherulites (Figure 8); however, the large thin walled structure did not curl during printing. This may be caused by strong bed adhesion, degradation, the elastic modulus may be too low for the part to curl, or the potential creation of micro fractures in the part that relieve the stress, also contributing to the parts brittleness.

#### 2.3.3.2 Small parts analysis

The low viscosity and thermal diffusivity of the material caused the small thin walled and solid parts to lose definition. The small thin-walled part had a decreasing cross-section and time between layers. As the part was printed, all of the materials lost part accuracy and definition as the perimeter of the pentagon decreased. The material was unable to cool and solidify before the next layers

were deposited and the viscosity was insufficient to hold the extruded road position and shape while the print head continuously deposited new layers.

The small solid part exhibited a similar issue with the  $\text{Na}^{1+}$  and  $\text{Mg}^{2+}$  counterion parts. The outside surface roads maintained the most definition due to convection on the larger surface area on the outside. The center of the part lost nearly all definition for the  $\text{Na}^{1+}$  and  $\text{Mg}^{2+}$  counterions due to the material expanding and the solid part design retaining heat causing the low viscosity roads to coalesce in the part center. As the melted material was deposited, the perimeter of the layer cooled first while the infill remained molten. The internal molten material expanded in the vertical direction due to the solidified perimeter. This propagated layer-by-layer, without sufficient time to cool and shrink between layers, causing a cascading effect where the  $\text{Na}^{1+}$  counterion material expanded past the nozzle tip and the print failed, due to the nozzle tip dragging through previous layers. The  $\text{Mg}^{2+}$  counterion also experienced this issue; however, to a lesser degree, as the small solid part was able to be completed.

The improvement in the small solid cube from the  $\text{Na}^{1+}$  to the  $\text{Mg}^{2+}$  counterion could be the stronger ionic attraction to the divalent counterion to prevent the  $\text{Mg}^{2+}$  material from thermally expanding as much as the  $\text{Na}^{1+}$  material, which is represented by the increased viscosity of the  $\text{Mg}^{2+}$  material. The  $\text{Ca}^{2+}$  counterion shows the most improvement in printing the small solid part. The divalent  $\text{Ca}^{2+}$  counterion material showed minimal volumetric expansion and the increased viscosity helped the material hold shape printing the solid parts. This may suggest a stronger ionic interaction with the  $\text{Ca}^{2+}$  divalent counterion compared to  $\text{Mg}^{2+}$ . There were clear road definitions every layer of the solid  $\text{Ca}^{2+}$  parts, where the  $\text{Na}^{1+}$  and  $\text{Mg}^{2+}$  parts lost definition internally, where roads coalesced together. This could also indicate a difference in surface tension between the  $\text{Mg}^{2+}$  and  $\text{Ca}^{2+}$  counterions, where the  $\text{Mg}^{2+}$  coalesced more than the  $\text{Ca}^{2+}$  counterion, despite similar melt viscosities. This experiment is an example of how both the melt properties and the cooling and crystallization properties contribute to the part quality.

#### *2.3.3.3 Bridge part analysis*

The  $\text{Na}^{1+}$ ,  $\text{Ca}^{2+}$ , and  $\text{Mg}^{2+}$  counterions were all able to span across a 10 mm open gap. The first layer was the most critical layer in the bridge structure and showed the most variance between the different counterions. The subsequent layers were more accurate after the foundation from the first layer was established. The melt strands broke on several of the initial bridge roads printed using the  $\text{Na}^{1+}$  and  $\text{Mg}^{2+}$  materials and attached to the wall structure the nozzle reached. Once a few bridged roads were successfully established, the bridge was stable enough to hold shape over the unsupported gap for the following layers. The material shrinkage was an advantage for printing the bridge. Molten material would droop slightly across the open gap before the material cooled. Then the material would shrink and tighten the printed road creating a flat surface across the bottom of the bridge. Qualitatively, the bridge that printed the best was the material containing the  $\text{Ca}^{2+}$  counterion. The high viscosity, and the stronger divalent counterion interaction created a stronger melt strand as it stretched across the gap. This is indicative that the melt strength of the  $\text{Ca}^{2+}$  is higher than that of the other printed counterion materials.

To compare the “printability” of each SPEG material independent of the printing conditions, the same print parameters were used across all materials and printed part geometries. This was possible because the melting temperatures between the materials were very similar. However, finding the optimal print parameters for each material may yield different results in the printability. Regardless, the results presented in this work are expected to be generalizable due to the overall trends of  $\text{Zn}^{2+}$  counterion brittleness, the  $\text{Na}^{1+}$  counterion coalescing and shrinking, and the  $\text{Mg}^{2+}$  counterion coalescing. Brittleness and shrinking are difficult for the print parameters to influence.

Printing at a lower temperature may reduce coalescing; however, the temperature needs to be sufficiently high enough to ensure complete melting of the filament during extrusion.

## 2.4 Conclusions and Future Work

Four new semi-crystalline polymers were printed using FFF. Step-growth polymerization yielded SPEG with a  $\text{Na}^{1+}$  counterion, which was subsequently dialyzed to produce materials with varying cationic counterions ( $\text{Ca}^{2+}$ ,  $\text{Zn}^{2+}$ ,  $\text{Mg}^{2+}$ ). The different ionic interaction strength between the different counterions altered the material properties and thus the print quality of each material. The  $\text{Ca}^{2+}$  performed the best in printing due to a stronger ionic interaction strength compared to the other counterions. Using a divalent counterion over a monovalent counterion increased the melt viscosity by a magnitude, which was beneficial for the material's ability to hold shape while slowly cooling due to the small difference between the processing temperature and melting temperature. The increased nucleation density and small spherulites (radii  $< 10 \mu\text{m}$ ) in the  $\text{Ca}^{2+}$  counterion created stronger parts with less part curling, while the large spherulites (radii  $> 200 \mu\text{m}$ ) from the  $\text{Zn}^{2+}$  created material that was too brittle for practical use. Future work includes optimizing the printing parameters for each counterion species, which could yield better printed part accuracy and shape.

This work demonstrated how making small changes on the molecular level of an ionic polymer affect the melt and crystallization properties of the material, which influences the printability and final part properties of the material. These results contribute to what it means for a material to be FFF printable, where semi-crystalline materials are less common. The results enable development of new materials for the process of filament extrusion additive manufacturing.

### 3. Using different fillers to tune material properties of an ion containing semi-crystalline poly(ethylene glycol) for fused filament fabrication additive manufacturing processing

#### 3.1 Introduction

Additive manufacturing (AM) has become an increasingly common technology for creating prototypes, complex parts, and customized products. The applications for AM are expanding across a wide variety of markets including aerospace, automotive, and medical industry. Amorphous polymers, such as acrylonitrile butadiene styrene (ABS), have traditionally been proven chosen for processing via fused filament fabrication (FFF) [48] because its ability to flow and solidify with minimal expansion and shrinkage. However, to enhance the FFF materials library, researchers have strived to find techniques for modifying semi-crystalline polymers so they are able to be successfully processed [26]. For example recycled PET and PET blended with PP have been shown to be printable via FFF [49]–[51]. Such modifications are required because the discrete change in volume when the material crystallizes is less desirable for FFF as it causes residual stresses in the extrudate and ultimately, layer warping [51].

Pekkanen and coauthors developed a semi-crystalline sulfonated PEG polymer series that can be printed at 70 °C using FFF [24]. The semi-crystalline, low-melting temperature sulfonated PEG series was previously shown to be able to be printed into complex geometries [52]. Its low processing temperature and water solubility could find applications in direct printing of tailored pharmaceuticals [53] or in sacrificial support material for FFF [54]. In their evaluation of four sulfonated PEGs with varying counterions the authors identified that the ionic interaction of the  $\text{Ca}^{2+}$  counter-ion, poly(PEG<sub>8k</sub>-co-CaSIP), minimized shrinkage (due to smaller crystal sizes from a higher nucleation rate) and increased the melt viscosity such that the shape of the extrudate was maintained [52]. Although poly(PEG<sub>8k</sub>-co-CaSIP) produced the best results while printing, dialysis was required to ion-exchange the  $\text{Na}^{1+}$  counterion to a  $\text{Ca}^{2+}$  counterion (reaction shown in Figure 13) [24]. Unfortunately, reactions like this are difficult to scale-up in mass production in this polymer or a similar polymer that could be developed using this technique.

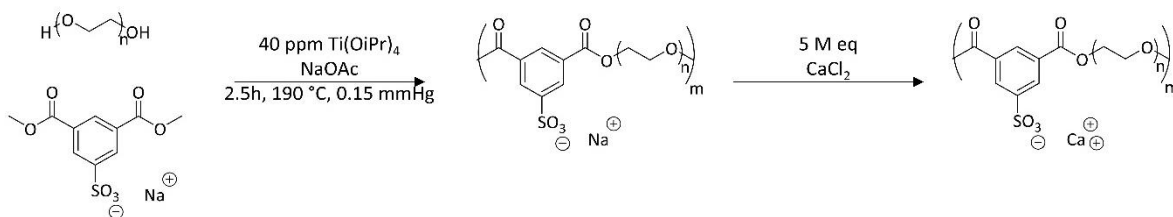


Figure 13: The one step chemical synthesis of poly(PEG<sub>8k</sub>-co-NaSIP) and two step chemical synthesis of poly(PEG<sub>8k</sub>-co-CaSIP) [24].

In this work, the authors test the hypothesis that adding fillers to the precursor material poly(PEG<sub>8k</sub>-co-NaSIP) can create similar material properties and crystalline structure to poly(PEG<sub>8k</sub>-co-CaSIP), and thus improve printability, without the need for an ion exchange, while maintaining the crystallinity of the material.

The use of additives to improve material properties for processing and application is common practice in sheet molding compounds for traditional injection molding applications [55], [56].

Additives can be used to modify melt flow [57], increase strength [58], and/or decrease warpage [59]. Fillers have also recently been incorporated in FFF filaments to alter material properties, such as shrinkage/warpage [60], rheology [61], or to add functionality, such as magnetic properties [62]. The size and shape of the filler additive contribute to the affected properties [63].

Within the context of manipulating properties of high molecular weight PEG, previous work has shown that adding an inorganic filler can alter crystallization kinetics without affecting the melting temperatures [64]. As a stronger ionic interaction between the  $\text{Ca}^{2+}$  counterions improved poly(PEG<sub>8k</sub>-co-CaSIP) printing [52], an ionic particle that physically reacts with the  $\text{Na}^{1+}$  counterion is predicted to be favorable in creating the higher melt viscosity and smaller spherulite size.

This study tests the effect of adding different ionic and non-ionic fillers to poly(PEG<sub>8k</sub>-co-NaSIP) to determine its effect on material properties and processing performance. The fillers were first mixed and screened by comparing the thermal and rheological properties in comparison to both poly(PEG<sub>8k</sub>-co-NaSIP), the control, and poly(PEG<sub>8k</sub>-co-CaSIP), the target. Two different fillers were selected to test printability to observe if the predicted improvements were seen in printing different features.

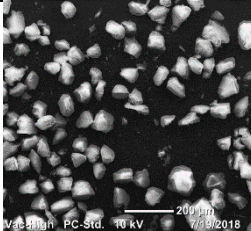
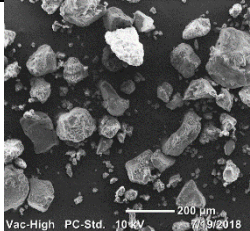
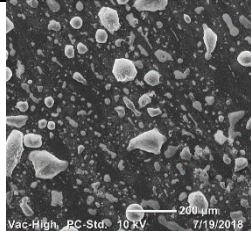
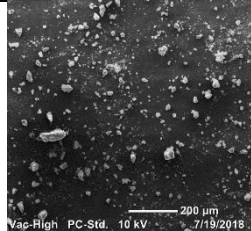
### 3.2 Methods

Poly(PEG<sub>8k</sub>-co-NaSIP) was compounded with two ionic and two non-ionic additives to observe their impact on the resulting composite thermal properties, viscosity, and crystallization kinetics. From these results, one ionic and one non-ionic filler were printed to compare the performance of the filled material in relation to the control and the target materials.

#### 3.2.1 Materials

The materials and synthesis steps for creating poly(PEG<sub>8k</sub>-co-NaSIP) and poly(PEG<sub>8k</sub>-co-CaSIP) are described in detail in Pekkanen's work using the same materials suppliers [24]. Additional materials used as fillers, SilicaFlash P60 (VWR), Starch1500 (Colorcon), CaCl<sub>2</sub> (Sigma-Aldrich), and CaCO<sub>3</sub> (Sigma-Aldrich) dried at 40 °C before use, in this study are listed in Table 3 along with their average diameter, and density. The particle sizes were measured using scanning electron microscopy (SEM) on a Joel NeoScope JCM-5000 Benchtop SEM, under high vacuum at a 10 kV accelerating voltage. An area of 3x3 mm was examined. Using Jeol measurement software, measurements from end to end of 10 different representative particles determined average particle sizes.

Table 3. SEM images of ionic and non-ionic fillers before mixing.

			
Silica (non-ionic) SiliaFlash P60 81±18 μm 0.6-0.7 g/cc	Starch (non-ionic) Colorcon: Starch 1500 124±104 μm 0.61 g/cc	CaCl <sub>2</sub> (ionic) Sigma Aldrich 85±36 μm 2.15 g/cc	CaCO <sub>3</sub> (ionic) Sigma Aldrich 32±22 μm 2.93 g/cc

### 3.2.2 Thermal Analysis

Differential scanning calorimetry (DSC) was completed by using a 50 mL/min nitrogen flow at 10 °C/min heating and 100 °C/min cooling rate using a TA instruments Q1000 DSC from -80 °C to 100 °C. Melting and crystallization temperatures were measured at the peak of the endotherm and exotherm respectively using the curve produced from the second heat. The second heat is chosen for discussion in order to directly compare the influence of filler on semi-crystalline morphology development. Differences between  $T_m$  measured in the first and second heats were found to be less than 5 °C. As the  $T_m$  is more than 10 °C below the nozzle temperature used, this difference does not affect printing. The percent crystallinity was calculated using 188.3 J/g as the theoretical enthalpy of fusion from PEG for a crystal of infinite size ( $H_f^\circ$ ) [65] normalizing for percent polymer content in the sample.

Isothermal crystallization experiments were also conducted using a TA Instruments Q1000 DSC. Samples were heated at 10 °C/min from room temperature to 100 °C, held isothermally for 5 min, and immediately cooled to a specified undercooling using the “jump” command in the TA thermal analysis software. Specimens were held at this temperature for 20 minutes to complete data collection. The limits of integration were determined by using the peak maximum during initial baseline establishment at the specified undercooling temperature and 15 s past the intersection of the lines tangent to the baseline and tangent to the second half of the crystallization peak. The time to reach 50% crystallized was determined through a running integral.

### 3.2.3 Oscillatory Rheology

A TA Instruments Discovery HR-1 parallel plates were used to measure rheological properties. The experiments were in a controlled temperature, air environment at 70 °C. Frequency sweep measurements were executed with angular frequencies ranging from 0.1 – 100 rad/s with a constant strain of 1%.

### 3.2.4 Crossed-Polarized Light Microscopy

Spherulitic growth of the material samples were observed via an Olympus BX51 microscope with crossed-polarizers and Linkam hot stage. Each material was melted at 70 °C and cooled naturally to room temperature on the Linkam hot stage to provide a similar thermal history for each sample. The material was then reheated and a video was collected during dynamic cooling of each sample at 80 °C/min to room temperature following a 1 min isotherm at 70 °C (i.e. nozzle temperature). These experimental conditions were selected to mimic printing conditions. Representative images from the video capture were taken at different time steps to explore spherulite size (the spherical semi-crystalline regions [66]) at different stages of crystallization. The crystallization is depicted by clipping the video capture to start from the time the first crystal was observed to grow, until there were no additional spherulite growth observed. The resultant video was then split into four time-equivalent sections to enable measurement of the rate of spherulite growth during crystallization. Using MatLab, the video frames were analyzed at different time steps to measure the diameter, where the radii was calculated from, of spherulites during crystal growth where the first spherulite was plotted in Figure 9 to provide understanding of growth rate.

### 3.2.5 Processing

The poly(PEG<sub>8k</sub>-co-NaSIP) was mixed with the different fillers on a desktop twin-screw extruder (Haake MiniLab II Rheomex CTW5). A low percentage of filler was desired in order to minimize the alterations to the original polymer and exploit any ionic interactions between the polymer and the filler. According to Allison et al, the molecular weights of each polymer is similar

and also polydisperse [24]. Because of the broad PDIs, the fillers were added by weight rather than by moles and keep the amount similar throughout the study. Polymer (4g) and powder (0.2g) were alternatively added to the extruder at 70 °C and the material cycled in the extruder for 10 min to produce even mixing. The 10 min mixing was verified to create evenly mixed material, by measuring rheology of several sections of multiple batches of the poly(PEG<sub>8k</sub>-co-NaSIP) with 5 wt% CaCl<sub>2</sub> filled material (which has a noticeable change in rheology, Section 3.3.2) and verifying the consistency in the viscosity profile. The material was then extruded and collected for testing. Following initial material screening analysis (Section 3.3.1-3.3.4) CaCl<sub>2</sub> and Silica fillers were selected for the printing analysis. Filament (~1.75 mm) was mixed and fabricated by an external resource using an industrial scale twin-screw extruder that has 5 heat zones. The inlet temperature is 65 °C and the outlet temperature is ~100 °C where the filament was air cooled on a conveyor belt.

The filament was printed on a custom desktop scale FFF delta style printer based off of the Kossel design using marlin firmware, nema 17 stepper motors, and an E3D hot end processed at 70 °C at 5 mm/s on a room-temperature print bed (as in [24], [52]). The gcode used for printing was created using Slic3r (version 1.3.0). The slight variation of the diameter of the filament was adjusted in the slicer settings for creating the gcode using caliper measurements. Several parts were printed to demonstrate different printable features while using the least amount of material.

### 3.2.6 Print Quality

#### 3.2.6.1 Tensile strength

Interlayer adhesion can be measured in various ways [36]–[38]. In this work, as in previous [52], a single road wall thickness (i.e. with no infill) prism with a wall length of 30.75 mm and 13.30 mm tall was printed. Each wall was cut apart and dogbone tensile bars were punched from each wall (n=5). The dogbones labeled XY indicated the dogbones were punch where the printed roads aligned with the direction of the tensile force. Dogbones labeled Z indicated the printed roads align perpendicular to the tensile force. The cross section was approximately 2.5 mm in width with thicknesses of ~0.39 μm (dictated by the road width) and the full tensile bar measured approximately 22.75 mm x 7.75 mm.

Pressed films were created to compare the printed material strength to the bulk material. Films were thermally pressed 70 °C and cooled naturally to room temperature. The films were pressed to 0.4 mm to match the printed specimen's wall thickness, by matching the nozzle diameter. Dogbones were punched from the pressed films in the same procedure as the printed specimens.

Ultimate tensile strength, elongation, and modulus of elasticity were evaluated using an Instron 5500R machine pulling at 5 mm/min. The cross-section was measured using a micrometer for each tensile bar to calculate the engineering stress. The thickness was measured by the road width and not the layer bonding thickness. The ultimate tensile strength was taken at the peak of the stress strain curve, the elastic modulus was evaluated where the linear region had a R<sup>2</sup> value of 0.99. The elongation was evaluated at the location where the slope dropped below -2 because several of the parts did not break clean where the material and/or layers ripped during breaking. The slope used was determined by inspection.

#### 3.2.6.2 Printed features

Five different features were printed from each material variant as in previous work [52]. The features tested consisted of a large and small, thin walled and solid structures, and a bridge across a gap. These were chosen to exhibit features that can be combined to create larger, more complex

parts, while using the least amount of material to test the printability. Both the small and large thin walled structures are solid models and were printed with parameters set to 0% infill with one perimeter wall. The small thin walled part has a progressively smaller circumradius to see how the material behaves when printing small continuous features. The printed hexagonal prisms, shown in Figure 13, used for tensile specimens served as the large thin walled part. Both solid parts were printed using 90% infill setting. A 100% solid infill was not used because the filament had slight variation in diameter, which can cause the issue of overfilling at 100% density infill. A bridge was printed to span a 10 mm gap on top of two solid pillars. The bridge was printed using three 0.2 mm layers. Dimensions of the CAD features are shown in previous work[52].

### 3.3 Results and Discussion

#### 3.3.1 Thermal Characterization

DSC results shown in Figure 14 elucidate how the fillers affect the melting or crystallization temperatures of the poly(PEG<sub>8k</sub>-co-NaSIP). The broad melting peaks are characteristic of polydisperse polymers. Polymers synthesized through step-growth polymerization usually experience a PDI of 2, which could manifest varying lamellar sizes and thus broadening the melting peak [24]. The average of different material melting temperatures was  $55.8 \pm 1.2$  °C and the crystallization temperatures were  $30.9 \pm 1.8$  °C. The  $T_g$  was previously measured for PEG and the SPEG series to be significantly lower than room temperature ( $\sim -44$ °C), and was therefore not a focus for this research as all FFF processing occurred at and above room temperature [24]. In the context of FFF, the fillers did not significantly change the transition temperatures. There is a  $24.8 \pm 2.5$  °C gap between the melting temperature and the crystallization temperature. Although this is an artifact of the processing conditions used to run DSC, it is important to note that the material does not crystallize precisely at the same temperature that the material melts. Another important note that the melting temperature varies slightly for poly(PEG<sub>8k</sub>-co-NaSIP) and poly(PEG<sub>8k</sub>-co-CaSIP) from previous work [24], [52], this is thought to be a slight variation due from different synthesis batches. Section 3.3 provides a further analysis of this phenomenon by showing the crystallization half times. The non-ionic fillers both produced taller and narrower melting and crystallization peaks, the cause of this is currently unexplored; however, the variation in the nominal temperatures are small ( $< 2$  °C) compared to poly(PEG<sub>8k</sub>-co-NaSIP). The ionic fillers did show a slight decrease in the percent crystallinity, produced a percent crystallinity more similar to the target material poly(PEG<sub>8k</sub>-co-CaSIP) (Table 4).

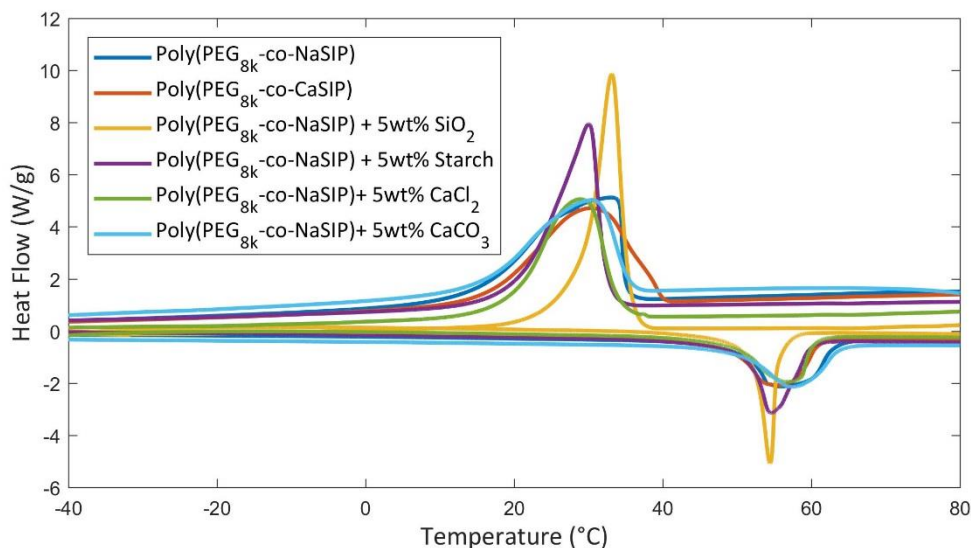


Figure 14: DSC for the base polymer, poly(PEG<sub>8k</sub>-co-NaSIP), and target polymer property, poly(PEG<sub>8k</sub>-co-CaSIP), and the poly(PEG<sub>8k</sub>-co-NaSIP) containing different fillers. Exotherm up.

Table 4: The thermal properties extracted from the DSC curve, including the melting temperature, crystallization temperature, and the percent crystallinity (n=1).

Material	T <sub>m</sub> (°C)	T <sub>c</sub> (°C)	Crystallinity (%)
Poly(PEG <sub>8k</sub> -co-NaSIP)	55.8	33.0	58.9
Poly(PEG <sub>8k</sub> -co-CaSIP)	55.5	30.2	53.4
Poly(PEG <sub>8k</sub> -co-NaSIP) + 5 wt% SiO <sub>2</sub>	54.4	33.1	56.7
Poly(PEG <sub>8k</sub> -co-NaSIP) + 5 wt% Starch	54.6	30.0	59.6
Poly(PEG <sub>8k</sub> -co-NaSIP) + 5 wt% CaCl <sub>2</sub>	56.8	28.8	52.6
Poly(PEG <sub>8k</sub> -co-NaSIP) + 5 wt% CaCO <sub>3</sub>	57.4	30.4	52.5

### 3.3.2 Rheological Properties

All of the filler materials increase the viscosity of the base polymer poly(PEG<sub>8k</sub>-co-NaSIP), following Poslinski's theory, where increased filler volume fraction increases the viscosity [57]. The SiO<sub>2</sub>, starch, and CaCO<sub>3</sub> filler increase the viscosity up to 69% from poly(PEG<sub>8k</sub>-co-NaSIP). CaCl<sub>2</sub> filler increases the viscosity to match the poly(PEG<sub>8k</sub>-co-CaSIP) with a 95% confidence level. This magnitude increase in viscosity, using the same wt. % filler, is likely the result of an ionic interaction between the Na<sup>1+</sup> counterion in poly(PEG<sub>8k</sub>-co-NaSIP) and the CaCl<sub>2</sub>. Ionic fillers can be used as a plasticizer for non-polar polymer chains with multiplets, where the separation of ionic domains allows for increased molecular mobility and increases the crystallization rate [67]. Here, the opposite effect is observed. The ionic filler is creating a stronger ionic interaction and limiting the molecular mobility of the polymer. The CaCl<sub>2</sub> filler may be forming crown ethers similar to the Ca<sup>2+</sup> counterion in poly(PEG<sub>8k</sub>-co-CaSIP) [24].

Once it was determined that the  $\text{CaCl}_2$  had increased poly( $\text{PEG}_{8k}$ -co- $\text{NaSIP}$ )'s viscosity, a second test was conducted to quantify the effect  $\text{CaCl}_2$  concentration in poly( $\text{PEG}_{8k}$ -co- $\text{NaSIP}$ ). Figure 15b shows the relationship between  $\text{CaCl}_2$  concentration to the viscosity. There is an exponential relation ( $R^2=0.97$ ) between the  $\text{CaCl}_2$  concentration and the viscosity. Batches containing 15% and 20%  $\text{CaCl}_2$  were also made; however, the oscillatory rheometer was unable to complete the test because the viscosity exceeded the upper limit of the instrument. For this work, 5 wt%  $\text{CaCl}_2$  will be used, as the rheological properties match that of poly( $\text{PEG}_{8k}$ -co- $\text{CaSIP}$ ) (~10,000 Pa·s zero-shear viscosity).

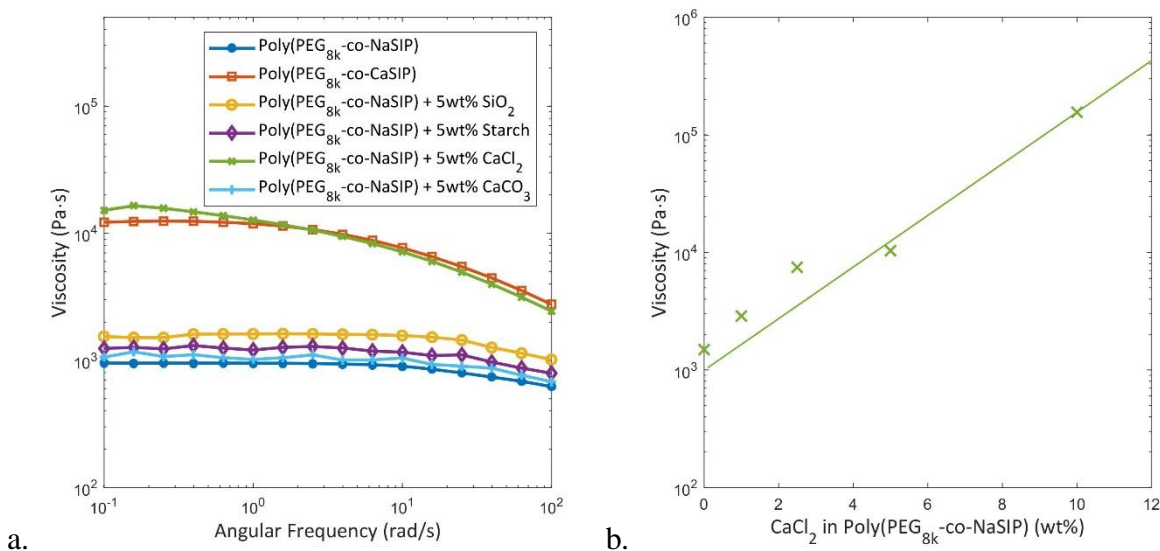


Figure 15: Oscillatory rheology of the SPEG materials (a) compared to the poly( $\text{PEG}_{8k}$ -co- $\text{NaSIP}$ ) with 5 wt% filler material at 1% strain and (b) the poly( $\text{PEG}_{8k}$ -co- $\text{NaSIP}$ ) with different wt% of the  $\text{CaCl}_2$  at 1% strain and near zero shear  $\sim 0.1$  rad/sec ( $n=1$ ).

### 3.3.3 Crystallization

Cross polarized microscopy of the polymer cooling from printing temperature ( $70^\circ\text{C}$ ) to room temperature ( $25^\circ\text{C}$ ) was video recorded and quantified to investigate the crystallization process, as depicted in Figure 16. Figure 17 depicts the spherulitic growth rate based on image analysis of the micrographs in Figure 16. Generally, fillers will be in the amorphous regions of the material [68]. The poly( $\text{PEG}_{8k}$ -co- $\text{NaSIP}$ ) grows spherulites to the size of  $132 \pm 41 \mu\text{m}$  at an average growth rate of  $6.5 \pm 1.8 \mu\text{m/s}$  under these conditions. Poly( $\text{PEG}_{8k}$ -co- $\text{CaSIP}$ ) grows to a spherulite size of  $< 10 \mu\text{m}$  and grew faster than the poly( $\text{PEG}_{8k}$ -co- $\text{NaSIP}$ ), but the rate was unable to be precisely measured due to the small size and rapid growth of the crystals. The authors hypothesize that the high nucleation rate and small spherulite size prevent printed parts from warping during solidification and shrinkage of the poly( $\text{PEG}_{8k}$ -co- $\text{CaSIP}$ ). This hypothesis of the importance of small spherulites is also supported by the observed spherulite size of commercial poly (lactic acid) filament (PLA), the most common printable semi-crystalline for FFF, which has been measured to be between 27-42 nm [69]. As the material crystallizes the ordering of the polymer chains cause the material to condense and shrink inward. The spherulites are comprised of crystalline and non-crystalline regions that are interconnected. Larger crystals cause a larger region of material to condense inward, as the crystals grow radially from the nucleation cite [66]. By increasing the nucleation sites and allowing smaller spherulites to form, the condensing and shrinking of the

material is discretized allowing the polymer chains to condense locally and effectively “pinning” the road dimensions in place. This effect can also be seen in injection molding, where adding a nucleating agent reduces the warping and deformation [70]. This reduces the internal stresses within the material as the melted regions do not have to travel as the spherulite grows.

All of the fillers decreased the spherulitic growth rate except starch, and all except  $\text{CaCl}_2$  increased the average spherulite size when compared to the unfilled poly(PEG<sub>8k</sub>-co-NaSIP). Spherulite radii in the silica and  $\text{CaCO}_3$  filled materials were measured to be  $144 \pm 35 \mu\text{m}$  and  $195 \pm 52 \mu\text{m}$  respectively. The starch filler spherulites were too large to be precisely measured in the field of view of the microscope, but were observed to be  $>190 \mu\text{m}$ . The largest change in spherulite size and growth rate was  $\text{CaCl}_2$  whose spherulites radii were smaller, measuring  $51 \pm 13 \mu\text{m}$ , where the rate of spherulite growth was slower than all the other materials at about  $1.0 \pm 0.5 \mu\text{m/s}$ .

The reduction in spherulite size, growth rate, and total crystallization time are favorable for FFF for this material. The smaller spherulites reduce the effect of curling because there will be less internal residual stress from the larger continuous spherulites growing and shrinking on top of the previous layer. Slower spherulite growth rates allow for more time to nucleate new spherulites as the material is cooling and nucleating faster, helping to decrease spherulite size through earlier impingement. A reduced total crystallization time creates a slower transition between the melt and solid state of the material. This allows the material to remain molten longer to improve the bonding potential[36] to the next layer, and a slower crystallization process allows the polymer to create a more gradual transition between the melt and solid properties, rather than a fast transition which may cause greater internal stress during the layer-by-layer printing process. This may not be the case for materials with lower viscosity; however, the high viscosity of the  $\text{CaCl}_2$  filler allows the material to hold shape in the melt, which allows for the decreased crystallization rate without effecting the shape.

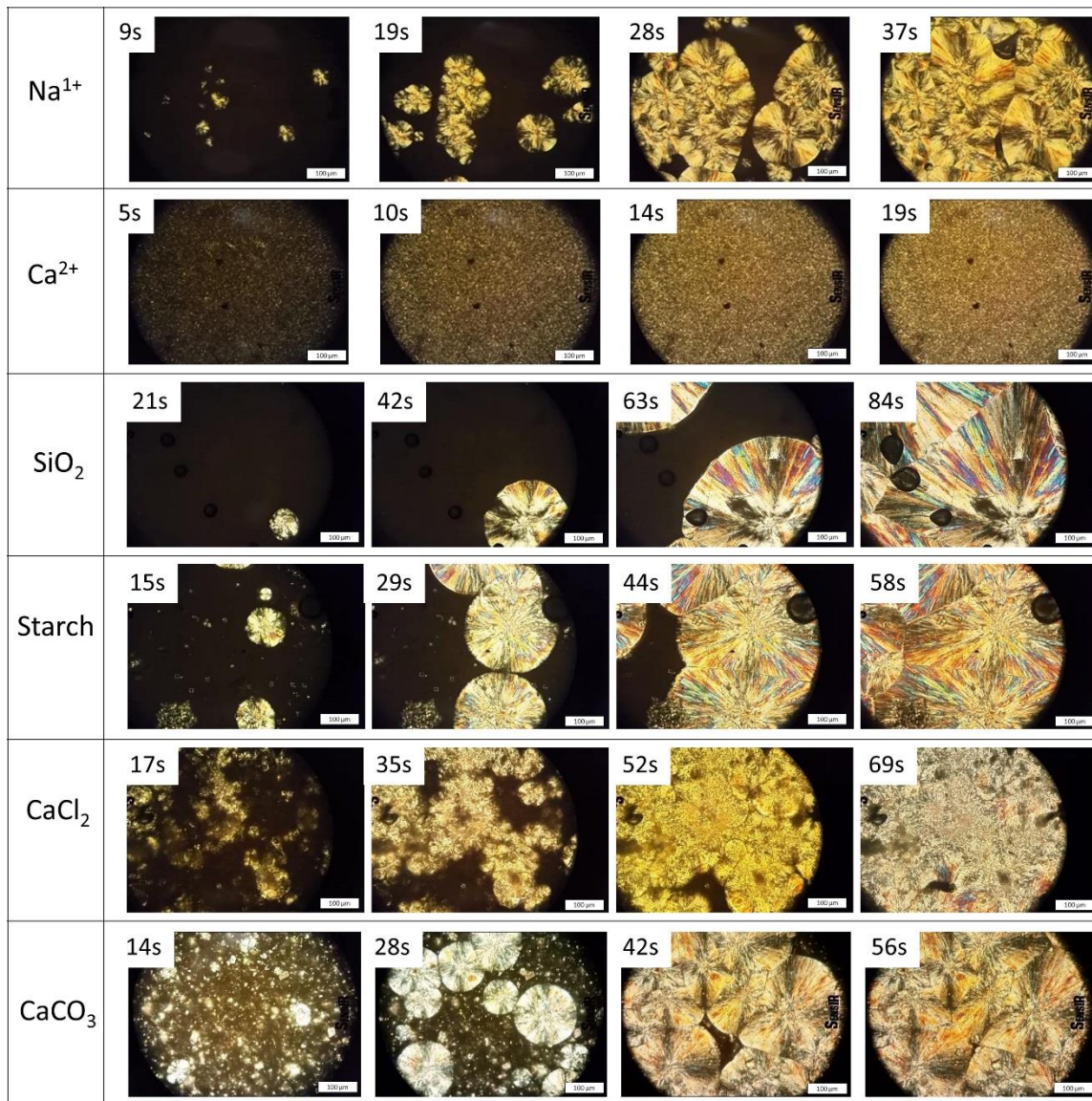


Figure 16: Crystallization of the polymers cooling from 70 °C to 25 °C shown at 4 different time stamps using cross polarized light microscopy on an Olympus BX51 microscope with a linkam hot stage. The scale bar shows 100 μm.

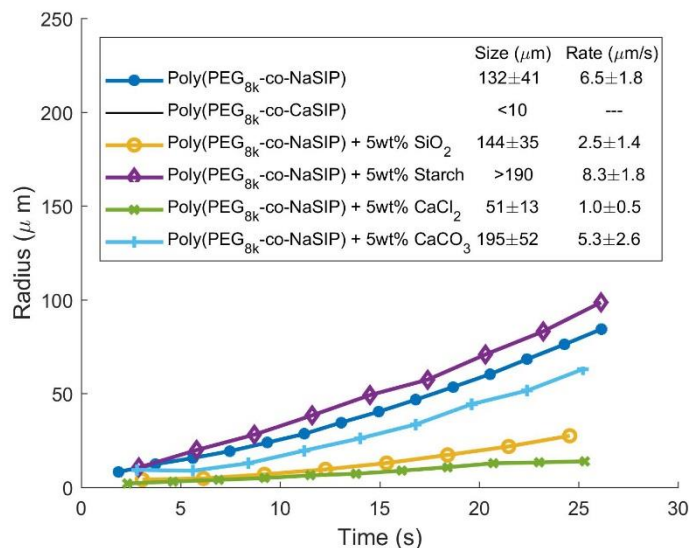


Figure 17: The spherulite growth measured from microscope images at different instances in time (n=1).

The nonlinearity of the spherulitic growth rates plotted in Figure 17 is due to the non-isothermal temperature conditions imposed on the samples during measurement. These non-isothermal conditions better mimic the FFF printing process than idealized isothermal conditions. The concave up shape of the curve are expected as the spherulitic growth rate will increase as time continues and the temperature decreases.

The isothermal crystallization halftimes presented in Figure 18 further characterize and differentiate the influence of the investigated filler materials on crystallization kinetics. The crystallization halftimes measured from DSC are a bulk characteristic of the material while the growth rate measured via microscopy is based on a small, representative population of spherulites. As a result, the DSC-based halftimes contain coupled information about nucleation and growth rates, whereas the image analysis only contains information about the growth rate following nucleation of a stable spherulite. The difference between all the sample's crystallization halftimes diminishes as the isotherm approaches lower temperatures. This is consistent with published literature, which states that the polymer backbone has a larger influence on chain mobility as temperature decreases compared to the filler particles or the pendant ionic groups [28]. The small difference between print temperature and ambient temperature creates a slow cooling rate [52]. Figure 18 shows the most difference in crystallization kinetics among the sample set above 45 °C, which is the most process relevant portion of the figure, due to the slow cooling rate.

The purpose of this experiment is to compare the filler materials to the non-filled poly(PEG<sub>8k</sub>-co-NaSIP) and the poly(PEG<sub>8k</sub>-co-CaSIP) which showed improved printing. The fast crystallization that is seen in poly(PEG<sub>8k</sub>-co-CaSIP) is due to the high nucleation rate and density, as depicted in Figure 16. The total crystallization rate for the ionic fillers is increased across the measured temperatures when compared to the control, despite the slower spherulite growth that was observed during the cooling of the material. Therefore, the ionic fillers cause an increase in nucleation rate which outpaces the reduction in molecular mobility caused by ionic interactions between the ionic groups and between these groups and the filler particles. The non-ionic fillers caused a decrease in the crystallization rate. This could be caused by the non-ionic fillers

interrupting the spherulite growth as the material crystallizes, causing a slight reduction in the crystallization halftime.

Due to instrument limitations, Figure 18 only represents the nucleation-controlled regime of the total crystallization rate as a function of isothermal crystallization temperature trend. The difference in crystallization halftimes increases as the isothermal crystallization temperature increases. This implies that the fillers have more influence over nucleation kinetics than over growth kinetics.  $\text{CaCO}_3$  has the shortest crystallization halftime of the filled materials in the high temperature range (44-49 °C in Figure 18), meaning it is the most effective filler material at nucleating crystalline regions flowed by  $\text{CaCO}_3$ . The  $\text{SiO}_2$  filled material is like the unfilled control, while the starch filled material is observed to prevent nucleation with respect to the unfilled control. These crystallization kinetics are further supported by Figure 16 and the low number of observed spherulites for the starch filled material, and the increase in number of spherulites in the  $\text{CaCO}_3$  and  $\text{CaCl}_2$  sample.

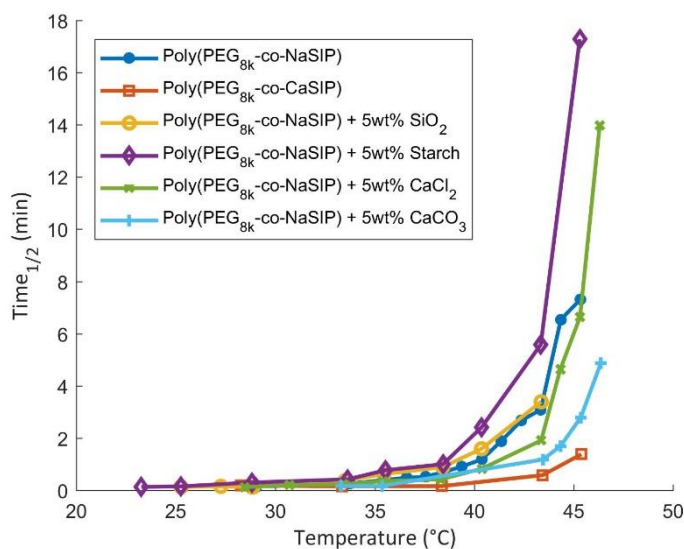


Figure 18. Crystallization halftimes versus isothermal temperature for four filled materials and unfilled control (n=1).

### 3.3.4 Tensile

Two fillers were selected for printing, one ionic and one nonionic. This was done in order to best address the hypothesis that adding an ionic filler, would alter poly(PEG<sub>8k</sub>-co-NaSIP) material properties, and thus the printing, to mimic poly(PEG<sub>8k</sub>-co-CaSIP) in order to produce a printable material with a reduction in the synthesis steps.  $\text{CaCl}_2$  was chosen because it matches the viscosity and crystallization behavior of poly(PEG<sub>8k</sub>-co-CaSIP) better than the  $\text{CaCO}_3$ .  $\text{SiO}_2$  and Starch measured more similar to poly(PEG<sub>8k</sub>-co-NaSIP) than poly(PEG<sub>8k</sub>-co-CaSIP) in material properties.  $\text{SiO}_2$  was chosen as the control to investigate whether changes in the printability are due to the ionic interaction from  $\text{CaCl}_2$  and not physical interactions from any added particle.

The elastic modulus and ultimate tensile strength of  $\text{CaCl}_2$  improved as predicted from the material properties (Figure 19). The poly(PEG<sub>8k</sub>-co-CaSIP) has a larger elastic modulus and tensile strength compared to the poly(PEG<sub>8k</sub>-co-NaSIP). The same trend is seen between the  $\text{SiO}_2$  and the  $\text{CaCl}_2$  filler material. The printed Z specimen for the  $\text{SiO}_2$  filler elastic modulus was greater than the film or printed XY specimen. The authors believe this is attributed to the z layers initiating a tear and the layer being peeled apart creating an artificial higher elastic modulus. This was

consistent with all of the SiO<sub>2</sub>/Z specimens. The printed XY tensile specimens for the CaCl<sub>2</sub> filler elongate longer than the film specimens for the same reason as poly(PEG<sub>8k</sub>-co-CaSIP), where bond between the roads break during plastic deformation before the roads break [52]. This is because the material is above glass transition temperature at room temperature and the ionic interaction of the formed crown ethers exist in the amorphous region of the polymer where they contribute to the strength.

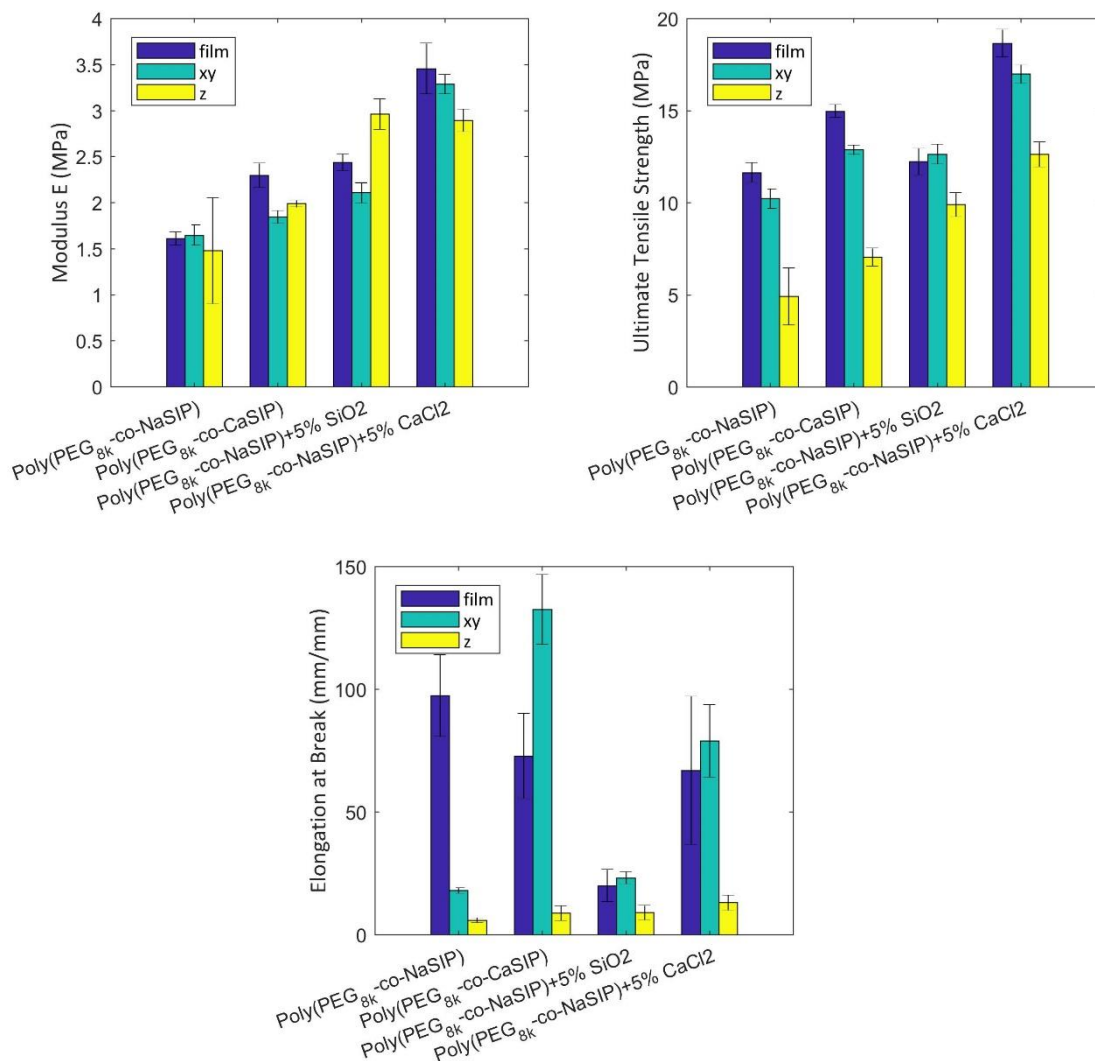


Figure 19: Tensile properties of the sPEG materials in comparison to the poly(PEG<sub>8k</sub>-co-NaSIP) with fillers looking at both pressed films and printed tensile properties (n=5).

### 3.3.5 Printing Quality

Figure 20 shows printed features from SiO<sub>2</sub> and CaCl<sub>2</sub> filled poly(PEG<sub>8k</sub>-co-NaSIP) and compares the quality to poly(PEG<sub>8k</sub>-co-NaSIP) and poly(PEG<sub>8k</sub>-co-CaSIP). Both fillers reduce the part curling when printing the large solid part. This is consistent with previous literature that suggests that fillers in filament can reduce part warpage [60]. The authors hypothesize that the

slower spherulite growth rate allows more time for the molten polymer to fill voids created within the road from the crystallization shrinkage.

For the small thin walled part, the  $\text{CaCl}_2$  filled material printed the most accurate part with clearly defined corner features. The other three materials lost definition because the material lost shape when the small previous layer had insufficient cooling time. However, the  $\text{CaCl}_2$  filled material was able to hold its shape better in the melt state to create a clearly defined feature. The increased viscosity contributed to the material's ability to hold shape during solidification; however, the authors hypothesize that melt surface tension contributed to this result due to  $\text{CaCl}_2$  filled material having the same viscosity as the poly(PEG<sub>8k</sub>-co-CaSIP).

Comparing the small solid cube, both fillers improved the printability. The poly(PEG<sub>8k</sub>-co-NaSIP) expanded and coalesced between neighboring roads while printing, losing resolution to the internal geometry of the part and ultimately failing when the material expanded into the print head [52]. The  $\text{SiO}_2$  material does not have as defined roads as the poly(PEG<sub>8k</sub>-co-CaSIP) or the  $\text{CaCl}_2$  filler; however, the material did not expand into the part and fail. This may indicate that the  $\text{SiO}_2$  filled material does not thermally expand as much as the poly(PEG<sub>8k</sub>-co-NaSIP), similar to perlite-filled polypropylene [60], or has less die swell.

The first layer of the printed bridge had the most variation because of the material crossing the open gap. All of the materials were successful by the second and third layer after there was material to support the subsequent layers. The  $\text{CaCl}_2$  filled material performed the best, where the material was able to cross the open gap without the melt strand breaking or significantly drooping. The difference between the  $\text{CaCl}_2$  filled material and the poly(PEG<sub>8k</sub>-co-CaSIP) was the shape of the pillars used to hold up the bridge. The  $\text{CaCl}_2$  filled material printed the small feature with better definition, without tilting inward as the print head moved from one pillar to the other. This was expected based on the small thin walled part losing definition at the top with the small cross sectional area for poly(PEG<sub>8k</sub>-co-CaSIP). Poly(PEG<sub>8k</sub>-co-NaSIP) and the  $\text{SiO}_2$  filled material both had lower zero-shear viscosity resulting in the first layer of the bridge drooping slightly and some road strands breaking. As the material cooled and shrank, the connected drooping roads did tighten, resulting in a more level first layer. The slow crystallization rate, as seen in the crystallization half times (Figure 18), of poly(PEG<sub>8k</sub>-co-NaSIP) and  $\text{SiO}_2$  filled material may also contribute to unsuccessful bridging roads.

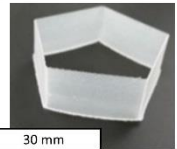
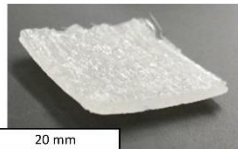
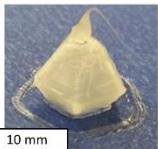
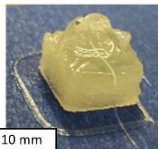
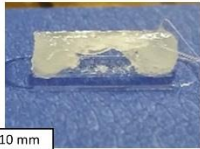
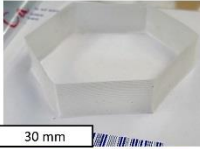
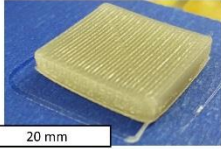
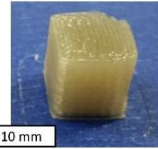
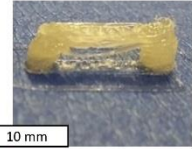
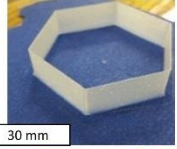
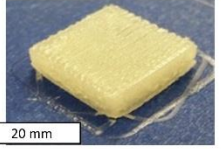
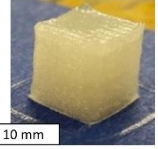
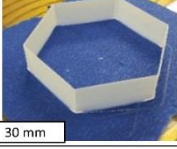
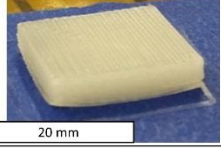
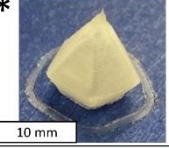
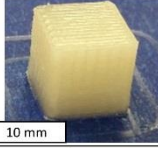
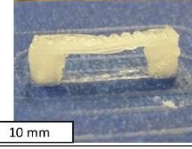
	Large thin wall part	Large 90% solid wall part	Small thin wall part	Small 90% solid part	10mm bridge
Na <sup>1+</sup>			* 		
Ca <sup>2+</sup>			* 		
SiO <sub>2</sub>			* 		
CaCl <sub>2</sub>			* 		

Figure 20: Printed features to compare the difference between the different materials printability. (\*Printed slower at 2 mm/sec)

### 3.4 Conclusion

This research demonstrates the use of fillers in FFF, where ionic interactions between a polymer and a filler can be used to influence the material properties and crystallization to enable and improve FFF printing of a polymer. A CaCl<sub>2</sub> filler was used in the ionic semi-crystalline polymer poly(PEG<sub>8k</sub>-co-NaSIP) to improve the mechanical properties and printability. Poly(PEG<sub>8k</sub>-co-CaSIP) had improved printed part quality over poly(PEG<sub>8k</sub>-co-NaSIP) because of the stronger ionic interaction within the polymer. CaCl<sub>2</sub> additives interact ionically with the pendant sulfonate groups resulting in the same increase in zero-shear viscosity and similar reduced spherulite size as the poly(PEG<sub>8k</sub>-co-CaSIP) material, which is known to be printable. These changes allowed for the poly(PEG<sub>8k</sub>-co-NaSIP) the ability to hold shape in the melt at low temperatures and reduce part curling. The CaCl<sub>2</sub> slowed the rate of crystallization, in contrast to poly(PEG<sub>8k</sub>-co-CaSIP), this is favorable because it makes the transition more gradual between melt and solid states in a similar manner to amorphous materials.

Using additives to alter material properties for processing is a common practice in material extrusion and injection molding of plastics. This technique can be used to enable FFF printing of additional semi-crystalline polymers by tuning mechanical and rheological properties along with crystallization kinetics. While the experiments in the work focused on using an ionic filler with an ionic polymer to improve printability, relations between a material's crystallization and printability lay the groundwork for studying crystallization kinetics and the molecular-scale polymer morphology formation in developing and modifying semi-crystalline polymers for FFF. There is potential for future work in how different filler types and geometries affect the material properties and how small changes in the material properties affect the overall printability.



## 4. Embedding of liquids into water soluble materials via additive manufacturing for timed release

### 4.1 Introduction

Additive manufacturing's (AM) layer-wise fabrication process has been shown to provide a cost-effective way to customize product geometry based on the specific needs of an individual. AM's ability to customize parts has given the medical industry the ability to customize treatment to the patient such as in prosthetics [71], replacements [72], and tissue scaffolds [73]. The ability for AM to provide custom, on-demand products has also been explored as a means of providing personalized medicine. AM possesses the ability to selectively control the deposition of multiple materials on a voxel-by-voxel basis, allowing for more complex customization of both geometry and composition of oral dose medicine.

To enable personalized medicine via AM, there have been many studies investigating different matrix materials that successfully incorporate active agents [74]–[77]. Recent studies have demonstrated the use of AM to control the amount of a drug inside an oral dose by either tailoring the concentration of the drug or size of the pill [78]–[81]. AM has also allowed for the fabrication of a single dosage tablet that incorporates multiple active ingredients [11], [21], [80]–[83].

Another advantage AM can bring to the pharmaceutical industry is rapid dissolution and instantaneous release of dosage tablets. For example, Spiritam uses binder jetting AM to create fast-dissolving pills for treating epilepsy and myoclonic seizures. The fast dissolution is achieved due to the water-soluble binding agent and the porosity of the powder part that allows for water penetration. The Food & Drug Administration (FDA) approved Spritam in August 2015 and is the first 3D printed pill approved for oral consumption [84].

AM of pharmaceuticals has the potential to realize tablets with a programmable tailored release of active ingredients. For example, Gupta et al. extruded poly(lactic-co-glycolic) acid (PLGA) solution and then directly injected emulsion ink into the aqueous core. The PLGA solutions contained different lengths of plasmonic gold nano-rods (AuNRs). The printed part released the emulsion ink by using a laser to excite the nano-rods and ruptures the part [85].

In this study, achieving a programmed release of active ingredients is accomplished via the solubility of the printed polymer matrix material in water. Controlling both the amount of material deposited and the overall shape of the printed part provides opportunity to tailor the drug release profile. Karasulu et al. have shown how different solid 3D shapes, including a cube, pyramid, and sphere, alters the release profile and how the shape changes, becoming more spherical, as the parts dissolve [86]. Goyanez did similar work using AM to fabricate and dissolve different solid geometries [87] and infill percentages [88]. Studies have shown how the release profile can be affected by complex part geometries such as a torus [89], convex and concave surfaces [90], lattice geometries [91], [92], and alternating two materials inside the part's internal geometry [93]. By enabling embedding of liquid/powder active ingredients into printed voids/chambers, more complex release profiles (e.g. multi-stage, multi-material) can be achieved.

In general, while fused filament fabrication (FFF) AM provides strong, robust parts, its use of high temperatures (~190-260 °C) prevents the inclusion of many active ingredients as they typically become inactive at temperatures above 100 °C. This requires the use of actives that are thermally stable for FFF processing [12]. To circumvent this limitation, the active ingredients can be incorporated inside of the printed part through an embedding procedure, rather than mixed within the filament material. The embedding of liquids into parts has been demonstrated in-situ FFF [15], [16], [94] and in post-processing [17] by depositing the active ingredients into printed

void spaces within the part. Schmitz et al. used liquid embedding with FFF to create a sensor for detecting tilt motion using a standard PLA material [94]. Okwuosa and coauthors performed work in creating an automated system for embedding active ingredients inside of a soluble part [16]. Okwuosa's automated embedding showed the release of theophylline; however, the shells created were 1.6 mm thick, as thinner walls would leak the embedded liquid. The resulting release profile shows that the theophylline might be leaking, where the rate of release was altered through wall thickness, but there was no delay in release. Okwuosa's previous work in creating a capsule with a solid polymer infill (instead of a liquid) does create a delay in the release profile; however, the delay is the same for the various thicknesses above 0.5 mm that were tested [95]. Maroni was able to change the release time using different thicknesses; however, the internal material was added as a post-processing step and was only demonstrated using powder [96]. While progress has been made in this research area, the lack of integrated, liquid-embedding design guidelines and FFF toolpath control have prevented demonstration of (i) a delayed release of a printed part with embedded liquids, and (ii) a part with embedded liquids that feature wall thicknesses comparable to soft gelatin capsules (0.56-1.14 mm) [97].

The focus of this paper is to present and demonstrate a method for FFF of thin-walled liquid-tight printed parts, allowing for a larger variety of tailored delayed release profiles. The overall goal of this work is to explore how the time of the release of an embedded liquid can be controlled by varying the wall thickness of a printed capsule. The first research objective is to present a method for embedding a liquid into a thin-walled encapsulated void processed by material extrusion using a water-soluble polymer (Section 4.2). The second objective is to study the relationship of wall thickness to the time the internal liquid is released. Finally, the third objective is to demonstrate the controlled release of parts with a different wall thickness and shape, and a multi-release capsule, containing two liquids or a liquid and a powder that allows for the two distinct delayed releases.

## 4.2 Embedding into Fused Filament Fabricated Parts

Embedding of foreign non-printed materials in AM is the process of printing a part around embedded preexisting components. Embedding takes advantage of cheap, reliable, previously manufactured components and AM-enabled complex 3D geometries. Meisel et al. discuss the embedding of parts during an AM build process in four general steps [98].

- The part is designed with a void corresponding to the embedded component.
- The print is paused at the top layer of the void during the printing process.
- The embedded component is inserted into the designed void.
- The print is resumed on top of the embedded component.

This general process has been used to embed solid objects such as electronics [99], batteries [100], and RF components [101]. In this work, the general AM embedding process is extended to the concept of embedding liquids into printed thin-walled parts. This process follows the general process described by Meisel, with the exception that the print is not paused; instead, the liquid is embedded in-situ as the material is being printed, as described in Section 4.3.4 (Figure 21).

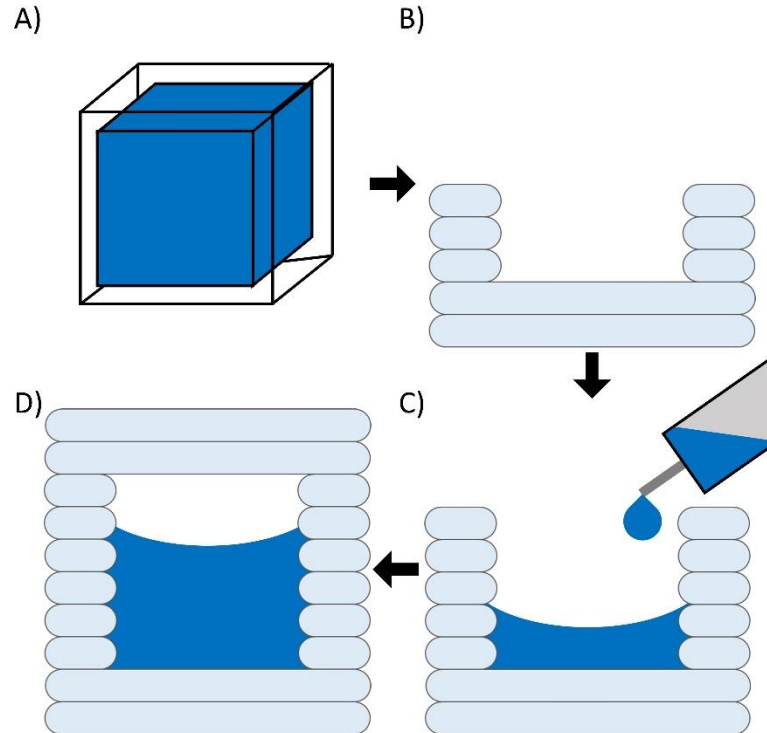


Figure 21: The general process for embedding where a) a part is designed with an internal void, b) the part is partially printed, c) the liquid is inserted during printing, and d) the embedded component is enclosed inside of the printed part. (Based on Meisel’s steps for embedding [98])

#### 4.2.1 Design Considerations for Embedding Liquids into Fused Filament Fabricated Parts

There are several design considerations unique to embedding a liquid into FFF parts including the need for self-supporting structures, continuous printing, and accounting for shrinkage and thermal stresses of the printed material.

- *Self-supporting structures:* In AM, part orientation and sacrificial support structures are used to enable the fabrication of overhanging and bridging features. Structures with enclosed voids often need support material to support the deposition of material that spans the top of the enclosure. Typically, a soluble material is used as a sacrificial material for support structures in FFF; however, when the build material itself is soluble, dissolving the support would also dissolve the part. Insoluble support structures can also be used, but require manual removal of these “breakaway” structures, adding an extra post-processing step, and the removal process may cause enough damage to the part to break the liquid seal. Therefore, designing part geometries to feature self-supporting structures are important in creating parts capable of retaining an embedded liquid. This can be achieved by either using materials that can successfully bridge large gaps due to their high melt viscosity or by designing the geometry to angle inward to enclose a void. For material to bridge a gap, the material must hold an intended shape across the gap without a support structure and properly bond between the roads creating the bridge structure [41]. A single layer bridging an enclosure will not be liquid-tight without special adjustments to the process parameters (such as overlapping roads); therefore, to create a liquid-tight seal, the bridge must be at least two layers thick. Self-supporting structures designed by angling the structure inward

so that the roads of each layer connect with the roads from the previous layer (this occurs for angles greater than  $\sim 20\text{-}30^\circ$  from horizontal).

- *Liquid-tight seal:* Standard FFF slicing software outputs an extrusion toolpath that must discontinue and then resume extrusion numerous times throughout the printing of a complex part. At these start/stop points, the extruded material does not bond well with the start part of the extruded line. The weak bond can introduce small gaps that create porosity in the part, preventing the part from being liquid-tight [102]. The tool path can be modified to create a continuous printing loop where the end of one layer continues into the next layer. This prevents leaks that can occur from start/stop defects. Another modification could be an extra extrusion of material at the seam (where the start and stop points of the material extruded around the perimeter meet), or overlapping material across the seam, but this can result in a loss of dimensional accuracy and tolerance stack-up if not done precisely.
- *Preventing delamination:* As the extruded thermoplastic material cools, it solidifies and shrinks. If a pause is used during the print, like in previous AM embedding research, there is a weaker bond due to the reduced molecular diffusion between layers [103]. As the layers shrink, internal stress is put on the part, which causes parts to curl, or layers to delaminate. Delaminated layers cause leaking between the layers when exposed to liquid. One way to prevent this issue is to print small parts where the thermal expansion of the material and the resulting residual stresses are less significant. Another way to prevent this issue is to not pause extruding for embedding and instead embed during the print (to prevent the delamination defects caused by cooling of extruded material) to ensure a strong bond between layers.

### 4.3 Methods

The general process for creating water-soluble printed capsules to control the release of the embedded liquid into water is shown in Figure 22. First, the material was processed from Mowiflex pellets (1) into filament (2). The filament was then printed via AM material extrusion FFF to create capsules (3). A liquid that simulates an active ingredient was embedded into the designed void space of the printed capsule during the printing process (4). The final printed part was subsequently dissolved in water (5), at which point the release of the embedded liquid was measured (6). The release of the embedded liquid is controlled by tuning the wall thickness of the printed part capsule.

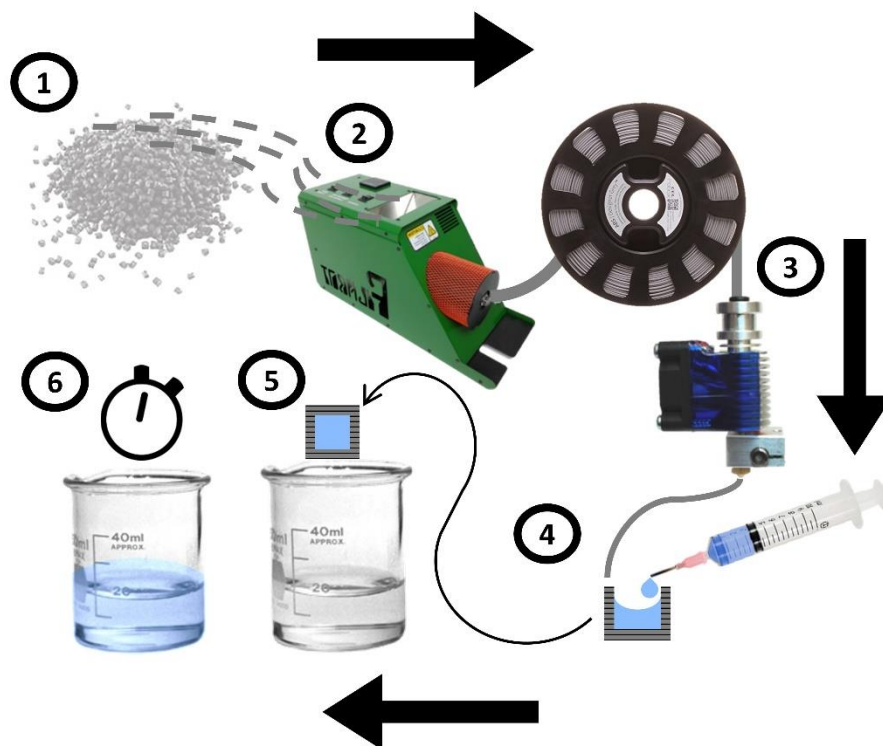


Figure 22: A process diagram for 1-2) creating filament, 3) printing the filament into a hollow capsule geometry 4) in-situ embedding a liquid into the capsule and 5-6) timed dissolution of the printed capsule.

#### 4.3.1 Materials

A PVOH-based polymer, Mowiflex 3D 2000 (previously referred to as Mowiflex TC 253), made by Kuraray, was chosen for this study as it can be processed via traditional material extrusion and injection molding and is water-soluble. Mowiflex is adequate for achieving the goals of this study: (i) demonstrating embedding a liquid with active ingredients inside a printed, water-soluble container and (ii) demonstrating tailored dissolution through both toolpath and geometry. This material provides the opportunity to embed active ingredients into a material with a high melting temperature. Liquid from a Tide POD® (containing actives) was used for the embedding process because of its color (allows for machine-vision tracking of the release of the actives it contains Section 4.3.7), and because it doesn't dissolve a water-soluble material since it is used in a similar context (i.e., the original Tide POD® packaging is a water-soluble polymer).

To determine print parameters, the material was characterized using Thermogravimetric Analysis (TGA) and Differential Scanning Calorimetry (DSC). TGA was performed on a TA Instruments TGA Q500 at 10 °C/min from 23 °C to 550 °C (Figure 23A). TA Instruments Q2000 DSC was run using a heat/cool/heat cycle from -80 °C to 200 °C at a heating rate of 10 °C/min and quench cooled at 100 °C/min (Figure 23B). Data was used from the second heating cycle, where the melting temperature was determined to be 177 °C.

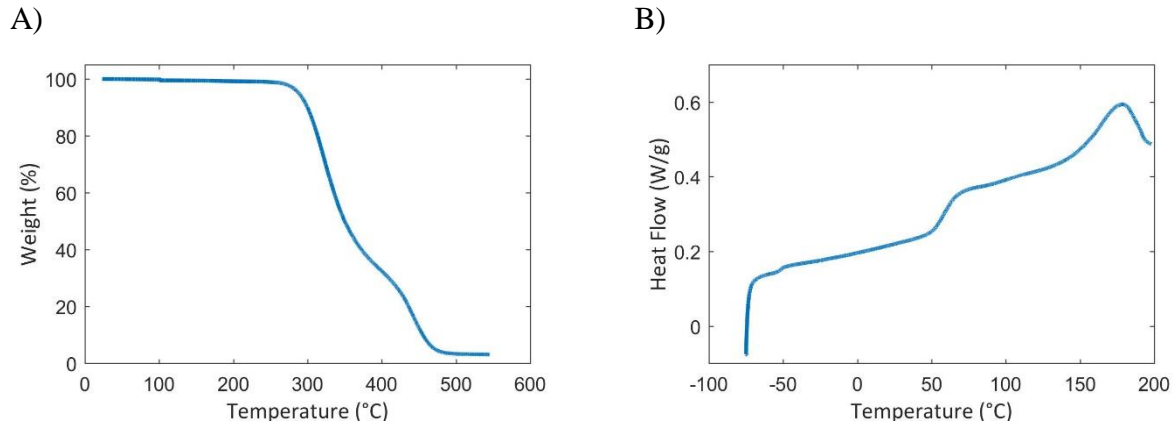


Figure 23: The thermal characterization of Mowiflex using A) TA Instruments TGA Q500 at 10 °C/min from 23 °C to 550 °C and B) TA Instruments Q2000 DSC from -80 °C to 200 °C second heat cycle at a heating rate of 10 °C/min.

The acceptable print temperature range is above the glass transition temperature but below degradation temperature. A 1% degradation occurred at 244 °C (Figure 23A), which is used as an upper limit for the nozzle temperature. The melting temperature (177 °C) is the minimum temperature that must be used in order to allow the material to flow. Typical FFF materials process using a nozzle temperature of at least 10-20 °C above the melting temperature to decrease the viscosity [69]. While the material remains above the glass transition temperature (~50 °C), polymer chain entanglement can occur between the printed layers, bonding the roads together [44].

#### 4.3.2 Filament Processing

The filament was made using a single screw desktop-scale extruder (Filabot Wee, Filabot, Barre VT). The processing temperature for creating the filament was 198 °C, and the extruder ran at a constant speed of 35 rpm. A 2 mm die was used, along with a drawing system to draw the extruded filament to a target diameter of 1.8 mm. The diameter of the filament typically varied less than 0.1 mm; however, the slicing parameters for printing were adjusted to the actual filament diameter for each part.

#### 4.3.3 Fused Filament Fabrication Printing

The material was printed on a custom delta-bot style FFF printer, driven by Marlin firmware. The printer uses an off the shelf hot end (E3D-v6, E3D), with the drive motor located close to the head for processing softer filaments. As informed by the DSC results (Figure 2), the material was printed at 215°C, with no bed heating. The part was printed on blue painter’s tape to ensure adhesion to the bed and to allow for easy removal from the bed.

#### 4.3.4 Liquid Embedding

The liquid was injected during the printing process via a disposable plastic 10 mL syringe. Small amounts of liquid were injected every few layers, without pausing the print. The injections started once the print reached 20 layers (out of 50). The liquid was injected in small quantities so that the liquid would not touch the most recent 3-5 layers.

This technique was developed through experimentation. Pausing during the print to inject the liquid tended to cause delamination in the subsequent layer. This occurs as the embedding layer cools; when the print is resumed, the bonding potential lowers for the subsequent layer [103]. The

difference in bonding between layers caused the part to create a very small crack that was not always visible. These cracks appeared between an hour to overnight to form, causing the liquid to leak. This indicated that the crack in the layer was caused by residual stresses from the part shrinking and cooling. Injecting the embedded liquid all at once also led to cracking. This injection effectively caused the printed layers to cool too quickly and prevented sufficient bonding with subsequent layers. This is less of an issue for powder embedding because the powder does not conduct heat as efficiently to cool the printed material.

#### 4.3.5 Powder Embedding

The powder embedding was also done in-situ (without pausing the print), similar to the liquid embedding. However, powder embedding has advantages over embedding liquid as it could i) begin after the bottom layers were printed (before 20 layers, which was needed for liquid embedding), ii) be added in larger quantities (because the powder is less thermally conductive), and iii) be filled to the top of the void (because there was no curvature caused by surface tension and it could act as a support for the top enclosure). The powder embedding process was performed by-hand using a scoopula with table salt (NaCl) and was used as a preliminary means to test the viability of embedding a powder. This was done to demonstrate the ability to embed using a powder or combination of powder and liquid where the liquid remains separated from the powder.

#### 4.3.6 Test Specimen Geometry Design

A cube-shaped test specimen was designed to allow the exploration of how different wall thicknesses of thin-walled structures affect dissolution time. The part design was guided by the design considerations from Section 4.2.1 for material extrusion of a water-tight part. Specifically, top and bottom walls were designed to be one printed layer (0.2 mm) thicker than its walls because the thickness of the first bottom layer is highly dependent on very precise nozzle calibration and the first layer on the top is not liquid-tight. A cube was chosen in order to ensure accurate measurements of the wall thickness. The walls were measured on parts printed with identical print settings to verify that they met the design specifications.

Programmable release was demonstrated by varying the number of roads used for the printed part. The external dimensions of the printed cubes were kept constant across all specimens, while the wall thickness was varied to be one, two, and three roads thick. The wall thickness for dissolution was calculated assuming the printed roads formed an obround shape (Figure 24) [104].

$$w_{thickness} = w_{design} - \pi * \frac{h}{4} \quad [1]$$

where  $w_{thickness}$  is the width of the layer interface (the thinnest point of the part),  $w_{design}$  is the multiple of the road width used, and  $h$  is the layer thickness (set to 0.2 mm for all of these tests).

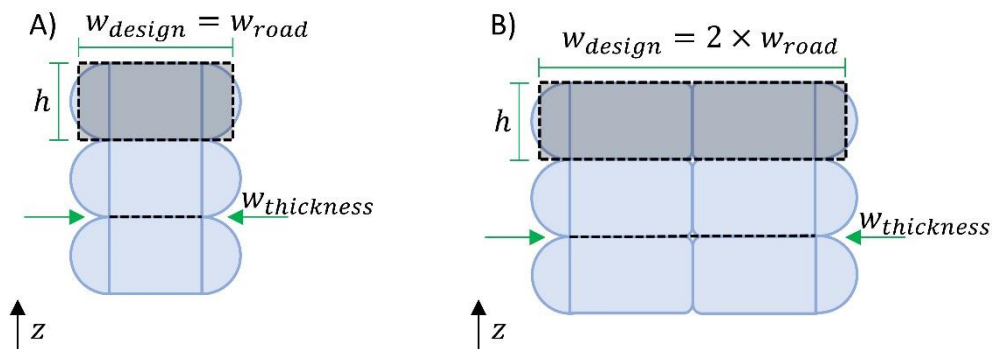


Figure 24: The assumed cross-section shape of stacked printed roads, where the top gray box represents the assumed shape, for A) one road thick and B) two roads thick printed walls

The size of the cubes was 10x10x10 mm. The amount the printer extrudes for each road was calculated using the nozzle diameter as the road width (0.4 mm), the layer height (0.2 mm), the length of the road, and the filament diameter. The filament diameter was measured and adjusted for every print. The print speed was set to 180 mm/min.

The gcode was generated using a custom Matlab script (R2017a) to create toolpaths for the parts because it allowed for more precise control of the toolpath. The custom toolpath was used to create continuous extrusions, without any start/stops of the extrusion within, and between, layers. Figure 25 shows the toolpaths used to create the parts where the start/stop locations are adjacent to each other or directly across a printed layer (for walls that are more than a single road). This technique could also be extended to more complex 3D shapes (rather than shapes that are 2D extrusions) by angling the walls inward or outward each layer.

For these experiments, the starting and stopping of extrusion only occur between the perimeter and the infill for the top and bottom of the structure. At these times, a small amount of material is extruded (0.2 mm) to intentionally “ooze” slightly, which helped in creating a more consistent seal by not stopping the extrusion completely.

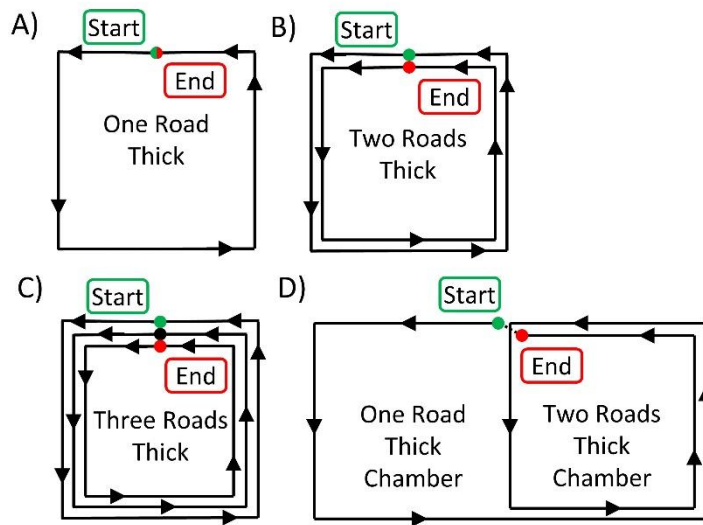


Figure 25: The outline of the continuous toolpath for each layer of the parts with walls that are A) one road thick, B) two roads thick, and C) three roads thick. D) Shows a multi-chamber part containing two chambers that are one and two roads thick. (the top and bottom layers are infilled).

#### 4.3.7 Dissolution measurement

As the goal of this work is to assess how AM can tailor the release of a liquid encapsulated in a water-soluble part, dissolution measurements were focused on the time of release and not on the release profile. The printed part with embedded liquid was placed in a sinker suspended in the center of the water-filled 250 mL beaker and the stir bar was offset (for imaging purposes) and set to 400 rpm. As the part dissolved, the embedded liquid released into the water, changing the color. Images of the surrounding water against a white background were taken by a digital camera (GoPro Hero3) every 5 seconds to record the water color. The images were then processed via Matlab's

image processing functions to assess the changes in its color (i.e., when the liquid from the printed part is released). For each image series, a consistent square section inside the beaker (color swatch) and outside the beaker (blank swatch) were first selected (Figure 26). The squares were then separated into mean RGB values. To eliminate noise in the data, the color swatch RGB values were subtracted from the blank swatch and the absolute value was taken. As the blue liquid is released from the interior of the printed part, the blue RGB value increases (or the red and green values increase, because of the change in blue and using absolute values). The release is tracked by measuring the change in the RGB values of the image sequence over time. The release time is defined by when the change in one of the RGB values exceed a threshold (set to 2). The threshold was chosen to be the lowest number that sufficiently did not trigger early from noise in the data for all of the printed specimens.

The release of the multi-chamber parts was calculated by identifying the first release, then finding a new baseline RGB value 2000 s after the first release and subtracting the new baseline from all of the following data and looking for values that cross the threshold again to document the second release.

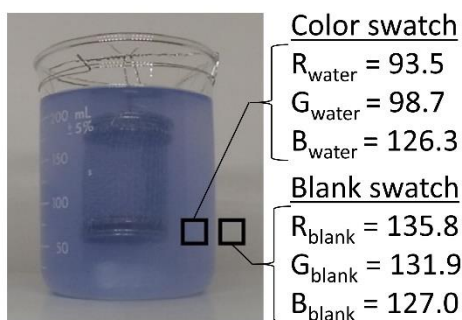


Figure 26: An example of a dissolution image with the color swatch and blank swatch RGB values used to detect the release time.

## 4.4 Results/Discussion

### 4.4.1 Dissolution vs wall thickness

Using the procedure defined above, five test specimens of each wall thickness variant (one, two, and three roads thick) were successfully fabricated without liquid leaking. Dissolution testing demonstrates delayed liquid release with increasing wall thickness, as shown in Figure 27. Figure 28 shows the average release for each wall thickness. During testing, a few cubes exhibited excessive agitation (i.e., collided with the walls of the sinker) caused by movement in the suspended sinker, which resulted in an early release and were omitted from the data. It was assumed that the diffusion of the color pigment through the part was insignificant and that the color would be released immediately.

Previous research shows that the dissolution profile of a solid cube could be approximated as a linear trend (for the first ~60% of the dissolution) followed by an asymptotic trend [87]. The dissolution of the cube capsules is expected to follow this release profile until a wall is broken and the internal liquid is released. The volume of the cube capsules is equivalent to 22%, 41%, and 56% of a solid cube for walls that are one, two, and three roads thick respectively because of the designed internal void. Therefore, the time of release is modeled as a linear fit using the averages, intersecting with the origin, resulting in an  $r^2$  value of 0.97.

The individual data points had a maximum error of 16%, 29%, and 41% from the trend-line for the parts' walls that were one, two, and three roads thick respectively. The variation in the data of the thicker cubes could be the result of i) less liquid, ii) thicker walls, or iii) variation in the filament. i) The single road wall structure had the largest internal void, containing the highest volume of liquid, which results in a faster more distinct change in the water color compared to the thicker walls with less liquid, that is more easily tracked programmatically. ii) The thicker walls also experience a thicker layer of diffusion of water, before the material dissolves, which softens/weakens the walls resulting in a more unpredictable release. Also, the shape of the part with thicker walls has a higher volume of material and may be experiencing the change in shape (such as the smoothing of corners) that occurs when dissolving solid shapes [86], [105]. iii) Finally, the filament diameter may also cause slight variations, where the small variability in the filament will result in a small variability in the deposition. Parts using more filament are susceptible to more variation.

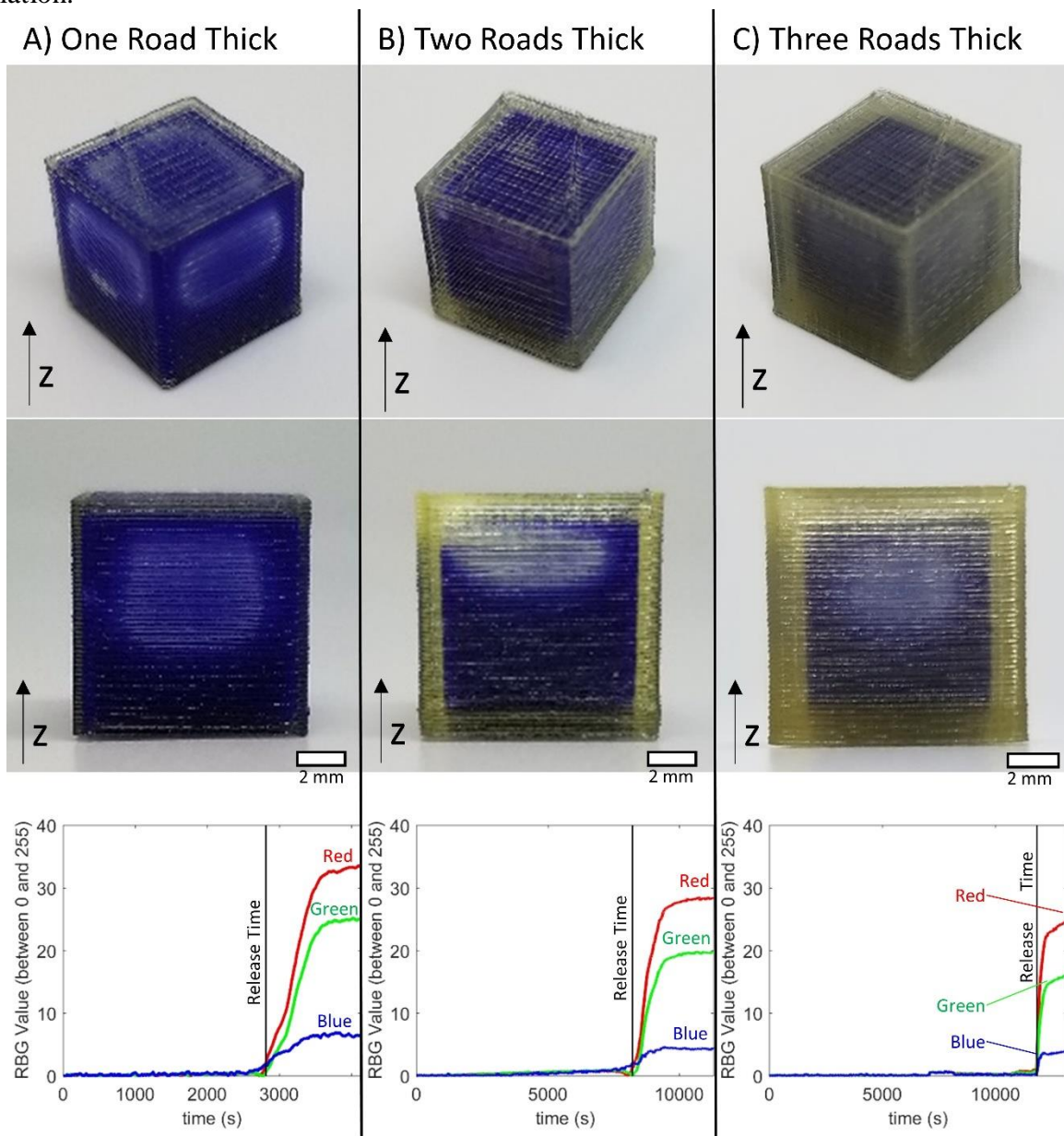


Figure 27: The time of release for the capsules with wall thicknesses of A) one road, B) two roads, and C) three roads, where all of the cubes are 10x10x10 mm in size. The vertical line indicates where the predetermined release threshold was crossed for the release time measurement.

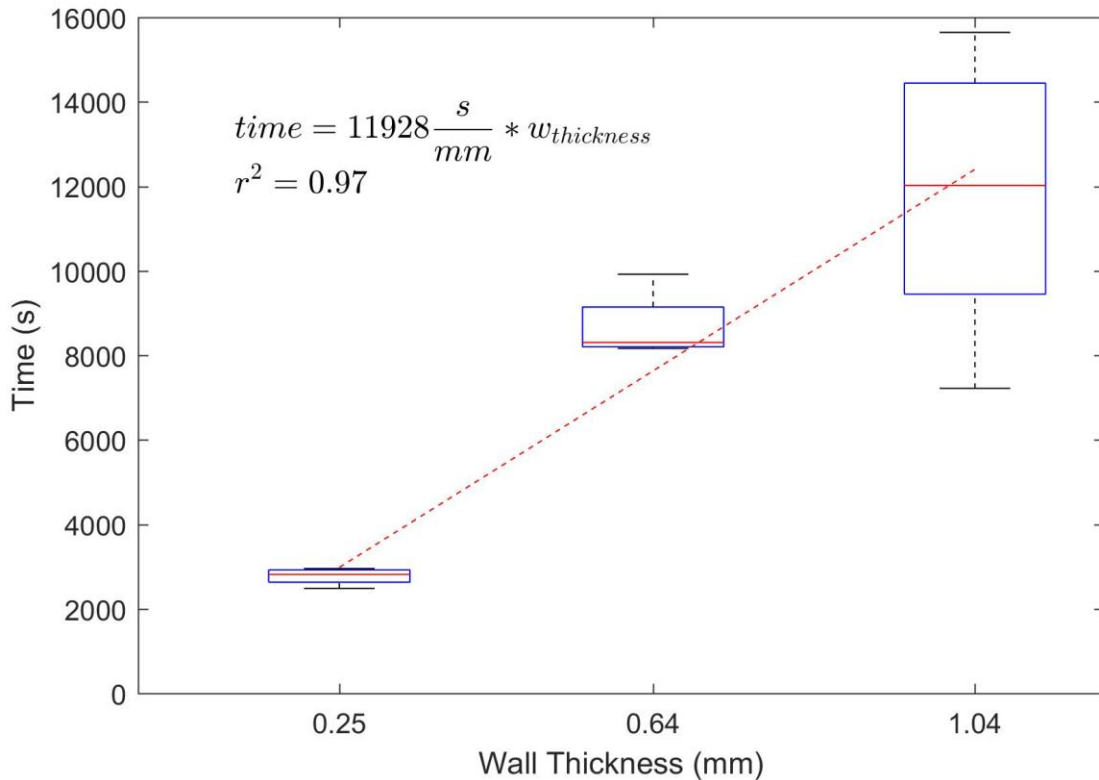


Figure 28: Box and whisker plot of the release time of specimens with a wall thickness of one, two, and three roads. The trend line is plotted using the averages of the respective measurements.

#### 4.4.2 Controlling release

Using the linear trend identified in Figure 28 as a release model, a desired release rate can be predicted and controlled by tailoring the wall thickness. Several shapes were designed with different wall thicknesses, including an over-extruded road resulting in a road width that is 1.5 times the nozzle diameter, a shape change using an angle, and a multi-chamber release. The parts were then dissolved, and the release time was measured.

##### 4.4.2.1 Thick walls

Figure 30A shows a printed cube with the over-extruded road, where the calculated wall interface width is 0.6 mm (equation 1). The result from the printed part's liquid release time is 12% above the trend-line (Figure 31,) which is within the variation measured in the single road cubes (maximum 16% from the trend-line).

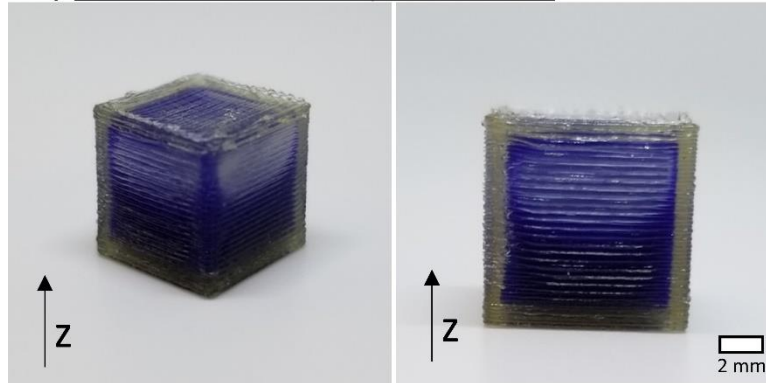
##### 4.4.2.2 Angled Geometry

Three parts, which were used for the preliminary study, were designed with angled walls (30°) and varying wall thickness (Figure 30B) [15]. The release times were plotted in Figure 31 using the wall interface calculation (Equation 1) and accounting for the wall angle. The release time was

calculated using the method described in Section 4.3.7. The results do follow the trend line where the average of the angled thicknesses of 0.13 mm, 0.53 mm, and 0.93 mm are off by 7%, 25%, and 5%, respectively. The variation in the angled part with two roads thick (0.53 mm) had the largest variance. This is likely the result of an early release caused by increased viscous forces from the water because most of the parts with two roads settled closer to the stir bar (where the velocity of the moving water is higher) during dissolution as a result of their movement not being constrained to a suspended sinker.

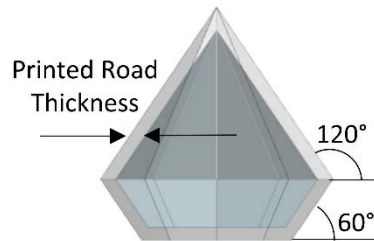
It is worth noting that the surface area of these structures are different from the cubes, and the method used slightly less water (200 mL) and did not use a suspended sinker [15]. When dissolving a solid part, the surface area to volume ratio alters the rate of dissolution [87]. However, for dissolution of thin-walled capsules, the dissolution of the thinnest part of the wall is the critical dimension since release is identified by the embedded liquid seeping through the dissolved wall. This is important because it allows for the comparison of these parts with different volumes and surface areas, even though they have different volumes and surface areas, and provides opportunities to alter these aspects independent of release. This element of the experimental design holds because the walls are not too thick (in which case the deformation of the shape could alter the release time [86]) and the concentration of the water will not become too saturated (which could decrease the rate of dissolution [90]).

### A) Over-extrusion by 1.5 times



### B) Angled Geometry

Designed



One Road Thick



Two Roads Thick



Three Roads Thick



Figure 29: Varying shapes used to test the release profiles with A) an over extruded road wall to be 1.5 times the nozzle diameter on the cube ( $10 \text{ mm}^3$ ) and B) a capsule design using a  $30^\circ$  angle with varying wall thicknesses, where the volume is constant, but the surface area changes [15].

#### 4.4.2.3 Multi-chamber release

Using the toolpath described in Figure 25, double chamber cubes were produced to create multi-substance, multi-release parts. Figure 30 shows a printed part featuring two chambers embedded with yellow liquid (for the liquid filled) or salt (for the powder/liquid filled) in the chamber that is one road thick and blue liquid in the chamber with two roads thick.

The resulting release profile from using two liquids is depicted in Figure 30, showing two distinct release profiles. Figure 31 shows the release times for these specimens as a function of

wall thickness. The first release was, on average, 18% longer than the previously identified dissolution rate. The authors believe this is caused by the structure with two roads created more stability in the part as the single road wall dissolved, which resulted in a slightly delayed release. The average of the second release has only a 6% delay from the previously determined trend line (Figure 28). This was slightly unexpected because, using the assumptions in Figure 24, two single walls would result in a slightly smaller thickness (0.5 mm) than a wall containing two adjacent roads (0.64) due to the road shape. The later release could be the result of the fact that once the liquid from the first chamber is released, the chamber does not immediately collapse. Instead, it holds some shape for a period of time, while the remaining wall dissolves. This would cause the inner wall to experience less viscous forces from the water stirring for a short time (due to the remaining walls from the single road chamber protecting the inner wall, reducing the velocity of the water), decreasing the dissolution rate. Lastly, Figure 30 also shows a demonstration of how this technique can be used for embedding powdered materials. The liquid/powder capsule did not exhibit any leaking from the liquid into the powder creating a multi-release structure where actives can be incorporated in different forms within the same part.

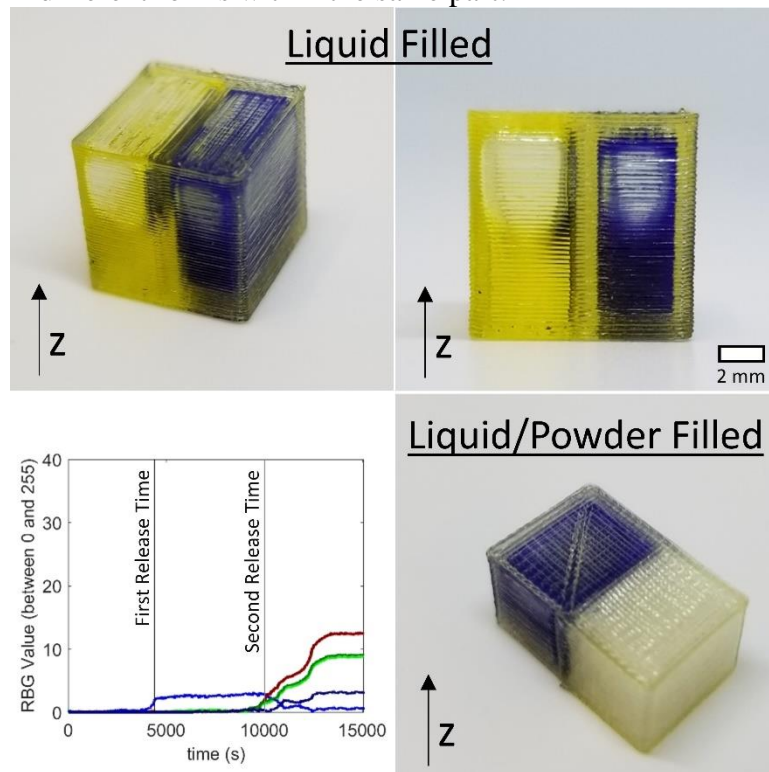


Figure 30: A capsule containing two chambers (using the toolpath described in Figure 25). The top images are of the cube (10x10x10 mm) with liquid embedded inside each chamber where yellow has a one road thick wall and blue has a two-road thick wall. The graph shows an example of the tracking of the delay in release for the two chambers. The liquid/powder filled part is a larger double chamber (10x16x10 mm) that contains the blue liquid and a powder material (NaCl).

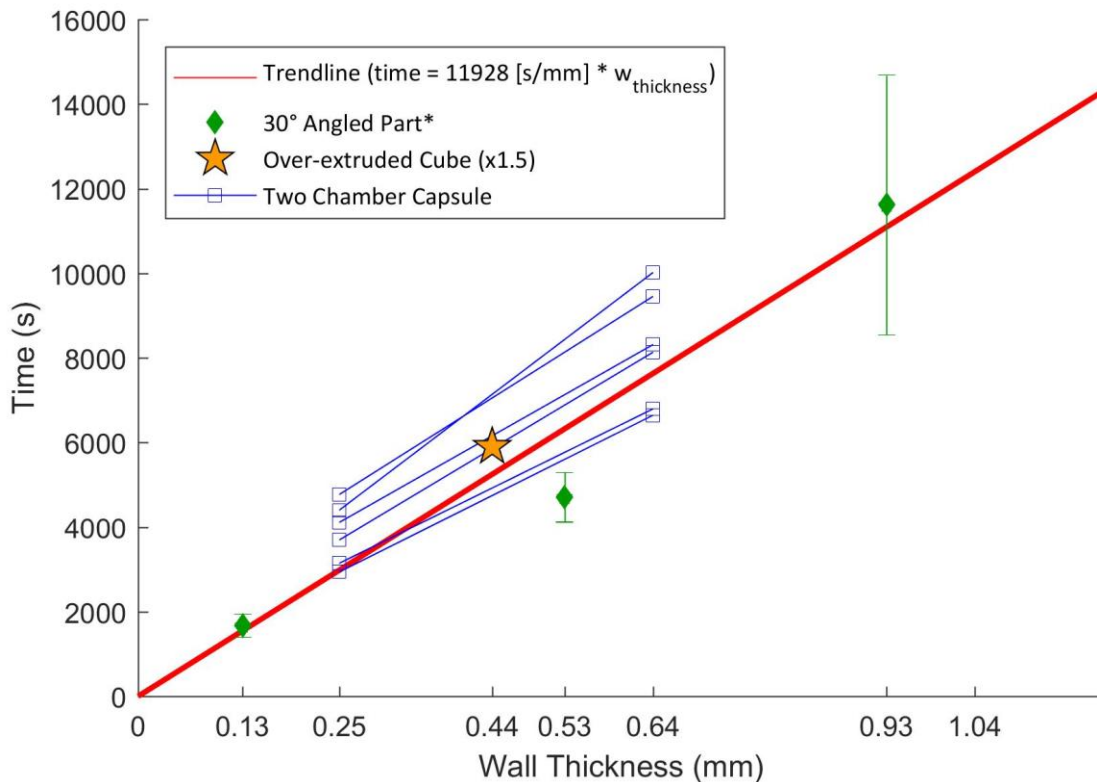


Figure 31: The release time for the varying shapes in comparison to the trend line created from the cube specimens. The over-extruded part had  $n=1$  and the angled parts had a minimum of  $n=3$ . The multi-release from the two chamber capsules are marked with a line between the first and second release. (\*Data from previous experiments, with slight variation in dissolution method [15])

#### 4.5 Summary & Future Work

This work demonstrates a process for in-situ embedding liquids and powders into a water-soluble, liquid-tight printed part via FFF. Design considerations were established for creating liquid-tight structures using self-supporting structures, creating a liquid-tight seal, and preventing delamination.

The ability to tailor the delayed release of an embedded liquid by tuning the printed wall thickness was also demonstrated. The time of the release of the embedded liquid is a function of the wall thickness of the enclosed void. Control of precise time was also demonstrated by changing the processing parameters (via over-extrusion) and the shape (incorporating angles). This allows for further tuning of the release time of the encapsulated liquid. Finally, a methodology for printing a continuous-extrusion multi-chamber part was developed and used to demonstrate a multi-release profile for two embedded liquids and the demonstration of a part containing both liquid and powder.

Future work includes developing more complex geometries using FFF and investigating how the shape affects the release profile. This would allow for the ability to further customize parts for personalized medicine and/or tailored release applications.

## 5. Design of a low-cost, high-temperature build environment for a fused filament fabrication

### 5.1 High Temperature Fused Filament Fabrication

#### 5.1.1 Introduction

Fused Filament Fabrication (FFF), a type of material extrusion additive manufacturing (AM) technology, has the largest market install base of all AM systems [3]. FFF has been used for the fabrication of functional prototypes, tooling, and end-use parts in industrial (e.g., automotive, aerospace, medical), educational, and hobbyist markets. The small size, and inexpensive desktop FFF machines effectively democratize manufacturing by providing users access to AM with low barrier to entry. Furthermore, the commodity thermoplastic materials used in FFF create accurate parts with robust mechanical properties, which enables broad application.

Recently, the materials available for desktop FFF have been expanding from ABS and PLA to include other materials such as Polyethylene Terephthalate Glycol (PETG) [106], thermoplastic polyurethane (TPU) [107], polyvinyl alcohol (PVA) [88], polycaprolactone (PCL) [108], and a variety of filled variants [109]–[111]. High performance materials, including ULTEM, polyether ether ketone (PEEK), and polyphenylsulfone (PPSF or PPSU) are also available; however, they are currently only printable on expensive, industrial-scale FFF systems. Such high-performance polymers have higher processing temperatures (e.g. > 300 °C) and require higher FFF nozzle temperatures due to the materials' relatively high glass transition temperature ( $T_g$ ). They also require a high temperature heated environment to reduce part curling [112], [113], and to increase overall part strength [36], [114]. Part curling occurs when printing a thermoplastic when a hot layer is deposited on and bonded to a cold layer, where it then cools and shrinks. The shrinking of the bonded layer creates internal stresses within the part that can cause the previous layers to either curl or delaminate [41], [115]. A heated environmental chamber reduces this effect by limiting the difference in the environment and extrusion temperature, and therefore the amount of shrinkage that occurs [116].

Additionally, a heated chamber also has been shown to improve the part strength. Manufacturing the part in a heated environment decreases the rate of cooling of an extruded substrate, which increases the weld time promoting chain diffusion and increased entanglement between layers to generate a stronger weld [44], [117]. For example, printing PEEK in a high temperature environment results in a stronger part, with a higher percent crystallinity [114]. PEEK printed in an ambient temperature of 200 °C demonstrated an improved of about 40 % in the tensile strength and elastic modulus compared to PEEK parts printed in room temperature. There are other techniques that also address the part strength by pre-heating the deposited strand using a laser [118], microwave [119], or heating element [120]. However, for materials that have a high thermal expansion, pre-heat treating the previous layer still creates a large thermal gradient in the part, which will result in curling. A heated environment improves both the layer bonding and reduces part curling.

#### 5.1.2 Review of existing high temperature environment machines

High temperature FFF is enabled via specialized machines that print parts within a high-temperature environment. In addition to Stratasys' Fortus line of printers, new systems have arrived recently in the market with the ability to print PEEK, Polyetherimide (PEI), Polyvinylidene fluoride (PVDF), Acetal Copolymer (POM-C), and Nylon (PA6,6, and PA6,12). These systems have increasing cost with capable printing temperatures (Figure 32).

The maximum temperature of the machine is effectively limited by the system's component with the lowest operating temperature range. These parts and components with extended operating temperature ranges increase the total cost of the printer, which effectively limits access to these high-performance polymers. Figure 32 lists existing commercially available high-temperature 3D printers and their advertised maximum steady state temperatures. From this synthesis, it is observed that the maximum temperature of the machine has a roughly logarithmic relationship with the cost of the printer.

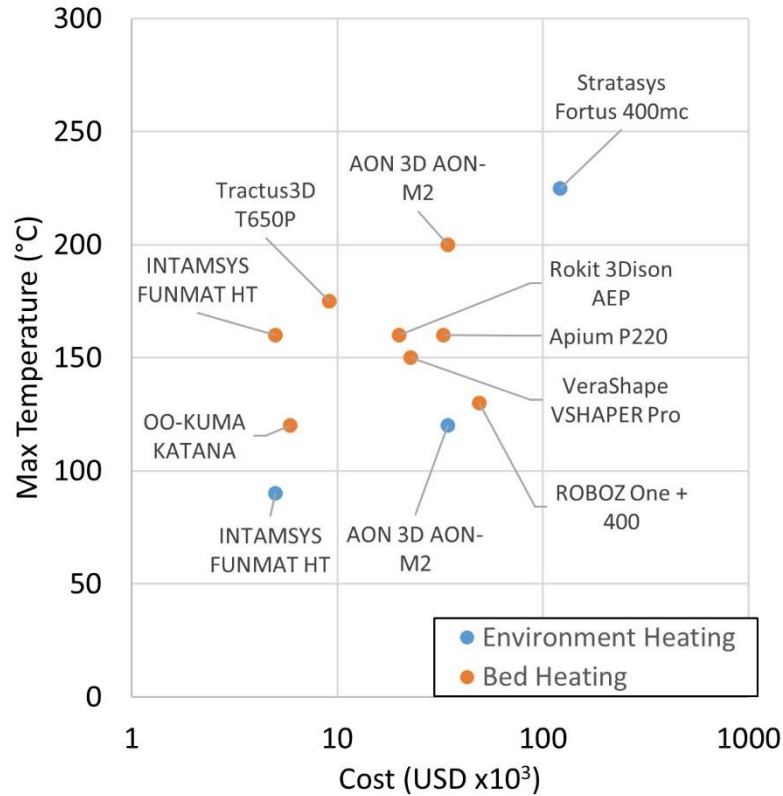


Figure 32: The advertised maximum temperature for and cost for FFF systems featuring bed and/or environment heating [121]–[130].

To avoid intellectual property conflicts [116], most of the high temperature machines rely on conduction of the heat through the bottom of the print bed to minimize curling. The bed is limited to maintaining temperatures below the  $T_g$  of the polymer to prevent deformation of a part's bottom layers. In their patent regarding the use of heated build chamber in FFF, Stratasys reports the ideal temperature being between the material's solidification temperature and its creep relaxation temperature [116]. This means printing tall parts on a heated bed (no heated environment), the top of the part is too far removed from the heat source and cannot gain all of the layer bonding benefits of the additional heating. Furthermore, complex-shaped parts may experience uneven heating/cooling throughout the part.

A heated chamber is a more stable design solution as it maintains the printing environment to a uniform, elevated temperature. The steady uniform temperature brings the entire part closer to  $T_g$ , which creates stronger bonds between part layers due to the higher bonding potential [36], as well as decreasing the residual internal stresses.

Yang's prior research on printing PEEK suggests that an ambient temperature of at least 200 °C is sufficient for printing parts with high mechanical properties [114]. Most of the available printers shown in Figure 32 are incapable of such high temperatures and the printers that can are very expensive.

### 5.1.3 Objective

Given this observed gap in FFF performance and cost, the authors aim to realize a FFF system that can print high-performance polymers at a low cost. The authors introduce a novel FFF system design that (1) exceeds current high-temperature systems to enable the capability of printing new high-performance materials and (2) can be applied to desktop-scale FFF machines. Specifically, the authors explore an inverted heated build chamber which uses natural convection to maintain a high temperature environment without exposing standard electronics to these temperatures.

Design considerations are first evaluated in Section 5.2.1, and their design tradeoffs are shown in Section 5.2.2. The core design tradeoff is maintaining a high temperature environment while keeping low cost electronics and used to inform the basis of the design solution (Section 5.3.1). The design concept was modeled using CFD to evaluate the heat transfer (Section 5.3.2) and validated (Section 5.4.2.1) by a prototype system. PPSF tensile specimens were printed to quantify the improvement in material strength; a complex part was also printed to demonstrate the ability to print different design features (Section 5.4.2.2).

## 5.2 Design Problem of a Heated Environment System

The design discussion begins with first highlighting the customer needs and the key design considerations for the system. The design considerations are then evaluated against each other and the design tradeoffs for different existing solutions are discussed.

### 5.2.1 Design Considerations/Customer Needs

#### 5.2.1.1 *Environment temperature*

The primary design requirement is to maintain steady environmental temperature of at least 200 °C. Yang et. al.'s work informs that printing PEEK requires a minimum environment temperature of 200 °C to improve the part mechanical properties [114]. However the continuous development of new materials may require environment temperatures exceeding 200 °C. In order to not limit the solution to current existing materials, the environment temperature should be maximized.

#### 5.2.1.2 *Component temperature*

When using high-temperature environments, whether it is environmentally controlled or controlled by a heated bed in an enclosure, special consideration needs to be taken for all of the exposed machine components (e.g., motors, wires (wire coating), belts, polymer mounts and brackets, etc.) that may be affected by the elevated temperatures. Parts can be affected by different failure modes when subjected to prolonged exposure to high operating temperatures. For example, typical low-cost stepper motors used in desktop-scale FFF systems (e.g., a NAME17) to drive the XYZ gantry are limited to operating in temperatures below ~100 °C for any sustained period of time, as stepper motors magnets lose their magnetism at elevated temperatures.

When designing the heated environment, the exposure of all components within it needs to be considered. The placement of each component must allow for the component to operate within its designed stable operating temperature range without sacrificing printing functionality and performance.

### 5.2.1.3 Cost

For the solution to be suitable for the authors' goal of enabling democratization of 3D printing high-performance polymers, the total cost of the machine with high temperature environment capabilities needs to be minimized. The cost of each printed part is the combination of the cost of the material, machine, labor, and its operation and maintenance divided by the number of parts printed during the machine's lifetime [2]. Thus it is advantageous to design the high temperature build environment so that both the initial price of the machine is low, as well as the cost associated with operation and maintenance.

### 5.2.2 Discussion of Design Tradeoffs

The key design tradeoff is maintaining low-cost components despite the need for them to operate in and/or near high-temperatures. Figure 33 contains three potential design solutions for the components' interaction with the heated environment. The components must be compatible with (Figure 33a), protected from (Figure 33b), or removed from (Figure 33c) the high-temperature environment for the machine to function. All of the high temperature printers from Section 5.1.2 embody one or more of these solutions across different components used. Here the authors isolate these solutions and evaluate the tradeoffs.

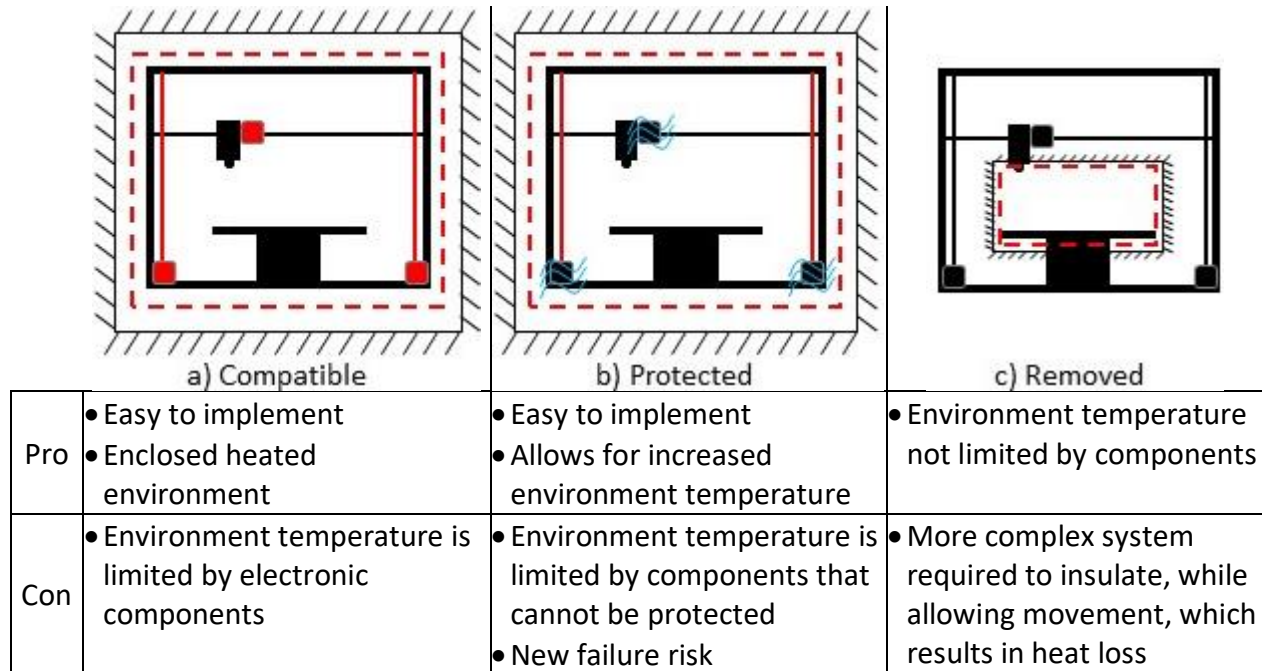


Figure 33: Three design concepts for handling the components compatibility to enable printing in high temperature environments.

#### 5.2.2.1 Compatible Components with the High Temperature Environment

In this solution using “compatible components”, only parts and electronics that are able to operate in the high-temperature environment for sustained periods of time are used. For example, a printer can be enclosed inside of an insulated chamber, such as the Afinia H800 (Afinia 3D). The Afinia uses heat from the print bed in order to heat the part and the environment. This solution is sufficient for commodity plastics such as ABS. The Afinia is not marketed for high-temperature polymers due to the low-cost plastics and electronics used in the machine that are not rated for temperatures greater than about 100 °C. Incorporating higher temperature rated electronics would allow for increased build environment temperatures; however, these components are typically

more expensive and pose new limits that may or may not be sufficient for high-temperature polymers.

#### *5.2.2.2 Protected Components from High Temperature Environment*

“Protected components” are defined by adding insulation and/or cooling to protect components and electronics from the high-temperature environment. This has the advantage of expanding the operating range of components to be able to operate at a higher environment temperatures without replacing them. A patent exists on a design for actively cooling the printer electronics [131]. AON-M2 is one commercial machine that uses liquid-cooled hot end and motion components to allow an increased environment chamber temperature [122]. A non-commercial design that uses protected components is documented by NASA, for modifying an existing 3D Printer (Lulzbot Taz 4) for printing high-temperature polymers. This modification includes adding an enclosure around the printer, active cooling for the motors, added heat lamps at the print bed, and replacing plastic parts [132]. Using heat lamps is a different way of protecting the electronics by focusing heat to the printing parts, creating inconsistent heating in the environment, thus the air around the part is hotter, where it is needed, than the air around the motors, where it is not needed.

Protecting components allows for the increase in the environment temperature past the limitation of the motors and larger electronics. However, the build environment temperature is still limited by any belts, plastic parts, wire insulation, etc. that are more difficult to protect and must be replaced with compatible components.

#### *5.2.2.3 Removed Components*

“Removed components” refers to removing all of the parts and electronics from being inside, or in contact with the high temperature needed for the environment. A patent that uses this design concept is owned and used by Stratasys for their FFF systems [113]. The motors are positioned externally to the heated chamber, using linear screw and belts to move the bed and print head. This design concept has the advantage of isolating the machine components, and allowing the heated environment to exceed any component temperature limits.

The challenge with this design is thoroughly insulating the build chamber, excluding the extruder motor, while still allowing full movement of the print head inside the build chamber. For example, the Fortus 400mc machine chamber top is insulated using a plastic accordion baffle to allow movement of the print head in the build space. The accordion insulation is insufficient to prevent heat from escaping into the top of the machine, which contains the print head components. The current designs that remove components have heat loss outside the chamber, resulting in some components being exposed to elevated temperatures.

### 5.3 Inverted Printer Design for a High-Temperature Build Environment

#### 5.3.1 Design

Removing the components from the heated environment is the only design solution that does not limit the temperature of the environment to the operating temperature of the components. This could allow for all printer components used for the motion and control of the printer to be inexpensive components that operate at room temperature. Such a solution would enable both minimizing the cost and maximizing the environment temperature. Removing the components still poses the design challenge of properly insulating the build environment for temperatures  $> 200\text{ }^{\circ}\text{C}$  to minimize the energy loss, while allowing full movement of the print head within the chamber. High-temperature insulation typically uses glass and ceramic fibers to create a brittle cloth-like texture, which breaks and crumbles with excessive movement. The print head requires full

movement within the build chamber and moves constantly while printing (at speeds more than 60 mm/s) for extended periods of time. The contradictory requirements between the print heads constant motion and the insulation breaking with movement poses a difficult design challenge.

At high temperatures, the most important wall of the build environment to insulate is the top of the build environment due to the natural, vertical flow of air as its temperature increases (and density decreases, as per Charles Law). Correspondingly, the bottom of the environment is less important to fully insulate, as it will experience less heat loss. Therefore, the authors argue that it would be advantageous to *invert the printer*, where insulation can easily be applied to the top and walls of the build chamber, and the bottom of the build chamber can remain open to allow of free movement of the print head.

A schematic of the proposed inverted high temperature system is shown in Figure 34. In the inverted configuration, the heated environment will act similar to a closed environment due to the difference in density of the cold and hot air, which will create a density barrier where the hot, less dense air will rise above the cool air. The inverted system effectively removes all printer components from the heated build environment, effectively solving the tradeoff between the cost of the component and the operating temperature discussed in Section 5.2.2. The feasibility of printing in an inverted configuration have been documented in previous research to verify the use of FFF for zero-G environments [133].

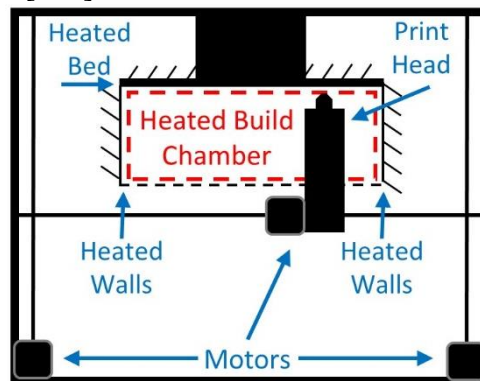


Figure 34: High environment temperature system design, where the printer is inverted to allow for an open bottom to the heated print area for the print head to be able to access without inhibiting movement.

While this inverted design enables a high-temperature heated environment; however, it does impose some limitations to the process. For example, the inverted configuration may not be compatible with a hybrid AM system [134] or in-situ embedding of non-printed parts [15], [98]. The technique or tool used in a hybrid design must also be compatible with the inverted configuration. For example, material jetting relies on gravity to dispense the material, and is therefore not compatible with the inverted design. An embedding system also has challenges with gravity with the addition that the embedded components must be compatible with the high-temperature environment for the duration of the print.

### 5.3.2 Verification via Computational Fluid Dynamics Model

To verify that a high-temperature environment could be reached and sustained with the inverted FFF concept, and that a temperature barrier would be created, the system was modeled using computational fluid dynamics (CFD). The model is used to evaluate the feasibility of the design and does not include the additional thermal mass of the part and the moving print head. A

2D steady state, pressure-based model was used, with a coupled pseudo-transient solution method in Ansys 17.0 Fluent. The chamber was modeled at 50.8 mm x 152.4 mm to match the dimensions of the physical prototype (Section 5.4). The walls were modeled as a 6.35 mm thick aluminum plate at a constant temperature of 200 °C. An open atmosphere around the opening of the chamber (304.8 mm x 304.8 mm) was defined to simulate the temperature where the system electronic components reside. Figure 35a shows the simulation setup. Fluent does not have an open boundary condition, therefore an intake-fan was used to model the open boundary, with turbulence intensity of 5% and a turbulence viscosity ratio of 10. The sensitivity of the turbulence and other fluent boundary conditions were modeled to verify the assumed boundary condition did not significantly affect the temperature gradient or velocity profile within the chamber. The density, specific heat capacity, thermal conductivity, and viscosity of air were manually input as a piece-wise linear function of temperature. Sensitivity analysis was performed on the mesh and boundary conditions to ensure the accuracy of the model.

The resulting thermal map and velocity profile are shown in Figure 35b and 4c. As hypothesized, trapped hot air rises to the top of the chamber which forms a temperature gradient at the boundary of the chamber and the open atmosphere. Heat generating from both the walls and the print bed create a vertical temperature profile with a horizontal temperature boundary and even heating throughout the environment. Air heated by the walls causes the air to flow upward along the wall, through natural convection. The vertical flow on the walls of the chamber then pushes the air on the top of the chamber to then flow inward and down creating a circular flow. Warm air recirculates as it nears the temperature boundary due to the lower density warm air remaining above the cool air to effectively enclose the warm air in the chamber. The temperature was maintained with 1% error for 4.4 mm z-height (>198 °C), 5% error for 19.2 mm z-height (>190 °C), and 10% error for 29.8 mm z-height (>180 °C), without including the heat provided by the print head or conduction through the part. This model shows how a consistent print chamber temperature of 200 °C can be created using an inverted chamber with heated walls and print bed.

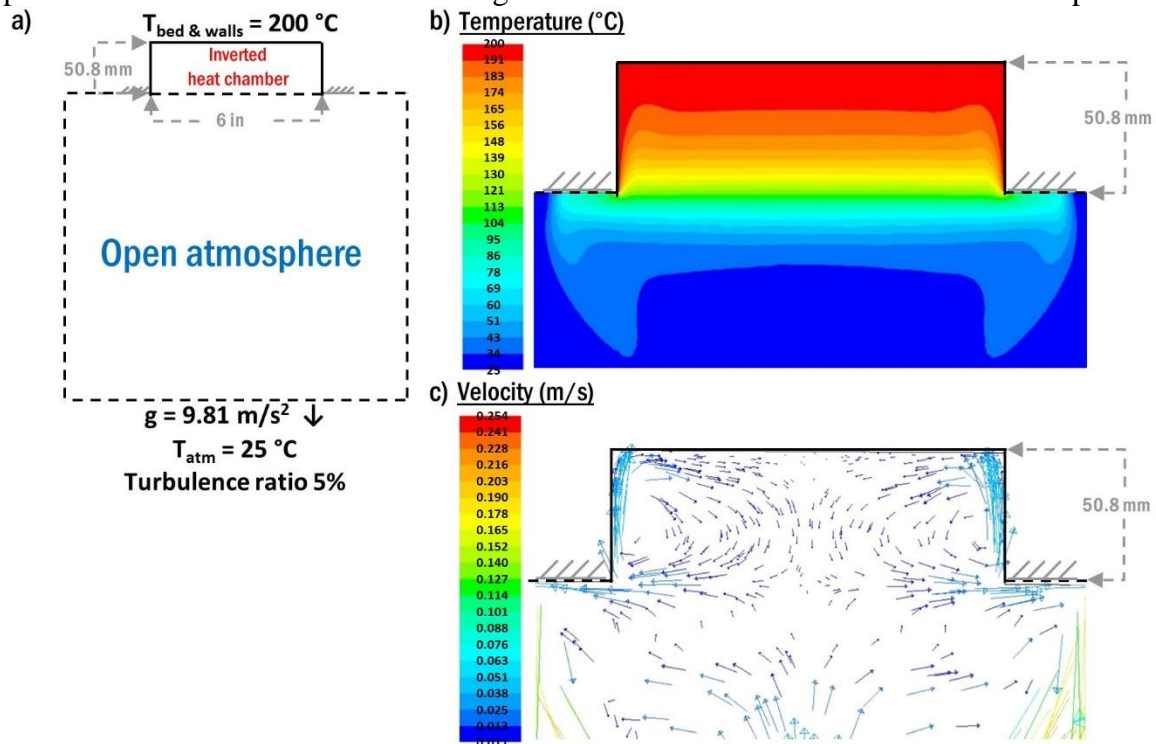


Figure 35: The simulation output for the a) the experimental set up, b) temperature profile, and c) the velocity profile for the inverted heat chamber.

To verify that the overall system design is generalizable for larger dimensions, the simulation was run with differently sized chambers (Figure 36). This allows for a comparison of the 50.8 mm x 152.4 mm chamber (Figure 36a) to a (2) taller (304.8 mm x 152.4 mm) (Figure 36b), (3) wider (50.8 mm x 304.8 mm) (Figure 36c), and (4) taller and wider (304.8 mm x 304.8 mm) (Figure 36d) chamber. The results of these simulations are synthesized in Figure 36 and demonstrates that increasing the chamber depth results in the temperature gradient remaining at the boundary of the heated chamber. The chamber width does not significantly affect the temperature gradient boundary. Increasing the size of the chamber becomes physically challenging to build and produce an isothermal wall boundary condition; however, building a smaller isothermal wall for desktop scale systems is trivial. The thermal gradient remains consistently approximately 40 mm into the print chamber and 30 mm outside the print chamber boundary. The deeper chambers were able to maintain temperature for a larger volume, where the 304.8 mm x 152.4 mm chamber maintained 1% error for 240 mm z-height ( $>198\text{ }^{\circ}\text{C}$ ), and 5% error for 270 mm z-height ( $>190\text{ }^{\circ}\text{C}$ ). The 304.8 mm x 304.8 mm chamber maintained 1% error for 207 mm z-height, and 5% error for 255 mm z-height.

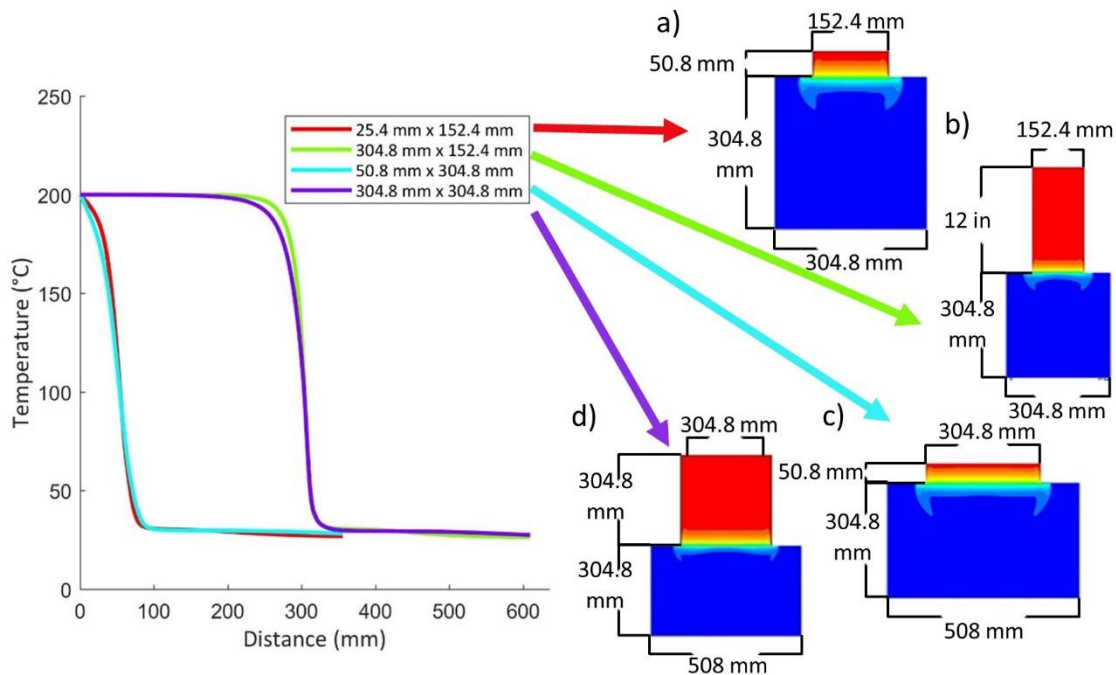


Figure 36: The temperature profile of different sized heat chamber using a 2D Fluent model.

#### 5.4 Experimental Validation

To validate the design concept, the authors created a physical prototype of the inverted printer. This section describes experimental validation of the thermal model and evaluation of printed polyphenylsulfone (PPSF) parts. It was designed to match the temperature profiles of the simulation. The temperature of the chamber walls is controlled by two PID controllers (one mounted on the inverted bed and one the cylindrical wall) to control and maintain an isothermal boundary of  $200\text{ }^{\circ}\text{C}$ . After the temperatures stabilized, temperature measurements were taken with a K-type thermocouple at different distances from the bed. Measurements were taken at 25.4 mm

increments from the print bed. All measurements were recorded as the average temperature over one minute. Following this validation, PPSF parts were then printed in the inverted build chamber to demonstrate the potential advantage of the system.

#### 5.4.1 Method

##### 5.4.1.1 Materials

The prototype for the 50.8 mm x 152.4 mm heat chamber consisted of an aluminum shell surrounded by heating elements and insulation. The total cost of the materials for the high temperature upgrade for an existing delta-style printer was less than \$300.

Off the shelf PPSF-PPSU (1.75 mm diameter) filament from Stratasys was used for printing trials. This material has a reported glass transition temperature of 230 °C and heat deflection temperature of 189 °C [135]. Stratasys operating manual states a maximum extrusion temperature of 415 °C and a maximum oven temperature of 225 °C for printing PPSF in the Fortus system [136].

##### 5.4.1.2 Printer Design

The printer design was prototyped and tested using a custom delta robot 3D printer that features inverted control arms, as seen in Figure 37. The system is controlled with an Arduino ATmega2560 running a custom version of Marlin firmware. The heated build chamber is located on the top of the printer, and features thick insulation (~25.4 mm alumina silica fiber insulation sheet and fiberglass fabric strips with plain backing from McMaster) and heaters on both the bed (Strip Heater without Temperature Control, 120V AC, 120W from McMaster) and walls of the chamber (Extreme-Temperature Heat Cable, 120V AC, 468W). An E3D V-6 print head was used with the PT100 thermocouple and a custom direct-drive extruder.

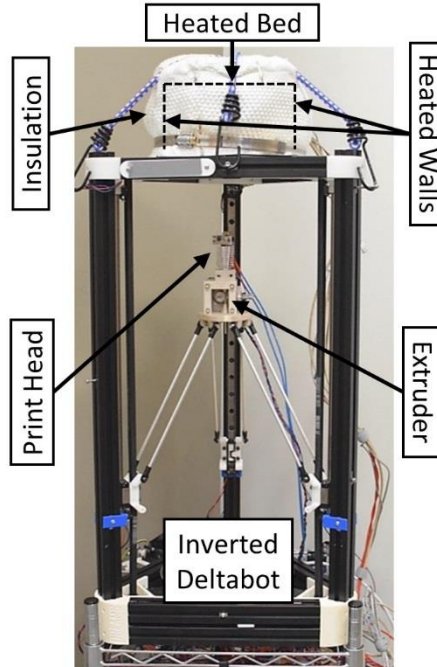


Figure 37: Functional prototype of a custom delta printer modified with the inverted heated build chamber.

### 5.4.1.3 Tensile test

To compare the effect of printing PPSF in the inverted heated chamber, tensile specimens were printed at both an elevated temperature (200 °C) and room temperature (25-50 °C). The control “room temperature” printing trials had some temperature variation due to the print head heating the insulated print area. All other process parameters were kept constant between the builds to determine the effectiveness of the heated chamber independent of inversion and printing parameters. The infill was set to 95% density with one perimeter and a rectilinear infill at +45°/-45° at 15 mm/s and a 0.2 mm layer height. Extrusion was done using a 0.4 mm nozzle at 350 °C. The print parameters were chosen for functionality; there remains the opportunity to further optimize parameters for part quality in future work. Parts were printed onto a PEI sheet that was secured to the inverted printer bed using Kapton tape. Printed parts were immediately removed from the printer following completion and set aside until the part cooled, when they were removed from the PEI sheet.

ASTM D638 Type V dogbones were printed in the XY plane and pulled on an Instron 5984 with a 10 kN load cell at 5 mm/min as per ASTM D638 [137]. A minimum of 4 dogbones were tested for each condition. The strain was calculated based on the distance of the grips. The elastic modulus was taken in the linear region where the linear fit had an  $R^2$  value of 0.99.

## 5.4.2 Results

### 5.4.2.1 Experimental Validation of Thermal Model

Figure 38 shows the inverted system’s temperature profile from both the thermal model (lines) and the experimentation (markers) using the inverted system. There is a large drop in temperature around 50.8 mm from the print bed, corresponding to the height of the chamber wall. The average temperature was used for the experiment and was within 8 °C to the pseudo transient model for all points except the points at the boundary of the chamber (50.8 mm), where there was an average of 19 °C discrepancy. The large variation at the boundary is expected due to the high temperature gradient at the boundary, which greatly affects any inaccuracy in the experimental distance measurement, and the assumptions used to model the atmosphere.

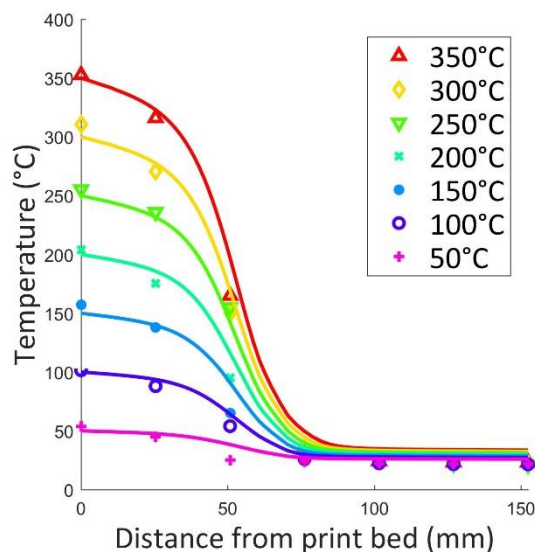


Figure 38: Experimental and modeled temperatures from the center of the bed outward where the chamber bed and walls were set to 50-350 °C, in the inverted heat chamber. The markers represent the measured temperatures, while the line represents the temperature values from the simulation.

The inverted build chamber was successfully heated to 400 °C measured at the heated bed. The authors expect that the temperature could be increased further even in this prototype build; however, 400 °C is greater than the melting temperature of most polymers and is likely sufficient for the build environment.

To validate the design decision to invert the print chamber, the results are compared to a traditional (non-inverted) chamber. An identical CFD simulation (Section 5.3) was performed with gravity inverted. The experimental data was collected with the chamber opening facing upwards. Figure 39 presents a plot of the temperature profile for the non-inverted system. Heat is lost quickly using an open top heat chamber. The environmental temperature of the traditional system experiences an exponential decay at increasing distances from the print bed. Although the thermocouple used for the controller reached the set temperature, the temperature on the top of the bed (where the part is printed) did not reach that temperature due to the loss in heat. The inverted heat chamber shows an asymptotic curve up to the set temperature, while the traditional design shows exponential decay to the room temperature. The dramatic loss in heat would be minimized if heated walls were not used, allowing heat to travel up through the center of the bed. However, at high temperatures, a printer with a heated bed and no heated walls still results in high energy loss and inconsistent heating.

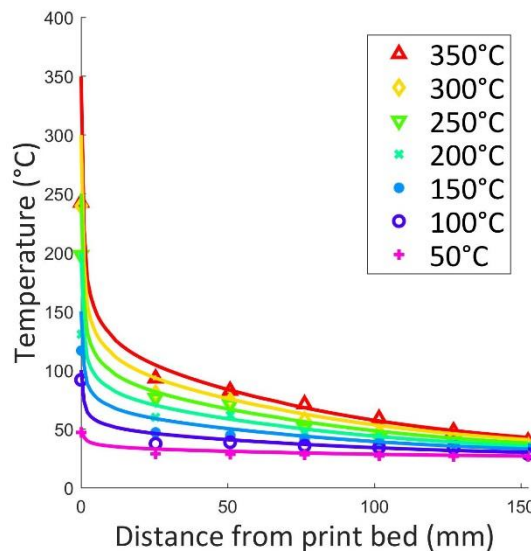


Figure 39: The measured temperatures at different displacements from the bed at temperature controller set temperatures are between 50-350°C, with a non-inverted heat chamber. The markers represent the experimental data, while the line represents the simulated data.

#### 5.4.2.2 Design Validation via PPSF Printing

PPSF Parts were printed on the inverted heated system to demonstrate the capability of high-temperature printing and to explore its impact on the resultant mechanical properties due to the heated environment. To explore the impact of the inverted heated build chamber, similar PPSF prints were completed on the same printer but without the heated chamber (i.e., parts were

completed near room temperature). A sample of a printed tensile bars with and without the inverted heated build chamber can be seen in Figure 40.

The tensile bars printed in the 200 °C chamber did not curl during printing. The room temperature environment tensile specimens curled as much as 2.34 mm the Z-direction, affecting the quality of the print, as well as the strength. The curling was so significant that a tensile bar (not used for tensile testing) fell off of the bed during the print, and the z-offset had to be adjusted to push the print head into the PEI sheet on the bed rather than being correctly calibrated.

The 200 °C environment temperature of the heated build environment prevents the material from shrinking during the print. The chamber temperature is below the glass transition temperature (230 °C) [135], so that the material is able to retain its shape. The authors believe the slight curvature in the ZY plane of the 200 °C specimen was caused during the part removal process from the PEI sheet or from a not optimized environment temperature.

Using PPSF's coefficient of thermal expansion provided by Stratasys [135], the room temperature tensile bars are calculated to shrink up to 0.6 mm more each layer in length (total 1.1 mm) than the high temperature tensile bars (0.5 mm) while cooling from the extrusion temperature to the environment temperature during printing. The discrete shrinkage of the bonded layers causes the residual stresses in the part to accumulate and cause the part to delaminate or curl. The material shrinks less while printing in the high-temperature environment, allowing the majority of the shrinking to occur after the part is printed and removed from the bed, where the part shrinks uniformly rather than discretely by layer.

Increasing the weld time between layers is critical to fabricating stronger bonds between roads and layer. Increasing the weld time increases the polymer chain diffusion across the interface and creates a stronger polymer weld [138]. Increasing the environment temperature decreases the rate of cooling, which increases the weld time. In addition, using a heated environment can allow for annealing of the part further increasing the part strength [116]. Heat treating a part after printing can increase the part strength, but requires additional processing time [114]. Using a high temperature heated environment allows for slower cooling during the print resulting in additional chain entanglement between the road and layer interfaces which increases the layer bonding and the part strength, without a post processing step.

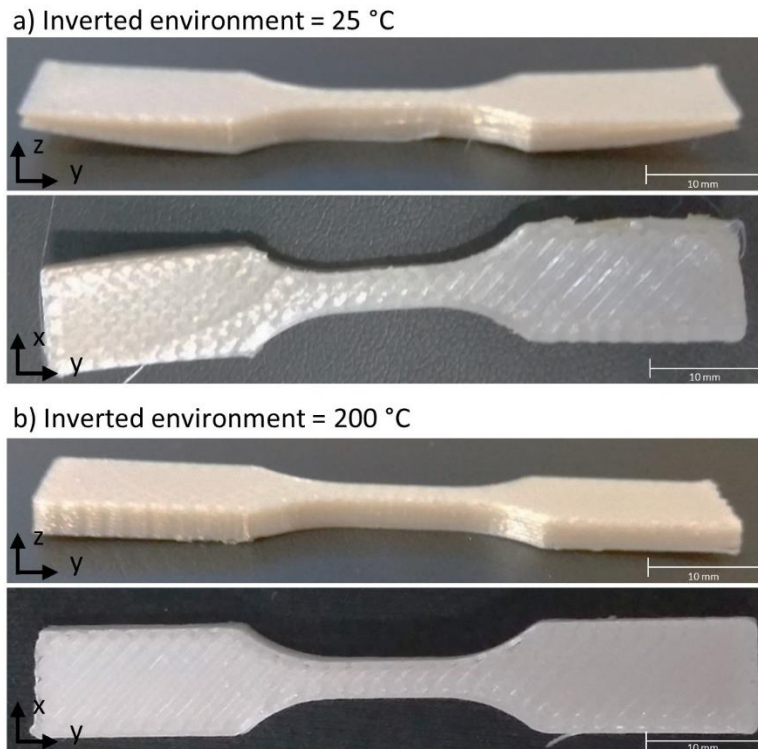


Figure 40: Printed tensile bars using the inverted printer printed at 25 °C and 200 °C. The tensile bars are 63.5 mm in length, 9.53 mm in width, and 3.17 mm in height.

Figure 41 shows the compiled tensile data, where the elastic modulus between the two printing temperatures is within error and the ultimate tensile strength is 48% higher for the higher environment temperature parts. The ultimate tensile strength for the PPSF specimens printed in the inverted high temperature environment was measured to be  $62.62 \pm 5.89$  MPa, which is comparable to the reported strength (55 MPa) specified on the Stratasys PPSF data sheet for printing on a Fortus system [135]. The elastic modulus is not comparable to the Stratasys reported data, as the experimental procedure in this work measured effective strain (i.e., distance between the grips) and not true strain.

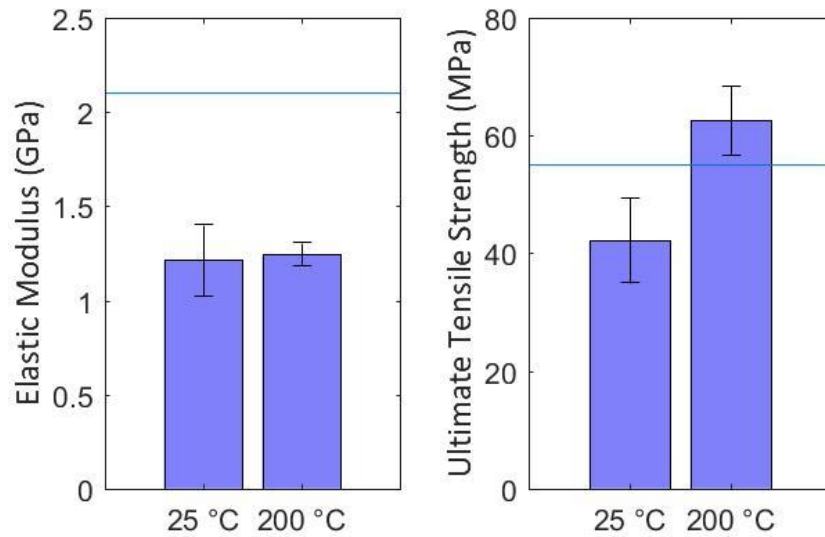


Figure 41: Tensile properties of tensile bars printed on inverted FFF system at environment temperatures of 25 °C (n=4) and 200 °C at 15 mm/s with a 200  $\mu$ m layer height and 95% rectilinear +45/-45 infill (n=5). The horizontal line indicates reported StratasyS strength [135].

In order to qualitatively assess print quality, and to demonstrate the ability to print complex, solid geometries, the authors printed a PPSF 3D Benchy part in the high temperature environment (Figure 42). 3D Benchy has been selected by the crowdsourcing community as a standard part for evaluating FFF printers' ability to print features including vertical and horizontal cylindrical holes, curved and flat overhangs, and high resolution details [139]. The part was printed at 15 mm/s using solid infill. All of the features were successfully printed with the inverted high temperature system, with the exception of the tiny surface detail (the 100  $\mu$ m extrusion “#3DBenchy” nameplate), which is a detail that is difficult for most FFF systems. The authors attempted to print the same design in the room temperature environment, but it proved to be impossible as it failed early in the build by curling and falling off of the inverted bed during the first few layers. This part demonstrates that the high temperature design enables the printing of a complex structure.



Figure 42: A standard part (3D Benchy) was printed to demonstrate the ability to print more complex parts in the inverted high temperature system.

## 5.5 Summary

Printing high-performance thermoplastics via FFF has proven challenging as the required high-temperature environments require expensive electronic components that have high operating temperatures. As such, currently commercially available high-temperature FFF systems cost > \$30,000 and offer operating environments of less than 200 °C. In order to democratize the ability to 3D print high performance polymers by minimizing the cost of the FFF system, it is therefore critical to separate the electrical components from the high environment temperature. In this work, the authors have presented a novel approach for addressing this design trade-off by inverting the printer and printing inside of a heated chamber. The inverted heated chamber traps heat due to the difference in density between hot and cold air, while also allowing for full free movement of the print head. This design solution effectively separates the printer components from the high-temperature environment.

Both a computational fluid dynamics simulation and experimental measurements on a prototype systems demonstrated that an inverted chamber, with heated bed and walls, could be maintained at 200 °C for a 29.8 mm height (with 5% error) from the build plate in a 50.8 mm tall chamber. Tensile testing of PPSF specimens printed at 200 °C demonstrated a 48 % increase in the ultimate tensile strength compared to specimens printed at room temperature. The specimens printed in the ~\$1,000 inverted build chamber also demonstrated equivalent tensile properties to specimens printed on commercially available high-temperature FFF systems that retail for >\$200,000. Complex structures with fine features and overhangs were also successfully printed with the inverted setup. This system can reach higher environment temperatures compared to machines in the current market and can be used to democratize manufacturing of high-performance polymers.

There is future work in creating a larger chamber to print larger parts and limit the thermal gradient. Preliminary simulations indicate that the thermal gradient will remain at the boundary and a more stable environment temperature can be reached within a larger chamber. In addition, the thermal process simulation could be expanded to a three-dimensional model (instead of the presented 2D model) and include the effects of a moving heated print head to observe the impacts

of air circulation distributed heat input (instead of the presented model's static extruder). While experimental results validated the current simulation, and the overall advantages of an inverted process chamber, such an updated model would improve the model's overall accuracy. Finally, the authors aim to explore the effects of gravity on the printed large parts in the inverted configuration.

## 6. The effect of Fused Filament Fabrication Thermal Processing Conditions on the mechanical strength and dimensional accuracy on Ultem 1010

### 6.1 Introduction

Polyetherimide (PEI) is an amorphous polymer that provides high-strength and chemical resistance in high-temperature environments. Fused filament fabrication (FFF), a material extrusion additive manufacturing (AM) process in which heated thermoplastic materials are selectively deposited and cooled to form three-dimensional shapes, has proven suitable for processing PEI resins, with several commercially available solutions available on the market in the ULTEM® series [140]. ULTEM® 9085 has been rigorously characterized for the approval of qualified use in aerospace applications, specifically using the Stratasys Fortus machine [13]. ULTEM® 1010 is transparent and is used in automotive (under the hood), outdoor construction, electrical devices, and energy storage applications due to its relatively high glass-transition temperature, chemical resistance, and high tensile strength [14]. ULTEM® 1010 has been printed with carbon nanotube yarn for embedded functionality [141] as well as incorporated with various fillers [142]. However, the FFF of ULTEM® 1010 has been less researched overall [143]. The processing of polymers that have high transition temperatures, such as ULTEM® 1010, are more difficult to process using FFF because they require i) a higher processing temperature to enable material flow [117] and ii) a high build environment temperature to ensure inter/intralayer bonding of the extruded roads and to reduce part warping from solidification-induced residual stresses [36], [144].

#### 6.1.1 Thermal Processing Effects of FFF parts

The temperature of the extrusion nozzle must be sufficiently high to allow for consistent extrusion of the material, without causing polymer degradation. In a study of FFF of polypropylene, Watanabe et al. discovered that nozzle temperature does not significantly affect a part's tensile stress, nominal strain, and modulus of elasticity [145] or part warping [146]. Montero et. al. similarly found that nozzle temperature for ABS did not affect tensile strength [147]; however, Aliheidari et. al. showed it affects the fracture behavior [148]. However, due to the temperature-dependence of polymer viscosity, a sufficiently heated nozzle is required for the polymer to flow [41]. If the nozzle isn't heated sufficiently, and the motor cannot produce the required force to extrude the material, the material will under-extrude which causes porosity in the printed part. For high-temperature polymers, the temperature of the nozzle is higher than typical FFF materials in order to sufficiently decrease the viscosity for extrusion [149].

In order to improve layer bonding and to prevent curling deformation, FFF systems capable of maintaining high-temperature build chambers are required to successfully process PEI [150]. Decreasing the difference in temperature between the nozzle and the build environment results in a slower cooling rate, which allows for the part to remain above the material's glass transition temperature ( $T_g$ ) for longer (though not indefinite). The heat introduced by the adjacent road also reheats the previous road and contributes to this [151]. The time that two adjacent printed road remain above  $T_g$  is critical as it increases the reptation and chain entanglement between individually printed roads, producing a stronger bond and improving the overall part strength. The "bonding potential" is a variable that was developed based on the time the material remains above a critical temperature (such as  $T_g$ ) as an indicator for strength [36]. For amorphous polymers such as PEI, the build environment temperature cannot remain above the material's  $T_g$  temperature or

heat deflection temperature for an extended period, to increase the bonding potential, as it can cause part slumping and deformation [116]. Therefore, keeping the build environment below  $T_g$  is necessary to prevent deformation; however, this limits the extrudate bonding potential due to rapid cooling (especially for high-temperature differentials found when printing PEI), which can result in weak parts and exaggerated anisotropy [36], [44]

Pre-deposition heating using a laser is another method shown to greatly improve ULTEM® 1010's tensile strength [118]; however, selective laser heating of larger parts is not expected to decrease shrinkage and part curling. Decreasing the difference between the extrusion and the environment temperatures effectively limits the amount of material shrinkage that occurs during printing. The discrete shrinking of the layers that occurs during printing, caused by the thermal gradients between layers, creates residual stresses within the part that causes delamination and/or part curling [41]. By limiting the amount of shrinking that occurs during the print, and allowing the majority of the part to shrink simultaneously, the part is less likely to deform. As such, the first goal of this work is to explore the effects of the FFF thermal process parameters (extrusion nozzle and build environment temperatures) on the mechanical properties and dimensional accuracy of ULTEM® 1010.

#### 6.1.2 Thermal Post-Processing Effects on FFF Parts

While tuning the processing conditions can improve the mechanical strength, thermal post-processing the parts can be done to further strengthen the printed part. In order to increase the bonding between layers, thus increasing the overall part strength, the printed parts must be post-processed above the glass transition temperature. This is done to provide sufficient energy to enhance molecular movement and increase polymer chain entanglement between layers. Post-processing of more common, lower temperature FFF materials (ABS, PET, and PLA) has resulted in increased mechanical properties, including tensile strength [152], fracture toughness [153], and flexural strength [154]. Hart et. al.'s study of fracture toughness tested post-process annealing ABS samples above their  $T_g$  for a prolonged period of time (2-168 hrs.). Due to the parts' inability to maintain their shape while being held above  $T_g$ , an aluminum fixture to support the shape of the printed rectangular prisms was created for post-processing [153]. Post-process annealing above  $T_g$  increased the fracture toughness up to 2720% (held at 135 °C for 72 hrs.) when compared with no annealing. The stable crack propagation can be achieved by either increasing the temperature or increasing the time the part remains at temperature, due to the time-temperature superposition principle. *The second goal of this paper is to explore techniques for holding ULTEM® 1010 above  $T_g$  for prolonged periods of time and to study the effects of post-processing on both strength and dimensional accuracy.*

The authors also hypothesize that a part with fewer pores and better interfaces will result in a clearer part when using a transparent material such as ULTEM® 1010. *The third goal of this paper is to determine if the absorbance of light through a printed ULTEM® 1010 part correlates to its mechanical strength.*

## 6.2 Methods

The thermal properties and rheology of the as-received ULTEM® 1010 filament are first characterized to gain an understanding of the melting behavior of the material and to guide the selection of process parameters. The nozzle temperature, environment temperature, and post-processing conditions are tested independently to determine the effects of each processing parameter on the tensile properties and dimensional accuracy of the printed parts. Table 5 shows the temperatures used for each experiment. Finally, the part's absorbance to light is characterized

to test the hypothesis that there is a relationship between a printed part’s strength and its optical clarity.

Table 5: The experimental processing conditions were varied to test the effects of thermal processing on part properties.

	<b>Experimental Temperature Studies</b>		
	<i>Nozzle</i>	<i>Environment</i>	<i>Post-Processing</i>
Nozzle Temperature	330, 340, 350, 360, 370 °C	360 °C	360 °C
Environment Temperature	180 °C	50, 100, 150, 175, 200, 215, 225 °C	200 °C
Post-Processing	none	none	260 °C for 0, 6, 12, and 24 hrs.

### 6.2.1 Materials and Thermal Characterization

ULTEM® 1010 filament was purchased from Argyle Materials. The material was dried at 80 °C overnight and stored in a dry box with desiccant. Short sections of approximately 1 m were cut and were used for printing to prevent the material from hydrating during testing.

The material’s thermal-mechanical properties were evaluated using thermogravimetric analysis (TGA), differential scanning calorimetry (DSC), and oscillatory rheology. TA instruments TGA 500 was used to evaluate thermal degradation by running a test from 30 °C to 800 °C at a rate of 10 °C/min. DSC was run on a TA Instruments DSC Q2000 from 30 °C to 230 °C on a heat-cool cycle at 10 °C/min. In order to better mimic the thermal processing conditions of the filament in the print nozzle, the first heat was used to determine the glass transition temperature. Oscillatory rheology was performed using a TA Instruments Discovery HR-1 with an 8 mm parallel plate. Complex viscosity was measured from 0.1 to 100 rad/sec at 1% strain at temperatures ranging from 330 °C to 370 °C.

### 6.2.2 Processing

#### 6.2.2.1 Fused Filament Fabrication

The printing was performed using an inverted delta-style custom FFF printer (Figure 43). This printer offers a high-temperature build environment and open architecture process parameters (via open-source printer firmware (Marlin 2011) and toolpath generation (Slic3r version 1.3.0) to enable high-temperature FFF research. Additional information on the printer design and its validation can be found in previously published work [150]. The printer uses an E3D print head (E3D V6) with a thermocouple (E3D PT100) to maintain an extrusion nozzle temperature of < 400 °C and an environment temperature of up to ~400 °C. The parts are printed onto a PEI sheet that was adhered (via Kapton tape) to a removable aluminum plate at the top of the inverted heat chamber. Finished parts were immediately removed from the heated chamber and pulled off of the PEI sheet while still hot/warm, which allowed for easier removal. Aside from the nozzle and build

environment temperatures, printing conditions were kept constant across all experiments (Table 6).

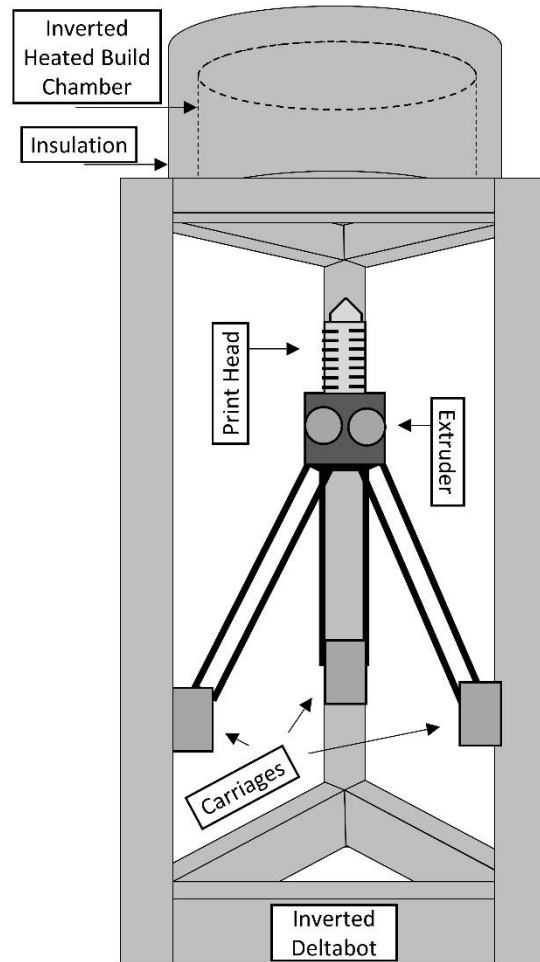


Figure 43: A schematic of the delta-style inverted printer with a heated build chamber used for printing (adapted from [150]).

Table 6: Controlled printing process parameters used to test the effects of thermal processing conditions.

<b>Controlled FFF Process Parameters</b>	
Nozzle Diameter	0.4 mm
Layer Height	0.2 mm
Infill percent	100%
Infill pattern	Rectilinear (45°/45°)
Print speed	15 mm/sec

#### 6.2.2.2 Nozzle Temperature

To explore the effect of nozzle temperature, four geometries were printed in a 180 °C build environment at nozzle temperatures ranging from 330-370 °C in 10 °C increments. The nozzle temperature range was chosen because 330 °C was the lowest temperature that created a constant extrudate flow (without the motor audibly skipping) and the filament was found to heat and deform before entering the heater block when the nozzle was set to 380 °C.

#### 6.2.2.3 Environment Temperature

The build environment temperatures studied ranged from just above room temperature to just above the  $T_g$  of ULTEM® 1010 (217 °C). Specifically, temperatures of 50 °C, 100 °C, 150 °C, 175 °C, 200 °C, 215 °C, and 225 °C were used with a constant nozzle temperature of 360 °C. Higher environment temperatures were not used because using an environment above  $T_g$  can cause the filament to deform before the heater block of the print head, “clogging” the print head (similarly to when the nozzle temperatures exceeded 370 °C, Section 6.2.2.2), and the inverted part to stretch due to gravity during printing.

#### 6.2.2.4 Post-Processing

For the polymer chains to have sufficient energy to increase entanglement between the printed roads and layers the post-processing temperature is required to be above  $T_g$ . However, this also permits the material to deform and lose its desired shape. A technique was developed to embed the parts in powder, where the printed parts can be heated above  $T_g$  while the powder supports the shape of the printed parts. This technique can only be applied to solid or near solid parts, as parts with a sparse infill may cave in. Table salt (Kroger) was selected for the material based on i) the ability to be obtained in powdered form, ii) its melting temperature is higher than the  $T_g$  of the polymer, and iii) the water solubility of the powder enables its facile removal from the part following post-processing.

The printed parts used for SEM and characterizing the tensile strength, dimensional accuracy, and clarity (described in Section 6.2.3) and a complex part, to evaluate the effectiveness of this technique on printed complex parts, were packed carefully into a stainless steel cylinder (10 cm diameter x 10 cm tall) with salt used to contain and separate the parts. The temperature was recorded using a sensor (FluxTeq PHFS 0.5” square) that was protected by two small aluminum sheets (to protect the sensor from bending) and was placed below the complex part toward the center of the layer. The procedure for salt powder packing is as follows.

- 1) Pulverize salt: Salt was pulverized into smaller particles using a blender (NutriBullet) for ~30 s to enable better packing.
- 2) Layer Salt: Salt is loosely layered into the container (the top and bottom had ~10-20 mm and between parts had ~5-10 mm loose powder).
- 3) Tap: Container is lightly tapped by hand on a solid surface repeatedly for approx. 15 sec for the powder to pack and settle to a flat layer.
- 4) Layer Parts: A layer of parts was added on the top surface of the flat powder. Figure 44 shows a visual representation of the layering of the printed parts in sets.
- 5) Repeat: Steps 2-4 were repeated, adding 4 sets of parts.
- 6) Cover: The parts were then covered with a final thicker layer of powder and tapped on a solid surface.
- 7) Compress: Lastly, the salt and parts were compressed by hand by pushing a smaller flat cylinder into the container until the salt ceased compressing.

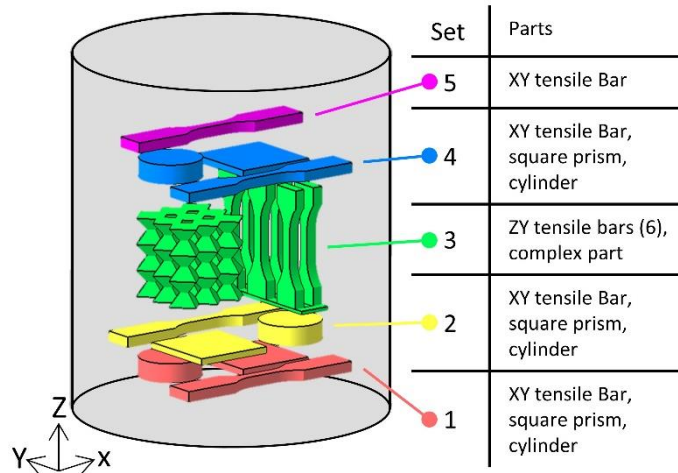


Figure 44: A scaled visualization of the parts packed into the cylindrical container. Set 3 also contained a temperature sensor placed below the complex part and toward the center of the cylinder.

Parts for post-processing were printed using a nozzle temperature of 360 °C and an environment temperature of 200 °C. The post-processing oven temperature of 260 °C was chosen to be a similar ratio between the  $T_g$  (217 °C) and the printing nozzle temperature used in Hart's study using ABS (135 °C) [153]. Using a lower temperature for a longer time, opposed to a higher temperature for a short time [155], allows for the entire packed system to reach the desired temperature, before parts closer to the surface start degrading (due to reaching the desired temperature first, and remaining hot for longer while the internal parts heat). The thermal cycle used for post-processing is depicted in Figure 45 with a two-hour ramp up, a hold, and cooling. The hold time was set to 6, 12, 18, and 24 hrs. The  $T_g$  (217 °C) was reached approximately one hour into heating and the temperature was >95% of the set temperature (260 °C) at 2 hrs. Once removed from the oven, the container cooled from 260 °C to  $T_g$  in less than 15 minutes.

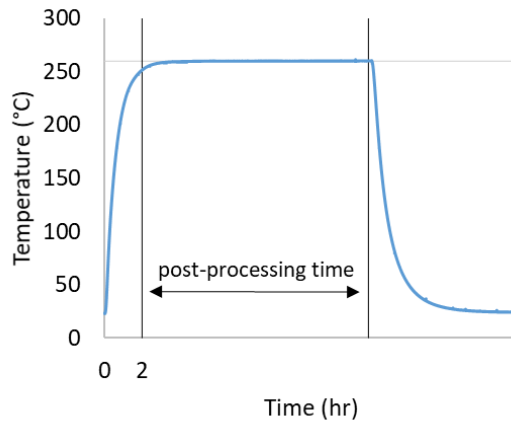


Figure 45: The temperature ramp and cooling cycle of the post-processing technique as measured by an embedded thermocouple. The post-processing time was set to 6, 12, 18, and 24 hrs.

### 6.2.3 Characterization

#### 6.2.3.1 Scanning Electron Microscopy (SEM)

Printed squares (25.4 mm side length) that had 10 layers of 0.2 mm thickness were printed in sets of three for each thermal condition. The parts were freeze fractured by dipping the parts into liquid nitrogen for a minimum of 20 seconds and snapping them in half along the top layers' printed road direction (diagonally across the square). The pieces were then sputter-coated in Au/Pd using a Cressington 208Hr for 15 seconds and SEM images were taken of the fracture surface on a LEO (Zeiss) 1550.

#### 6.2.3.2 Tensile Strength

The tensile strength was tested for tensile bars printed horizontally on the build plate (oriented in the XY plane) and printed vertically (along the ZY plane). The horizontal tensile specimens are standard ASTM D638 Type V tensile bars and were printed in pairs (Figure 46A), with a sample size of four. Due to the height restriction of the heated environment for the printer [150], the vertical tensile bars are the same standard ASTM D638 Type V tensile bars with 12.7 mm removed from each end of the gripping region. These specimens were printed in groups of six in order to allow for cooling time between each layer with the smaller cross-sections. A rectangular base was added to the six specimens for stability during printing and they were cut away for testing (Figure 46B).

The specimens were broken on a universal testing machine (Instron 5984) using a 10 kN load cell and pulled at 5 mm/min. The specimens were evaluated for the elastic modulus and yield. The stress was calculated using a constant cross-sectional area. The modulus was calculated by calculating a linear fit between 10% and 80% of the ultimate tensile strength, decreasing the region by 2% until the  $R^2$  value was greater than 0.99. The yield point was evaluated to be at the end of the linear fit used to calculate the modulus.

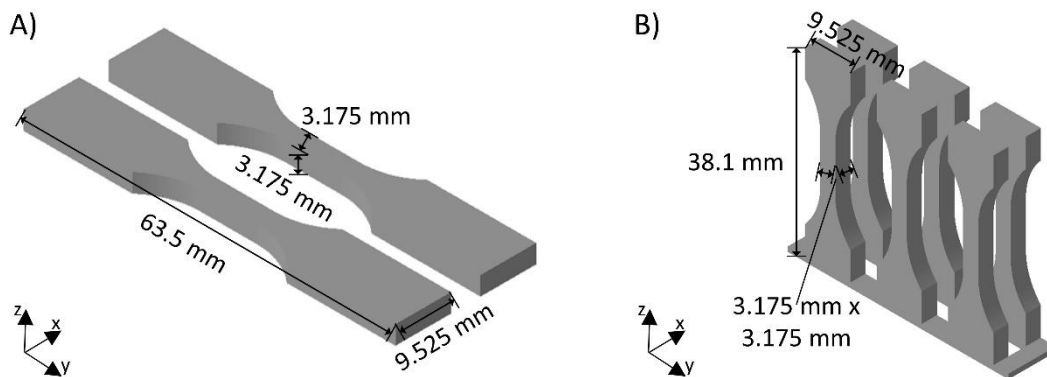


Figure 46: Visualization of the printed tensile bars and how they were printed on the printer bed where a) represents the horizontal XY tensile specimens and b) represents the vertical YZ plane specimens.

#### 6.2.3.3 Dimensional Accuracy

There is a difference in how the part accuracy was measured for the experiments pertaining to the nozzle temperature, environment temperature, and post-processing time based on the expected mode of failure related to the part accuracy. The nozzle temperature affects the flow rate of the material extruded during printing, thus failure occurs when there is restricted material flow due to polymer viscosity being too large at low processing temperatures, and/or clogging of the nozzle.

As such, part accuracy for the varying nozzle temperatures is quantified by measuring the mass of the printed part and comparing it to the theoretical as-designed mass. The mass was measured using a U.S Solid Laboratory Equipment Digital Analytical Balance (Model USS-DBS8).

When altering environment temperature, the dominant failure modes are part deformation and curling due to thermally-induced shrinkage and residual stresses during cooling. As such, part accuracy for these experiments was measured by assessing part curling for the different build environment temperatures. This was done by placing the printed XY tensile specimens on a flat surface and taking measurements from digital photos of the vertical distance between the part ends and the surface images.

As the proposed post-process subjects parts to a temperature above the  $T_g$  for a sustained period of time, it has the most potential to cause dimensional variation. The dimensional accuracy of parts subjected to this post-process is measured by comparing the dimensions of the part before and after post-processing using digital calipers (PITTSBURGH 47257 6" digital calipers). These dimensions (shown in Figure 47) are taken for the XY tensile bars, the Z tensile bars, the squares used for SEM, and printed cylinders used for clarity. The square and cylinder parts were marked with black permanent marker on one edge to ensure that before and after post-processing measurements are taken at the same location. The comparison evaluated is the percent change from the initial dimensions measured to the dimensions after post-processing for the length and mass measurements were also taken before and after post-processing using a digital analytical balance (Model USS-DBS8).

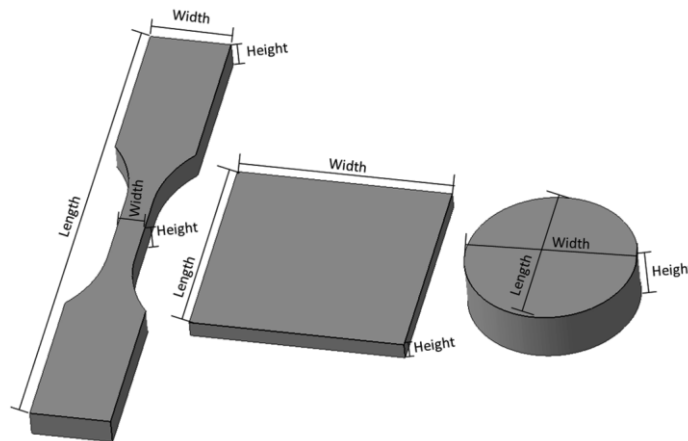


Figure 47: The length dimensions measured before and after post-processing to evaluate dimensional accuracy.

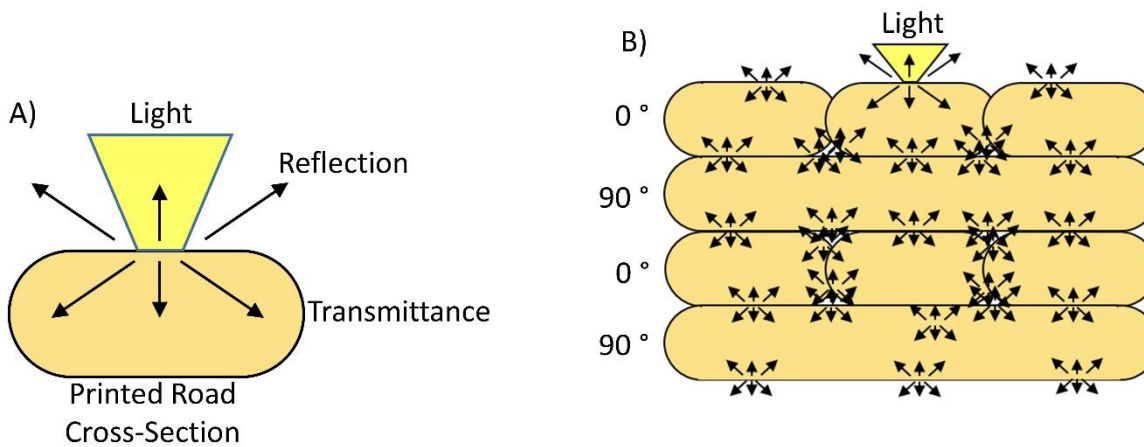
#### 6.2.3.4 Clarity

Prior research has been done to improve the clarity of printed parts. Ahn et. al have shown that the clarity of a FFF printed part using a transparent material is improved using infiltration of cyanoacrylate resin and acrylic resin. The infiltration of another material fills the voids between layers, reducing the number of surfaces and interfaces light can encounter and reflect [156]. Another study that improved part transparency was conducted by Nguyen et. al., whose dried silica-filled ink parts were opaque because of the porous bound powder parts became clear after post-processing where the parts densified completely and become clear [157].

ULTEM® 1010 is a transparent material in the filament form; however, the parts printed out of ULTEM® 1010 can appear opaque. As light hits the part the light is both transmitted and

reflected (Figure 48A) as well as with every interface and hole within the print. Each interface reduces the amount of light that can be transmitted through the part and is absorbed. More interfaces result in opaque parts (Figure 48B), while fewer increase the clarity (Figure 48C). If the printed roads and layers are well bonded, then the number of optical interfaces is reduced. The authors hypothesize that a measurement of the absorbance of the printed parts will correlate to part strength for ULTEM® 1010, and could therefore be used as a Non-Destructive Evaluation (NDE) technique.

To measure absorbance, a set of three cylindrical parts (20 mm diameter, 6 mm tall) were printed. Absorbance was measured using a Synergy H1 Hybrid Reader at 600 nm wavelength and samples were placed into a 12-well flat-bottom plate (typically used for cell cultures). A 31x31 array of measurements was taken for each sample. Because the well diameter was 22 mm and the printed cylinders were 20 mm, a subset of the collected data was used for analysis to ensure that the measurements included the part, regardless of the part placement. The subset was a 12x12 array of measurements centered in the well to use to calculate the average absorbance. Figure 48D shows an example color map of the data for one of the parts, where yellow represents clear and green represents more opaque. This was done for the three printed samples at each temperature setting (total of 432 data points). MATLAB 1-way ANOVA was used for the analysis to determine statistical significance.



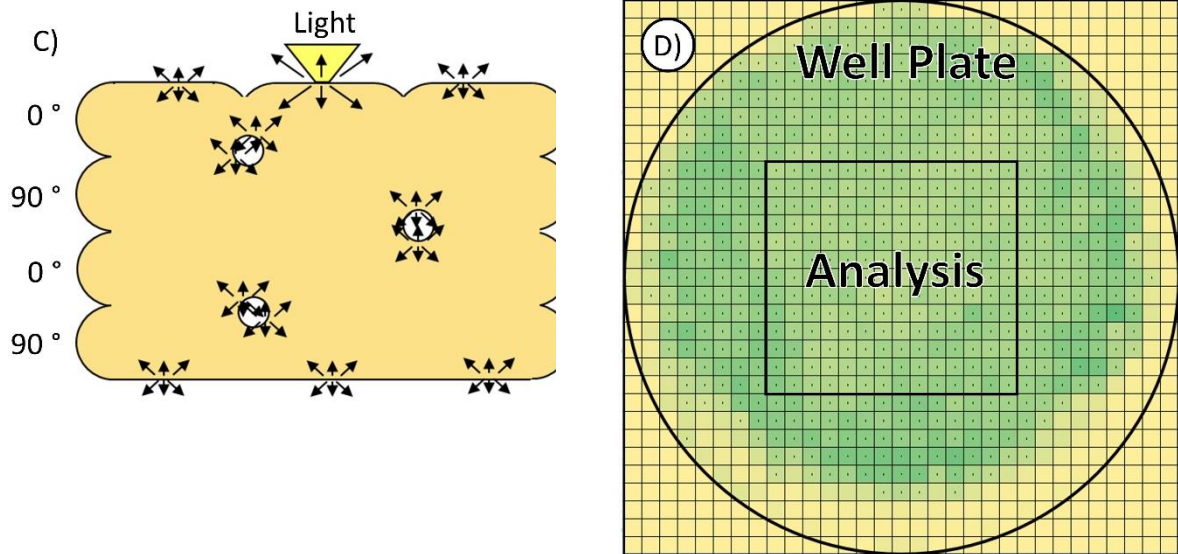


Figure 48: A visualization of light absorbance for a) a printed road, b) a printed part, and c) a well-bonded printed part. D) Example of the collected data for a printed cylinder, using a color map to show absorbance. Data for the analysis was taken from the center of the well plate in a 12x12 array.

## 6.3 Results and Discussion

### 6.3.1 Thermal Characterization

The ULTEM® 1010 filament's thermal degradation, which provides an upper limit for the nozzle temperature, was measured to be 520 °C at 5 wt. % and 495°C for 1 wt. % (Figure 49A). There was up to a 0.05 % weight loss at 360 °C, which is the nozzle temperature used for printing specimens to test the effect of the build environment temperature and post-processing conditions. Therefore, during the printing process, the nozzle was not heated for extended periods without material flowing, or the material would begin to discolor.

The glass transition temperature ( $T_g$ ) was measured to be 217 °C using DSC (Figure 49B). The same transition temperature was observed during cooling. This is expected for an amorphous polymer and verifies that the material will hold its shape once cooled below  $T_g$ . The  $T_g$  is the maximum build environment explored as it should allow the layers to solidify and hold their shape while subsequent layers are printed.

Figure 49C shows the viscosity of ULTEM® 1010 as a function of angular frequency. The viscosity of the material decreases with increasing temperature and shear rates, where slight shear thinning is observed. The printing parameters used in Table 6 produces a maximum shear rate of  $\sim 190 \text{ s}^{-1}$  in the nozzle. The viscosity of materials that can be printed via FFF range from around  $10^3 \text{ Pa}\cdot\text{s}$  [52] to  $10^4 \text{ Pa}\cdot\text{s}$  [158].

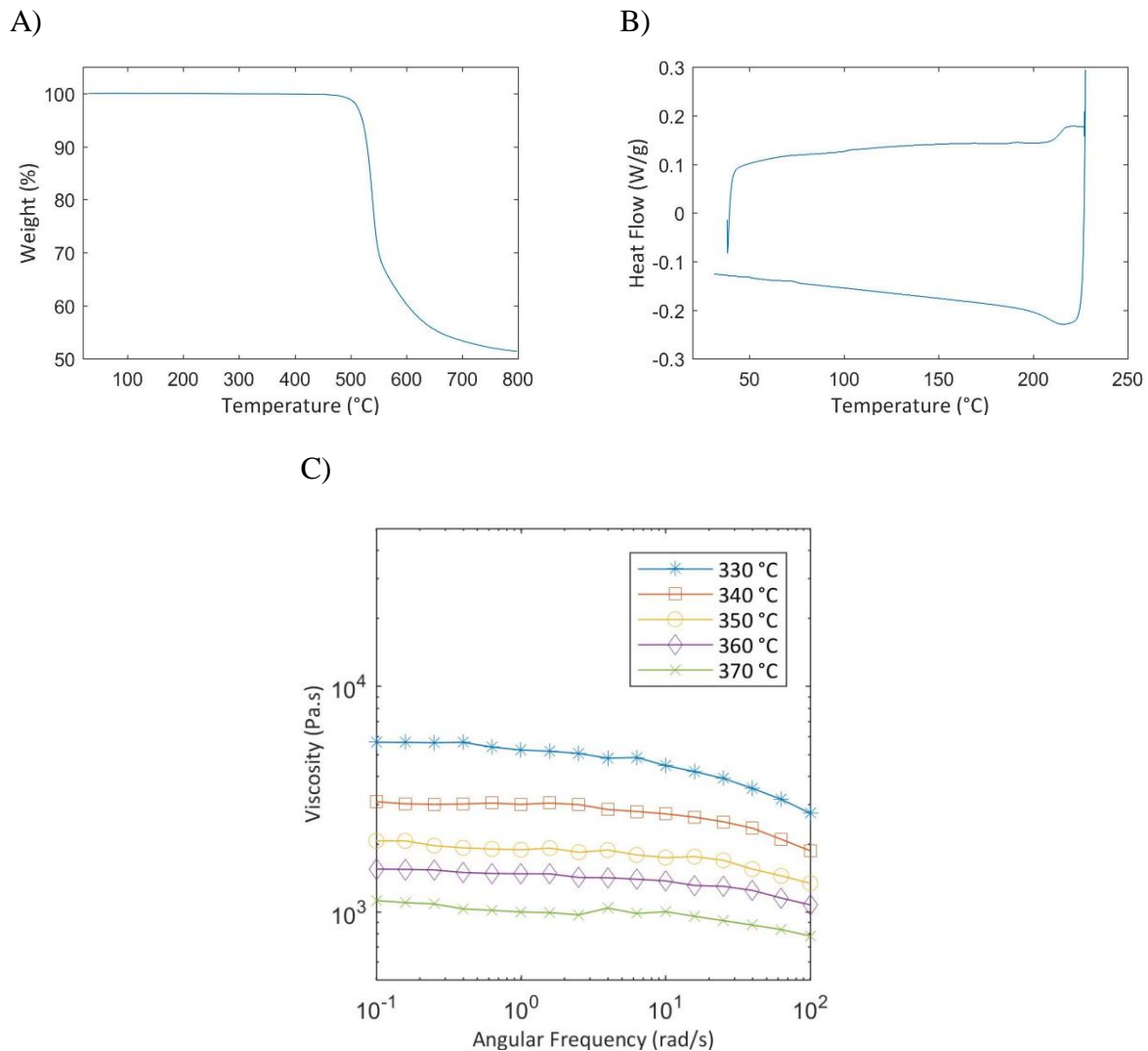


Figure 49: Thermal characterization of ULTEM® 1010 via A) TGA using a 10 °C/min ramp rate to 800 °C, B) DSC first heat and cooling cycle at 10 °C/min (Exo Down), and C) oscillatory rheology at 1% strain at various temperatures.

### 6.3.2 Effects of Nozzle Temperature on Processability and Strength

Specimens were printed at nozzle temperatures ranging between 330-370 °C (Section 6.2.2.2). SEM images of freeze-fractured printed specimens (Figure 50) confirmed that the nozzle temperature affected the interlayer bonding, of the printed parts. The lower nozzle temperature (330 °C) resulted in large voids between printed roads (Figure 50a) and the higher temperature range (360-370 °C) resulted in much smaller voids (Figure 50d-e). With increasing temperature, the interface between the layers becomes less observable with the decreasing of the voids.

The quality of intra/inter-layer bonding is also seen in looking at the fracture surface, where the printed roads from lower nozzle temperatures appear to fracture independently. The parts printed at higher nozzle temperatures showed a more continuous surface, as fracture lines appeared across multiple roads and interfaces.

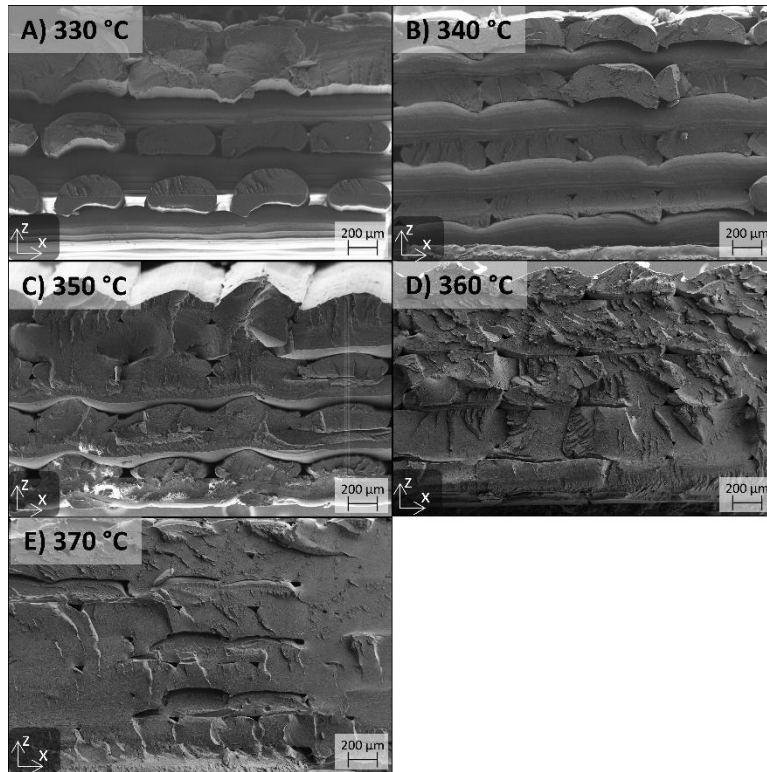


Figure 50: SEM images of freeze fractured printed squares that were printed with nozzle temperatures varying from 330-370 °C with the environment temperature set to 180 °C.

The effects of nozzle temperature on the mechanical properties are quantified in Figure 51. The elastic modulus of the XY tensile specimens had no statistical difference ( $P=1e^{-1}$ ) and the Z specimens' elastic modulus had a slight increase ( $P=1e^{-7}$ ). The yield strength for the XY tensile specimens increased, where the XY specimens ( $P=5e^{-4}$ ) were statistically similar for the parts printed between 350 °C-370 °C. The Z specimens' yield strength were not statistically different ( $P=1e^{-2}$ ); however, there is a statistical difference for the Z specimens printed at 370 °C and both 330°C and 340 °C using a pairwise comparison. The voids observed at the lower nozzle temperatures (Figure 50) showed there is less material within the cross-sections of the tensile bars. Therefore, it is consistent to measure a lower yield strength (38% reduction) for 330 °C when compared to the 360 °C XY tensile specimens. Similarly, the Z specimens are strongest at 370 °C with a 30% increase in strength compared to those printed at 330 °C.

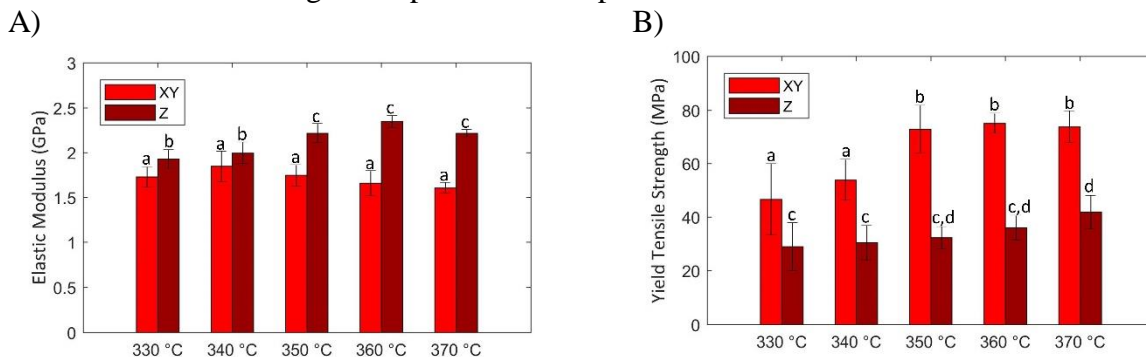


Figure 51: The mechanical properties of ULTEM® 1010 printed using nozzle temperatures between 330-370 °C, where the environment was set to 180 °C. The letters above each column indicate that there is no significant difference between columns with the same letter ( $p>0.05$ ), where XY specimens are only compared to XY specimens and Z specimens are only compared to Z specimens.

Figure 52 shows the mass of the printed coupons that were used for SEM imaging. The mass of the parts increased with the increasing nozzle temperature until about 360 °C, where there is no difference between 360 °C and 370 °C. The increase in mass is also reflected in the SEM images that show a decrease in the size of the voids between the printed roads in Figure 50, where parts printed at 360-370 under °C show highly dense parts. This low mass is attributed to the material’s high viscosity at the lower nozzle temperatures, which causes under-extrusion and results in more porosity and lowers the total part mass (Figure 49C).

The theoretical mass for the model was calculated to be 1.23 g using the measured filament material density ( $0.00127 \text{ g/mm}^3$ ) and the CAD model volume ( $967.4 \text{ mm}^3$ ). The gcode toolpath created by the slicer has filament extrusion commands for a volume of  $950.2 \text{ mm}^3$  resulting in a slightly smaller theoretical mass (1.20 g). All printed specimens had a mass of at least 20% lower than this theoretical mass (Figure 52). Since the SEM images show highly dense parts, the large difference in the measured mass to the theoretical mass could be that there is a larger void located in one area of the part that was not captured in SEM. For example, this could occur at the starting/stopping of extrusion, on an edge (as discussed later in Section 6.3.4), or at a corner which are locations that are consistent in every layer but would not affect the majority of the part. Other sources of error include i) the nozzle being calibrated slightly too close to the bed causing under extrusion on the initial layers, ii) material oozing/stringing between parts (which was removed), and/or iii) the small size of the parts caused reasons i and ii to have a larger percent influence.

Printing with nozzle temperatures of 360-370 °C produced parts with the largest mass (Figure 52) and also the highest degree of fusion between printed roads/layers (Figure 50). Since specimens printed at 360 °C featured a slightly higher yield strength and lower standard deviation (Figure 51), this nozzle temperature was chosen for subsequent experiments.

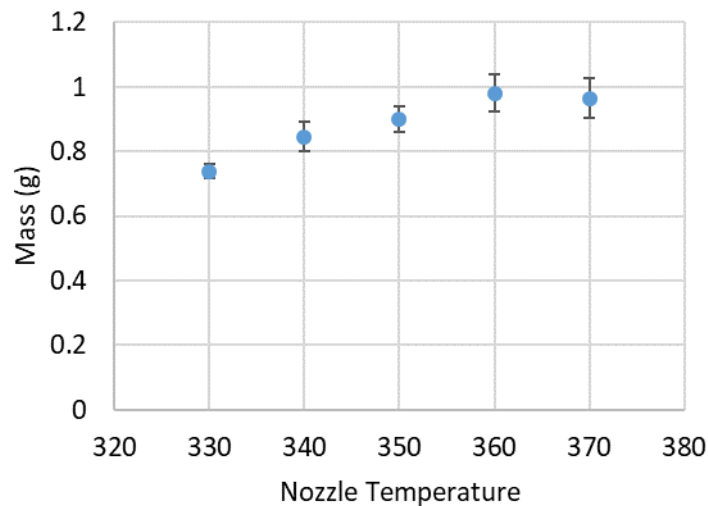


Figure 52: The mass of the printed square specimens used for SEM in relation to the nozzle temperature ( $n=3$ ).

### 6.3.3 Effects of Environment Temperature on Strength and Curling

To study the effect of build environment temp on the interlayer/road fusion of printed parts, SEM images of freeze-fractured surfaces were taken on parts printed at a nozzle temperature of 360 °C (Figure 53). Similar to the earlier experiments on varied nozzle temperatures, parts printed in lower build environment temperatures feature distinct road and layer interfaces. With increasing build environment temperature, the interface within the layer becomes less distinct. The fracture surface of parts printed in the lower build environment temperatures features roads and layers breaking individually, while higher temperature samples fracture surface span across multiple roads and layers. This is the result of the higher environment temperature increasing the bonding potential [36]. By increasing the temperature of the environment the material cools at a slower rate, which allows the previous roads to remain at a higher temperature while subsequent roads are deposited. Remaining above  $T_g$  for longer allows the molecules to remain mobile increasing the polymer chain entanglement at the interface.

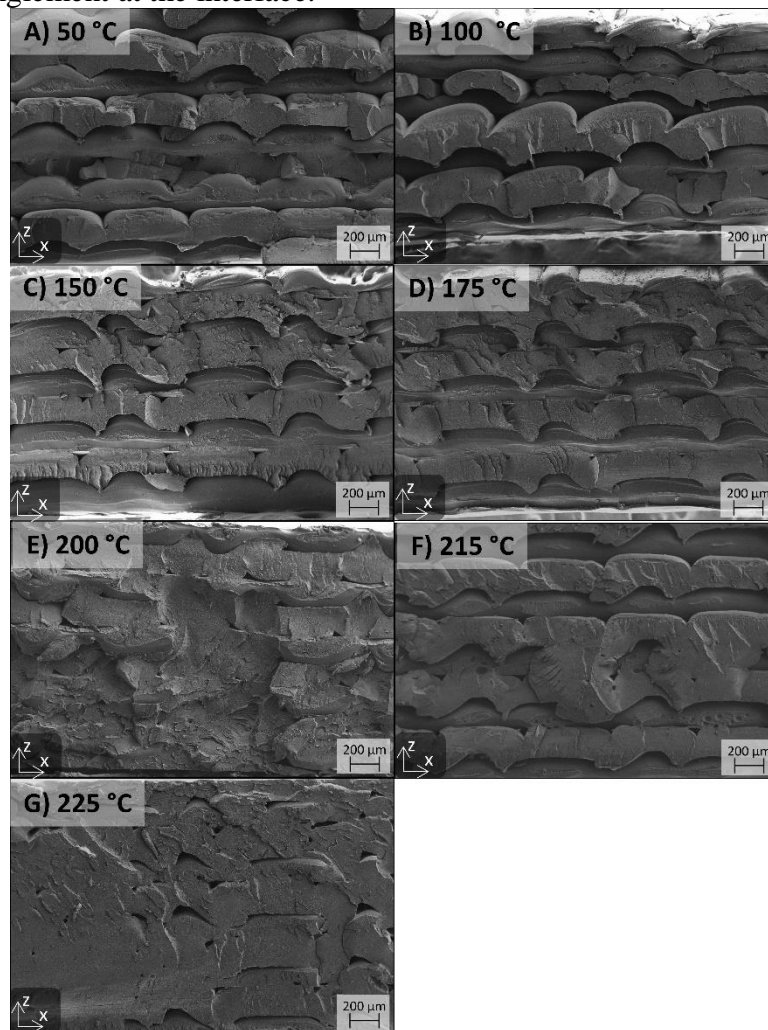


Figure 53: SEM images of freeze fractured printed squares that were printed with environment temperatures varying from 50-225 °C with the nozzle temperature set to 360 °C.

The parts printed in the lowest environment temperatures (50-100 °C) failed during printing by curling and falling off of the inverted print bed. Results from the mechanical testing (Figure

54) generally show an increase in the XY specimens' modulus ( $P=3e^{-3}$ ) and yield strength ( $P=2e^{-4}$ ) with increasing build environment temperature. The specimens had a 27% increase in elastic modulus between 150 °C and 200 °C and a 22% increase between 150 °C and 225 °C. The increase in the XY strength suggests that there is an increase in the intra-layer bonding. However, the Z specimens' modulus remains constant ( $P=8e^{-1}$ ), while the tensile strength decreases up to 36% with increasing temperature ( $P=1e^{-5}$ ). This is surprising because the fracture surface of the parts appears to show increased bonding between layers in parts printed at and above 200 °C. Using a pairwise comparison, there was no difference in the elastic modulus or yield strength between the XY specimens printed at 200 °C and above.

Section 6.1.1 describes how decreasing the temperature difference between the nozzle and the environment reduces the rate of cooling, improving layer bonding. The difference between the XY and Z specimens bonding is due to the variation in time and the deposition path. For the toolpath used, a single layer took 105 s to complete two XY tensile bars where the Z tensile bars took ~8 s at the neck region (the smallest cross-section) of the six tensile bars. Increasing the environment temperature decreases the rate of cooling and the time it takes to cool below  $T_g$  and the heat introduced by the following road also contributes to the reduction of cooling [151]. A shorter time between printed layers means that the positive effects of the build environment might not be as pronounced. In fact, increasing the environment above  $T_g$  decreased the tensile strength for the Z specimens in this experiment. This could be caused by small deformations in the part from remaining above  $T_g$  and/or increased stringing of the material between the parts, due to higher temperatures that decrease the melt viscosity.

The FFF part strength is highly dependent on the size, shape, and orientation of the part (such as the tensile specimens) as well the size, shape, and orientation of any other parts printed in the same build. Large parts, or parts with large cross-sections (such as the XY specimens), have a disadvantage where there is more time for the roads to cool before printing the adjacent roads and layers. Thus, these types of parts benefit more from increases in the environment temperature.

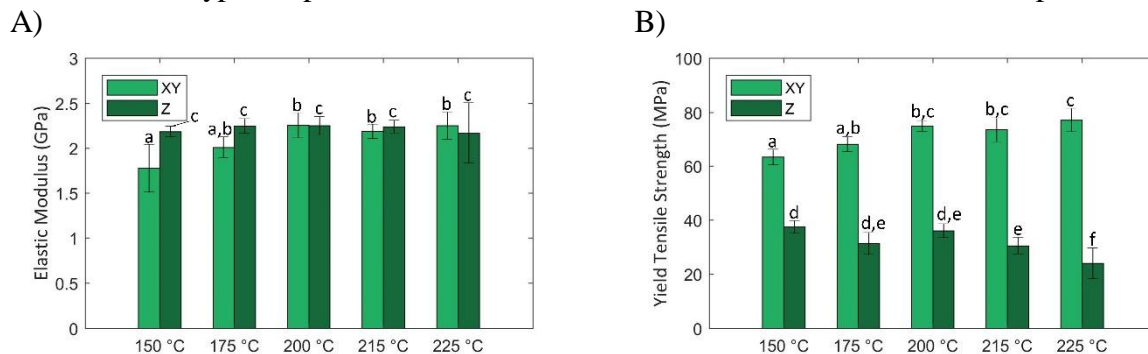


Figure 54: The mechanical properties of ULTEM® 1010 printed using different environment temperatures. The letters above each column indicate that there is no significant difference between columns with the same letter ( $p>0.05$ ), where XY are only compared to XY and Z are only compared to Z.

Figure 55 shows images of printed parts next to a vertical ruler to measure curling. Part curling decreased when printed in hotter environment temperatures. The authors believe the slight curling for specimens printed in the 215 °C and 225 °C environments may be caused by the removal from the PEI sheet while it was still hot. As the environment temperature approaches  $T_g$  (217°C) the deflection of the printed part is eliminated, as residual stresses from rapid cooling are reduced. Part

curling produces a linear relationship between the environment temperature and the deflection of a printed part. Figure 56 presents the data from measuring the extent of curling on both ends of the printed tensile specimens. The resultant data follows a linear trend, which aligns with the linear trend in warp deformation (mm) vs chamber temperature predicted by Wang’s model of warping in FFF processes [144].

Environment temperatures >200 °C provided the highest increase in intra-layer strength (Figure 54) and the largest decrease in curling (Figure 56). In order to prevent possible excessive oozing from the nozzle while printing, the authors recommend an environment temperature of 200 °C for the print parameters used (Table 6).

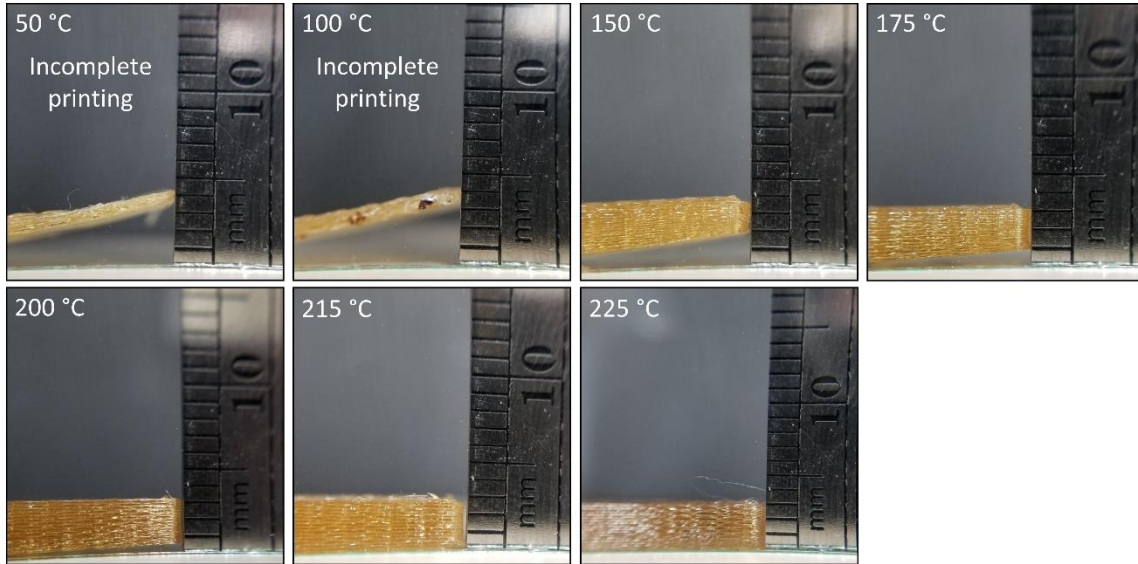


Figure 55: Images of tensile bar curling when printed in a heated environment at various temperatures. (Nozzles temperature was 360 °C)

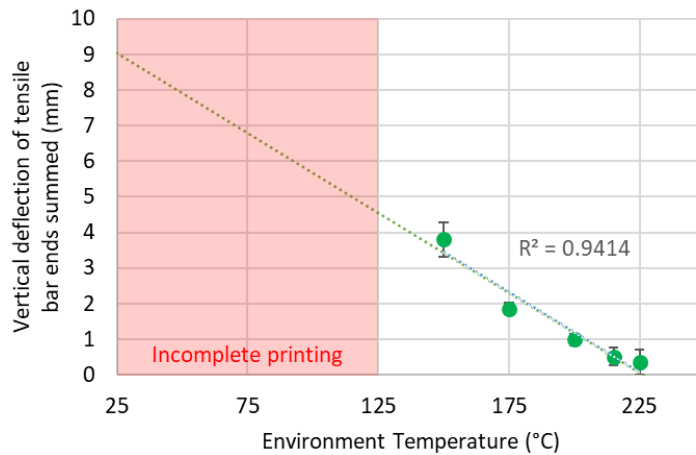


Figure 56: The sum of the curling on both ends of the XY tensile bars printed using a nozzle temperature of 360 °C in various environment temperatures.

#### 6.3.4 Effects of Post-Processing Conditions on Strength and Dimensional Accuracy

Parts printed with a nozzle temperature of 360 °C in a 200 °C environment were post-processed at 260 °C for varying times (6, 12, 18, and 24 hrs.) to induce additional inter-layer entanglement. However, for amorphous thermoplastics such as ULTEM® 1010, maintaining the temperature of the parts above  $T_g$  can result in dimensional deformation. To counteract this, the authors embedded printed parts into a container with packed, pulverized salt, as described in Section 6.2.2.4.

Figure 57 provides images of the printed parts following post-processing at 260 °C at different durations. As can be seen, the parts are not significantly deformed on a macro-scale using the powder embedding technique. The parts post-processed for shorter time periods (6-12 hrs.) are paler in color when compared to the longer times (18-24 hrs.). This may indicate a slight degradation of the material. Some of the part surfaces feature a white tint due to the surface defects from the removal of the salt.

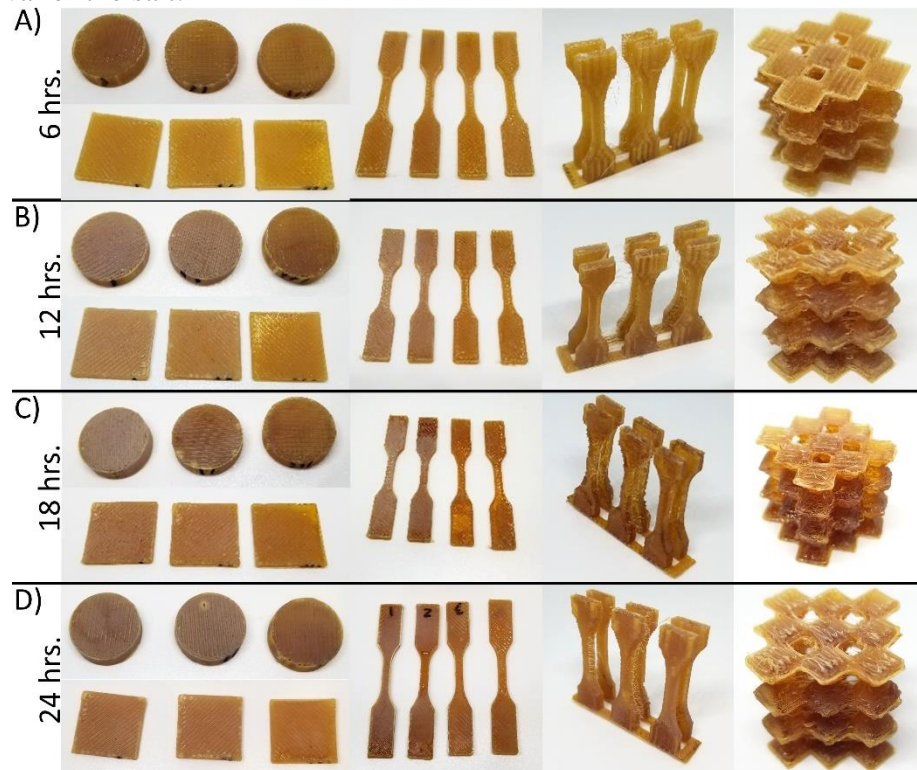


Figure 57: Image of the printed parts after post-processing at 260 °C for A) 6 hrs., B) 12 hrs., C) 18 hrs., and D) 24 hrs.

SEM images of freeze-fractured parts were taken to explore the internal interlayer/road bonding in relation to the post-processing time (Figure 58). An image was taken in the middle and at an edge of a printed specimen for each post-processing time period. It is observed that the shape and size of the voids between the printed roads are significantly different in parts that were not post-processed (Figure 58A) and parts that were post-processed (Figure 58B-E). Hart et. al. have previously shown how the long thin voids between printed roads form a grid-like pattern before thermal post-processing. It was shown that post-processing above  $T_g$  for a prolonged time (18 hrs. at 175 °C for ABS) resulted in the coalescence of the voids into spherical air pockets at semi-regular intervals [153]. A similar phenomenon is observed in these experiments with ULTEM® 1010, where the observed voids appear larger and more frequent in the cross-section images at

longer processing times. The spherical voids are larger in diameter than the long thin voids between the roads; the part is more likely to break where there is the largest collection of voids during the freeze-fracture process. With increasing time, the frequency of the voids decreases (Figure 58B through Figure 58D) due to the coalescence of the pockets of air. Given enough molecular mobility, the small voids near the perimeter of the part may escape the bounds of the part. However, a number of the voids appear to coalesce to a large void located near the edge of the part. The large pocket on the edge appears to be the result of a gap in the interface between the perimeter roads and the infill (Figure 58A). Another observation is that all of the post-processed printed parts experience a more uniform fracture surface within the material. The interfaces between layers virtually disappear when post-processed above  $T_g$  for any extended time period.

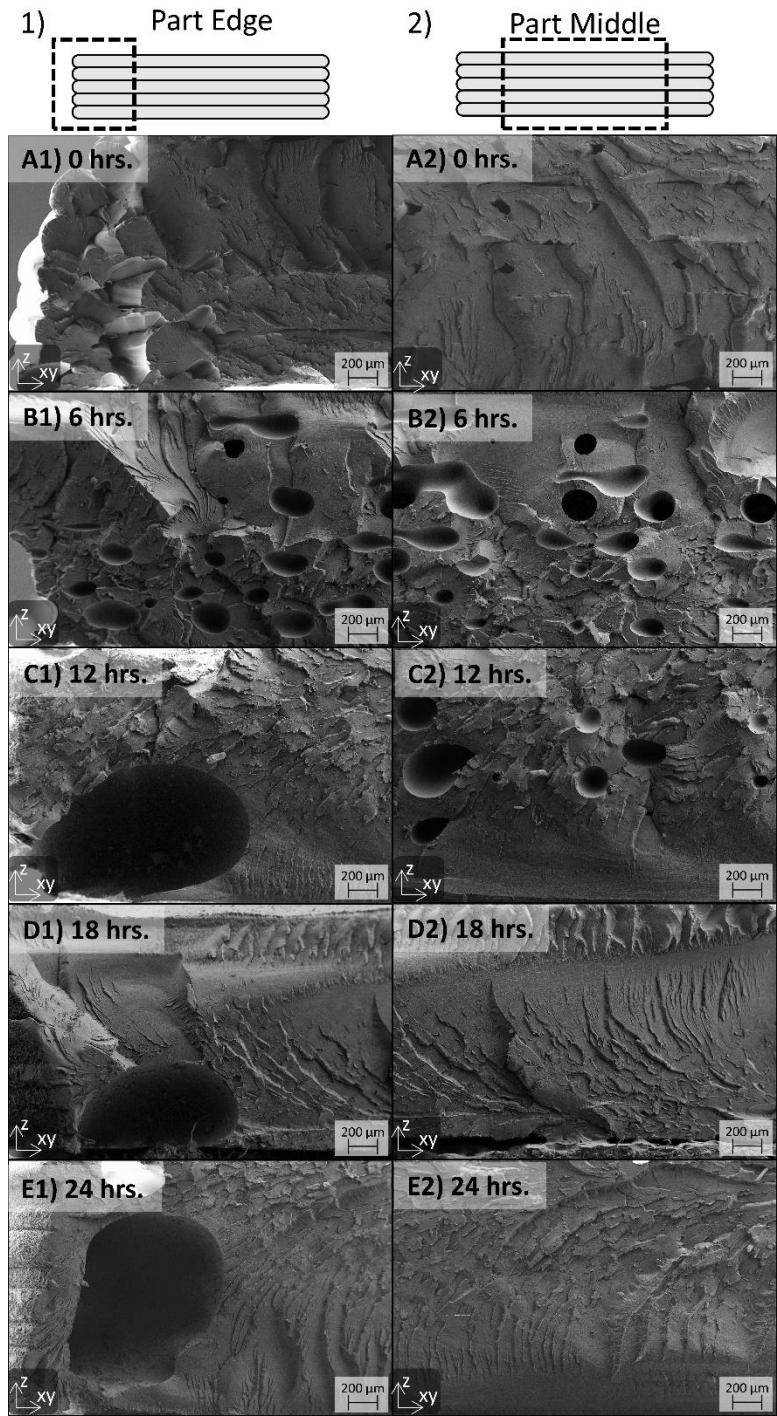


Figure 58: SEM images of freeze fractured printed squares that were post-processed at 260 °C for times ranging from 0 to 24hrs.

Additional SEM images were taken on the exterior surface of the printed parts to observe the effects of the powdered salt on surface quality. Figure 59 shows a comparison of the sides of a printed part with no post-processing and 24 hrs. of post-processing. While the dissolved salt particles resulted in external pockmarks on the part surface, there was no observed diffusion of salt into the part. Although creating a rougher surface may be undesirable, the defects are on the

order of  $\sim 1\text{-}130\ \mu\text{m}$ , whereas the typical layer interface road curvature and interfacial surfaces occur every  $\sim 200\ \mu\text{m}$  (set by the layer height print parameter) and have a depth variation up to  $200\ \mu\text{m}$  (assuming the road is an obround shape).

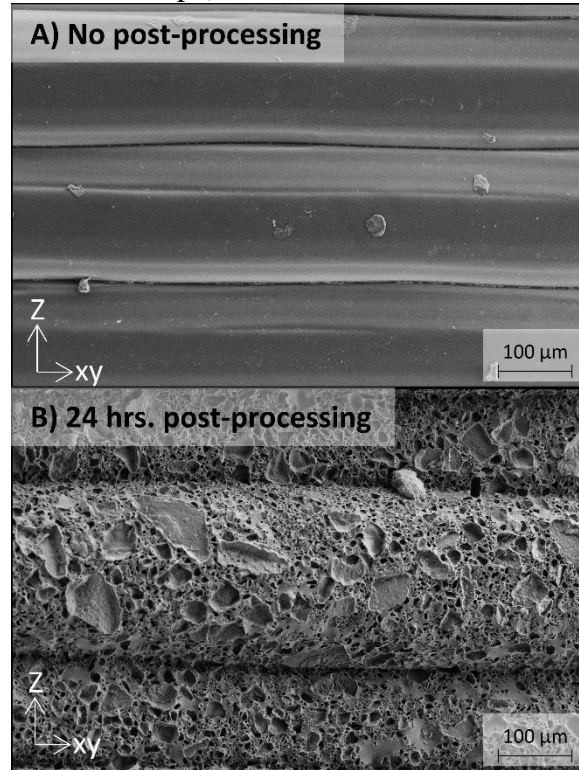


Figure 59: SEM images of the exterior of a printed part that a) used no post-processing and b) was post-processed at  $260\ ^\circ\text{C}$  for 24 hrs.

Results from mechanical testing specimens with and without this post-processing treatment are shown in Figure 60. The XY specimens had a maximum of 18% increase in elastic modulus and 27% in the yield strength for the parts post-processed for 18 hrs. Statistical analysis was not completed for the XY specimens due to a difference in sample size, where a tensile bar was discarded from processing error. The Z specimens increased up to 41% from 0 hrs. for the elastic modulus ( $P=6e^{-5}$ ) and a 50% increase in the yield strength ( $P=2e^{-5}$ ), where the post-processed parts were all statistically different from the parts that were not post-processed for both properties.

The load direction for the XY specimens pulled along the layers, which were previously improved by increasing the environment temperature. The Z bonding improves substantially with this post-processing technique, beyond the in-printer process parameter changes. The largest increase in yield strength between two adjacent post-processing times was 36% for the Z tensile bars, which occurred between no post-processing and six hours of post-processing. This shows how post-processing for even a short amount of time can make a large difference in improving the inter-layer bonding. The tensile strength continued to increase up to 18 hrs. However, after 18 hrs. there was a decrease in both the elastic modulus and the yield strength. This is caused by i) the material degrading (as seen in the discoloration in Figure 57), and ii) by the coalesced voids breaking the surface of two out of the six Z specimens in the neck region, creating larger irregular cavities on the part surface (Figure 61). The results show an isotropy value of 89% (average Z

specimen strength divided by average XY specimen strength [118]) in the printed parts' yield strength.

The Z specimens' yield strength is lower than that of the XY specimens because they featured large voids that were aligned with the specimen gauge length and often were connected to the part's surface (Figure 61). In contrast, the XY tensile specimens exhibited smaller, more discrete closed voids. These voids change the effective area for evaluation of the elastic modulus; however, the stress was not adjusted for the effective area because it is an inherent part of the processing. In order to be able to make the printed parts truly isotropic, the printing process needs to be modified to minimize the voids created between printed roads. For example, it has been shown in FFF literature that decreasing the spacing between roads can create a more dense part with increased strength [47].

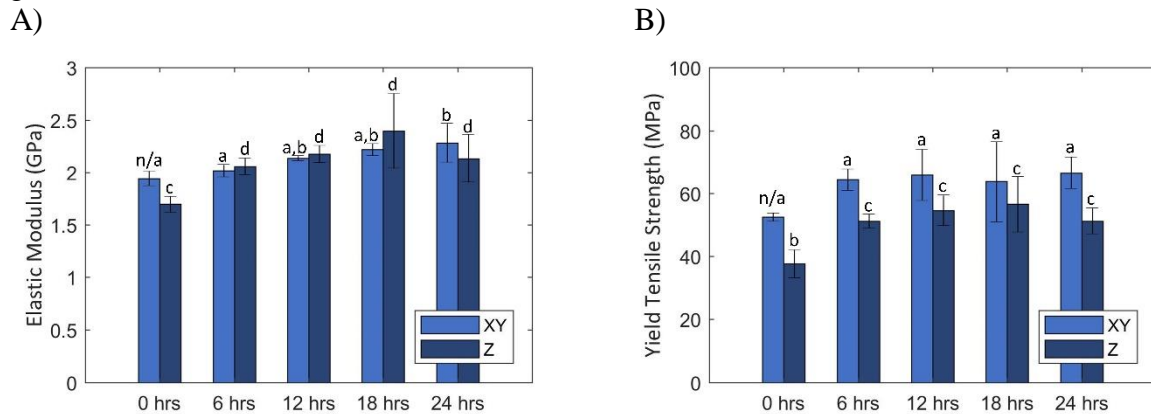


Figure 60: The mechanical properties of ULTEM® 1010 post-processed at 260 °C for different periods of time. The letters above each column indicate that there is no significant difference between columns with the same letter ( $p > 0.05$ ), where XY are only compared to XY and Z are only compared to Z.

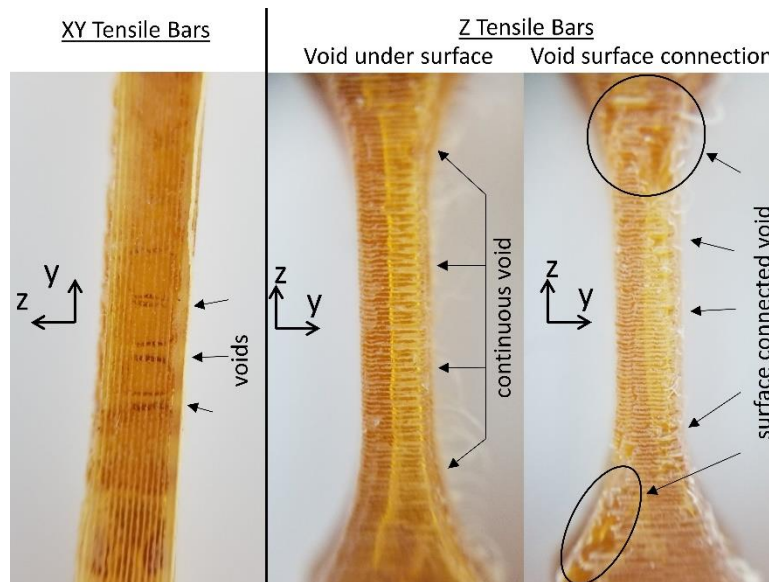


Figure 61: The neck of XY and Z tensile bars post-processed for 24 hrs. The cross-section of each neck is ~3.175 mm.

Figure 62 shows the results of the percent change in the dimensions and mass of the printed parts after post-processing when compared to before post-processing. Recognizing that the order in which the parts were packed in the salt could impact dimensional accuracy (i.e., parts packed on the bottom experience a greater load than the parts packed on the top), the dimensional stability of the parts is also plotted with respect to their packing layer (Figure 44) in Figure 62B. The average change of the part dimensions is  $< -1\%$  irrespective of post-processing time and layer packing. The slight reduction in size is likely caused by the coalescence of the internal voids. The largest dimensional change observed is the vertical tensile bars post-processed for 18 hours ( $-8.2-12.7\%$ ). The authors suspect that the outliers in the data were the result of variation in the packing process. All of the changes seen had a nominal maximum of 0.4 mm and a maximum percent difference of 12% from the printed part. Although it is desirable to have very accurate printing, this variation is within the accuracy of the printer used. The maximum difference seen from this set of data is equivalent to one nozzle diameter. This may be acceptable for applications where precision under 1 mm is irrelevant.

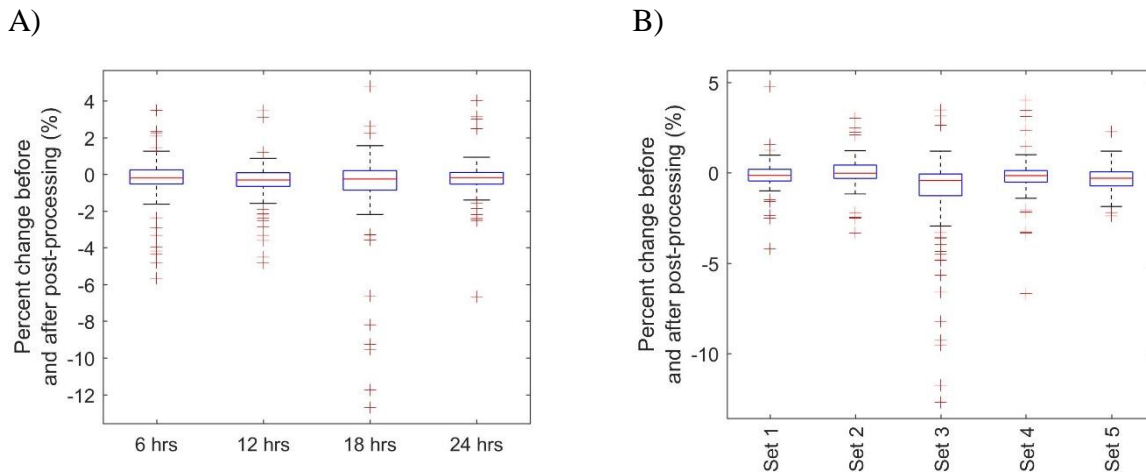


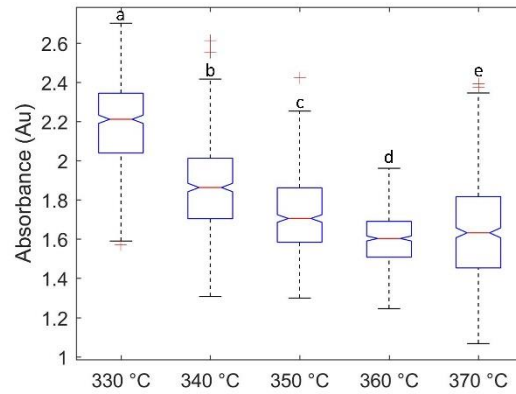
Figure 62: The percent change for the dimensional measurements (length and mass) taken before and after post-processing parts shown A) by post-processing time and by B) the layer in which the parts were packed in salt (where set 1 was on the bottom and set 5 was on top, Figure 44).

### 6.3.5 Light Absorption as an Indicator of Part Strength

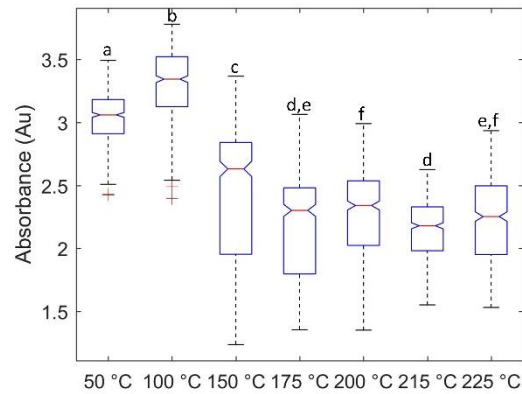
Figure 63 shows the light absorbance for the printed parts with varying processing and post-processing conditions. There is an inverse correlation between the absorbance of light and the XY tensile strength for the parts printed using a varying nozzle and environment temperatures when comparing Figure 63A and Figure 63B to Figure 51 and Figure 54 respectively. The higher processing temperatures reduce the number of voids and interfaces between the roads. In turn, this decreases the absorbance of light through the part. One-way ANOVA shows that the parts' absorbance for the different nozzle temperature are all statistically different ( $P < 0.05$ ) (Figure 63A). The absorbance of parts printed in environments of 150 °C and below are statistically different from each other. A pairwise comparison shows that there is not a statistical difference between parts printed in these environment pairs: 200 °C with 225 °C, 225 °C with 175 °C, and 175 °C with 215 °C (Figure 63B). This is consistent with the tensile data where the yield strength has very little variation when parts were printed above 175 °C. These results demonstrate that clarity of an ULTEM®1010 part can be used as a non-destructive means to evaluate the strength of the printed part.

In contrast to these results, the post-processed parts did not show the same inverse correlation between absorptivity and strength; instead, the parts had a higher absorbance for the parts that had a higher yield strength. The absorbance measured for each post-processing condition was evaluated to be statistically different. The surface roughness created from the post-processing powder (Figure 59) inhibited the transmittance of light. Thus, light absorbance is not an appropriate means for verifying the strength of parts that have been post-processed via the authors' salt embedding technique, without mitigating the surface roughness.

A)



B)



C)

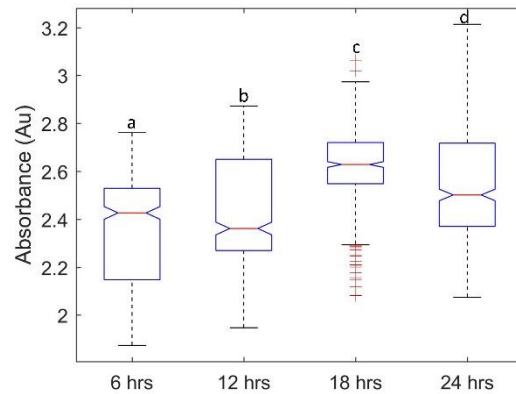


Figure 63: Absorbance measurements of light for the varying a) nozzle temperatures, b) environment temperatures, and c) post-processing time. The letters above each column indicate that there is no significant difference between columns with the same letter ( $p > 0.05$ ).

#### 6.4 Summary and Future Work

The overall goal of this work is to explore the effects of thermal (post-)processing conditions on the quality of FFF ULTEM® 1010 parts. Specifically, the extrusion nozzle, build environment temperature, and thermal post-process conditions were varied to explore their impact on tensile strength, elastic modulus, dimensional accuracy, and light absorptivity. Nozzle temperatures at and exceeding 360 °C (printing at 15 mm/sec) created stronger parts due to a more consistent flow of the material in the nozzle. Lower nozzle temperatures caused under-extrusion and part defects. Build environment temperatures of 200 °C and higher increased the printed material's intra-layer bonding, due to a slower rate of cooling and a longer time spent above  $T_g$ . By printing closer to the  $T_g$  of the material, the residual stresses within the material that induce curling were eliminated, which provided higher dimensional accuracy.

In order to enable thermal post-processing of printed parts above  $T_g$  without imposing deformation, the parts were embedded into powdered salt, which was later removed via water. Post-processing at 260 °C (approximately 40 °C above  $T_g$ ) caused an increase in the Z tensile strength that was not observed in changing the nozzle temperature or environment temperature. Embedded parts in powdered salt retained the parts' shape while being held above the material's glass transition temperature for extended periods. A <1% linear shrinkage was observed in the parts following post-processing; however, this dimensional change is smaller than the accuracy of the printer. While the dissolution of the pulverized salt introduced surface defects, these defects are significantly smaller than the layer interfaces.

In addition, the authors found an inverse correlation between the mechanical strength and the absorbance of printed ULTEM 1010® parts, which could be used as a non-destructive means to verify part quality. The same correlation was not seen for the post-processed parts, due to the surface defects from post-processing in powder. In future research, the authors will explore formalizing this post-processing technique as a non-destructive evaluation quality control approach following additional studies on different types of transparent materials, on larger parts, and the creation of a model to predict material strength based on the clarity.

## 7. Summary

### 7.1 Summary of Research

**The overall research goal of this work was to expand the library of materials that can be printed using material extrusion additive manufacturing.** In order to expand the library of materials and to gain a better understanding of the structure-process-properties relationship for FFF, two material needs cases were identified i) *a water-soluble material for incorporating actives* and ii) *processing high-temperature high-performance polymers*. These two goals enable the processing of materials that expand outside the standard FFF temperature range (190-260 °C) by enabling materials that process at much lower (70 °C) and much higher (360 °C) temperatures.

#### 7.1.1 Research Question 1

The first research question is motivated by the concept of 3D printing pharmaceuticals. Using FFF has distinct advantages when compared to other AM processes, as described in Section 2.1. The challenge in processing with FFF is that processing at FFF's typical high-temperatures causing the actives to become ineffective.

<b>Research Question 1</b>
How can active ingredients, that cannot be processed at high temperatures (<100 °C), be incorporated into a water-soluble 3D part processed by FFF for tailored release?

The work proposed to answer this research question is focused on enabling the ability to print with a material below 100 °C. The first approach is to create a material that can be printed at a low-temperature with sufficient material characteristics for FFF. A material was developed by Pekkanen and co-authors [24] that uses ionic interactions to tune the material properties within a SPEG polymer series. Hypothesis 1.1.1 states that the use of ionic salt can affect relevant material properties to enable FFF printing.

<b>Sub-Question 1.1</b>	
How can a low processing temperature dissolvable material be modified to be processable via FFF?	
<b>Hypothesis 1.1.1</b>	<b>Hypothesis 1.1.2</b>
An ionic salt can be added to an existing polymer chain of a low processing temperature dissolvable material (PEG) to create discrete points of polar charges. Different counterions in the salt have different ionic interaction strength. Changing the ionic interaction strength changes the material properties to allow the ability to tune a material's properties to enable material extrusion.	An ionic filler added to a low processing temperature dissolvable ionic polymer can influence the ionic interactions within the material. Using an ionic filler with a stronger ionic charge can influence the material properties in a similar way as changing counterions within a sulfonated ionic polymer. This allows for the ability to tune material properties using a filler material, in place of material synthesis.

The use of the different ionic salts in the SPEG material (Chapter 2) resulted in varying viscosity (Figure 5) and the crystallization kinetics (Figure 8). Although each of the counterions used in the polymer series resulted in a similar percent crystallinity, the crystallization rate and

spherulite size varied drastically. The  $\text{Ca}^{2+}$  counterion resulted in the most accurate part with the highest bonding quality due to its high viscosity ( $\sim 10^4$  Pa-s), which enabled the material to hold its shape, and with a small spherulite size ( $< 10 \mu\text{m}$ ), which prevented the part from warping. This knowledge gained can serve as a guide for modifying other low processing temperature or semi-crystalline materials for FFF.

Although the SPEG polymer containing the  $\text{Ca}^{2+}$  counterion produced the best print quality, the process used to exchange the counterions makes the material difficult to produce on a larger scale. Hypothesis 1.1.2 uses the knowledge gained from the evaluation of the SPEG series to evaluate the potential of using ionic fillers to produce a tunable printable material (Chapter 3). By incorporating an ionic filler ( $\text{CaCl}$ ), the material was able to replicate the material properties of SPEG polymer containing the  $\text{Ca}^{2+}$  counterion, which corresponded to improved printability without exchanging the counterion.

The work completed in Chapters 2 and 3 resulted in two new materials that process at a low-temperature, are water-soluble, and can be processed via FFF for the potential of incorporating active ingredients directly into the polymer to address Research Question 1.

The other potential solution outlined in Sub-Question 1.2 is to incorporate active ingredients by not directly adding them into the material, but instead embedding them into a designed cavity inside of a printed part. This would allow for tailored release times by altering the part geometry wall thickness and the incorporation of multiple active ingredients that could be released at different times.

<b>Sub-Question 1.2</b>
How can active ingredients be incorporated into a printed part, without adding the actives directly into the material for tailored release?
<b>Hypothesis 1.2</b>
Active ingredients in a liquid or powder form can be embedded into a printed soluble material, where the wall thickness of the printed material will create a time delay for release of multiple active ingredients.

Chapter 4 addressed Sub-Question 1.2 using Hypothesis 1.2 to embed liquid and powdered active agents into printed parts. A list of design considerations was developed and used for creating liquid-tight parts for FFF. Parts were printed with an in-situ liquid embedding technique that successfully held the material. Parts were printed with varying wall thicknesses to determine the time of release. The observed linear trend was then used to inform the release time of a variety of wall geometries and multi-release chambers (Figure 31).

The work completed in Chapter 4 resulted in the incorporation of materials into printed parts that could not themselves be printed. This method is a less direct way to address the overall research goal to expand the material library for FFF printing by embedding other materials into FFF parts. The methods developed for liquid embedding can be applied to other applications that require a liquid component in their manufactured parts like plant fertilization or part self-healing, where a glue that solidifies in air is embedded.

#### 7.1.2 Research Question 2

The second research question of this research explored the effect of the mechanical strength and dimensional accuracy for FFF printing a high-temperature, high-performance amorphous polymer. ULTEM<sup>®</sup> 1010 is used in applications where a combination of high-strength, light-

weight, chemical resistance, and/or dimensional stability at a high temperature is required. Thus when printing with ULTEM® 1010, the resulting part must exhibit high-strength properties.

<b>Research Question 2</b>
How does temperature affect the mechanical strength and dimensional accuracy for FFF printing a high-temperature, high-performance amorphous polymer ULTEM® 1010?

The sub-question addressed the need for a low-cost, desktop-scale open-architecture FFF system that can achieve the high-temperature environment for processing high-temperature polymers, as described in Chapter 5.

<b>Sub-Question 2.1</b>
How can a desktop material extrusion machine be modified to enable high-performance materials?
<b>Hypothesis 2.1</b>
A heated environment is essential for printing high-performance polymers (e.g. PPSF). An inverted heat chamber with an open bottom will trap heat within only the printing area, while an open bottom allows for free movement of the print head.

Hypothesis 2.1 states that an inverted heat chamber could use natural convection to trap heat and allow for full movement of the print head for a compact desktop-scale FFF printer. This hypothesis was created after an evaluation of the design criteria to design a high-temperature system, where the printer components are compatible with, protected from, or removed from the high-temperature. The concept of the inverted heat chamber was modeled using CFD software, verified experimentally, and validated by observing improved part strength of the high-performance polymer PPSF when compared to room temperature environments (Chapter 5).

After building the desktop-scale high-temperature system, the machine was used to address Research Question 2, which focused on studying the influence of the thermal processing conditions on the mechanical strength and dimensional accuracy of the high-performance polymer Ultem 1010.

<b>Hypothesis 2.2</b>
Optimizing the processing temperatures, the strength and dimensional accuracy can be improved. However, incorporating post-processing above $T_g$ the strength can be improved beyond what printing can achieve.

Hypothesis 2.2 was addressed in Chapter 6, wherein Ultem 1010 was printed and optimized with varying nozzle temperatures, environment temperatures, and post-processing conditions. The nozzle temperature controls the flow of the material through the nozzle and was required to be at least 360 °C when printing at 15 mm/sec to prevent under-extrusion. Build environment temperatures of 200 °C and higher produced parts that exhibited higher intra-layer strength and decreased warping. A post-processing technique was developed to prevent the parts from deforming while remaining above  $T_g$ . The parts were embedded in powdered salt to support the shape of the parts during thermal post-processing. The results showed the most improvement for inter-layer bonding by post-processing at 260 °C for 18 hrs. Additionally, tests showed an inverse

correlation between part clarity and strength, suggests this analysis could be used as a NDE technique for verifying part quality.

The machine design in Chapter 5 was used for the study of Ultem 1010 in Chapter 6 to address Research Question 2 and the overall research goal. The machine design and the post-processing technique developed can be used to enable and improve the part quality and strength for FFF printing of high-performance polymers.

## 7.2 Publications

Each of the Chapters 2-6 represent a completed, or planned, peer-reviewed publication that resulted from this work. Listed below are the publication titles, the corresponding research questions they address, and the current status.

<i>Chapter</i>	<i>Related Research Question</i>	<i>Title</i>
2	RQ1.1	C.E. Zawaski, E.M. Wilts, C.A. Chatham, A.T. Stevenson, A.M. Pekkanen, C. Li, A.R. Whittington, T.E. Long, C.B. Williams, Tuning the material properties of a water-soluble ionic polymer using different counterions for material extrusion additive manufacturing, <i>Polymer (Guildf)</i> . 176 (2019) 283–292.
3	RQ1.1	C.E. Zawaski, C.A. Chatham, E.M. Wilts, T.E. Long, C.B. William, Using Fillers to Tune Material Properties of an Ion-containing Semi-crystalline Poly(ethylene glycol) for Fused Filament Fabrication Additive Manufacturing Processing, <i>Addit. Manuf.</i> (Prepared for submission)
4	RQ1.2	C.E. Zawaski, E. Margareta, A.T. Stevenson, A.M. Pekkanen, A.R. Whittington, T.E. Long, C.B. Williams, Embedding of liquids into water soluble materials via additive manufacturing for timed release, <i>Addit. Manuf.</i> (Prepared for submission)
5	RQ2.1	C. Zawaski, C. Williams, Design of a low-cost, high-temperature inverted build environment to enable desktop-scale additive manufacturing of performance polymers, <i>Addit. Manuf.</i> 33 (2020). <a href="https://doi.org/10.1016/j.addma.2020.101111">https://doi.org/10.1016/j.addma.2020.101111</a> .
6	RQ2.2	C. Zawaski, C. Williams, The effect of Fused Filament Fabrication Thermal Processing Conditions on the mechanical strength and dimensional accuracy on ULTEM®1010, <i>Addit. Manuf.</i> (Prepared for submission)

Other presentations related to this work include:

### Poster Presentations

- **Zawaski C.E.** and Williams C.B., “Tailoring Dissolution via Additive Manufacturing of Water Soluble Polymers” *Macromolecules Innovation Institute Technical Conference*, Blacksburg, VA, October 11, 2016.
- **Zawaski C.E.**, Pekkanen A.M., Wilts E.M., Long T.E., Williams C.B., “Molecules to Manufacturing: Designing for Filament Material Extrusion” *Southeast Polymer Forum* 2017 June 6th, Blacksburg, VA, 2017

- **Zawaski C.E.**, Wilts E.M., Long T.E., and Williams C.B. “Using Fillers to Improve Printability of Semi-Crystalline Materials for Material Extrusion Additive Manufacturing” *MII Technical Conference*, Blacksburg VA, April 17, 2018
- **Zawaski, C.E.**, Williams, C.B. “The Impact of Thermal Processing Conditions on Mechanical Strength and Dimensional Accuracy for Fused Filament Fabrication of Ultem 1010” *MII Technical Conference*, Blacksburg VA, Nov 4-6, 2019

#### Oral Presentations

- **Zawaski C.E.**, Stevenson A.T., Pekkanen A.M., Whittington A.R., Long T.E., and Williams C.B., “Tailoring Geometry to control dissolution of water soluble materials via additive manufacturing” *Solid Freeform Fabrication Conference (SFF)*, Austin Texas August, 2017
- **Zawaski C.E.** and Williams C.B., “Design of a Low Cost, Desktop-scale, High Temperature System for Fused Filament Fabrication of High Performance Polymers”, *Solid Freeform Fabrication Conference (SFF)*, Austin Texas August, 2018
- **Zawaski C.E.**, Chatham C.A., Wilts E.M., Long T.E., and Williams C.B. “Using Fillers to Improve Printability of a Water Soluble Semi-Crystalline Polymer for Material Extrusion Additive Manufacturing”, *Solid Freeform Fabrication Conference (SFF)*, Austin Texas August, 2018
- **Zawaski C.E.**, Stevenson A.T., Pekkanen A.M., Long T.E., Whittington A.R., and Williams C.B. “Using 3D Printing to Embed Liquids into Water Soluble Materials for Timed Release toward Pharmaceutical Applications”, *Graduate Research Symposium*, Blacksburg VA March, 2019
- **Zawaski C.E.** and Williams C.B. “The Impact of Thermal Processing Conditions on Mechanical Strength and Dimensional Accuracy for Fused Filament Fabrication of Ultem 1010” *Solid Freeform Fabrication Symposium*, Austin Texas August, 2019

#### Intellectual property

- T. Hodgdon, D. Graham, M. Farrel, C. Kenneally, C. Williams, **C. Zawaski**, Water Soluble Containers and Methods of Making Them, US 2019/0002172 A1, 2019.
- T. Hodgdon, D. Graham, F. Barnabas, C. Williams, **C. Zawaski**, T. Long, A. Pekkanen, B. White, Polymeric Materials and Articles Manufactured There From, US 2019/0309163 A1, 2019.
- T. Hodgdon, D. Graham, F. Barnabas, C. Kenneally, C. Williams, **C. Zawaski**, T. Long, A. Pekkanen, B. White, Polymeric Materials and Articles Manufactured There From, US 2019/0309238 A1, 2019.
- T. Hodgdon, T. Long, A. Pekkanen, A. Whittington, C. Williams, **C. Zawaski**, D. Graham, C. Kenneally, F. Barnabas, A. Stevenson, Polymertic Materials and Articles Manufactured There from, US 2020/0086551 A1, 2020.
- T. Hodgdon, T. Long, A. Pekkanen, A. Whittington, C. Williams, **C. Zawaski**, D. Graham, C. Kenneally, F. Barnabas, A. Stevenson, Method for manufacturing a Three-Dimensional Object, US 10,543,639 B2, 2020.
- **C. Zawaski**, C. Williams, High temperature 3d printing via inverted heated build chamber, US 2020/0047412 A1, 2020.

#### Co-author publications

- A.M. Pekkanen, C. Zawaski, A.T. Stevenson, R. Dickerman, A.R. Whittington, C.B. Williams, T.E. Long, Poly(ether ester) ionomers as water-soluble polymers for material

extrusion additive manufacturing processes, *ACS Appl. Mater. Interfaces*. 9 (2017) 12324–12331. <https://doi.org/10.1021/acsami.7b01777>.

- E.L. Gilmer, D. Miller, C.A. Chatham, C. Zawaski, J.J. Fallon, A. Pekkanen, T.E. Long, C.B. Williams, M.J. Bortner, Model analysis of feedstock behavior in fused filament fabrication: Enabling rapid materials screening, *Polymer (Guildf)*. 152 (2018) 51–61. <https://doi.org/10.1016/j.polymer.2017.11.068>.
- C.A. Chatham, C.E. Zawaski, D.C. Bobbitt, R.B. Moore, T.E. Long, C.B. Williams, Semi-Crystalline Polymer Blends for Material Extrusion Additive Manufacturing Printability: A Case Study with Poly(ethylene terephthalate) and Polypropylene, *Macromol. Mater. Eng.* 304 (2019) 1–11. <https://doi.org/10.1002/mame.201800764>.
- Stevenson, R. Dickerman, C. Zawaski, C. Williams, A. Whittington, Ionic Sulfonated Polyethylene Glycols Incorporating  $\alpha$ -amylase for Multi-Processing Applications, *Chemistry of Materials*, Submitted
- Das, C. Chatham, J. Fallon, C. Zawaski, E. Gilmer, C. Williams, M. Bortner, Current understanding and challenges in additive manufacturing of high-temperature engineering thermoplastic polymers, *Additive Manufacturing*, Accepted 2020
- X. Chen, C. Zawaski, G. Spiering, B. Liu, C. Orsino, R. Moore, C. Williams, T. Long, Taking Advantage of Quadruple Hydrogen Bonding in Polyurea Supramolecular Elastomers for Melt Extrusion Additive Manufacturing, in-progress for submission

## 7.3 Contributions

### 7.3.1 Intellectual merits

Through the process of modifying the material, machine, and process for expanding the available materials for FFF AM, the following scientific contributions were made:

- An understanding of how nucleation density and spherulite size of a semi-crystalline material affect the material properties relevant to FFF processing. (Chapter 2)
- An understanding of how ionic interactions affect material properties, and how different counterions or fillers can be used to tune the material properties to enable and improve printability. (Chapter 2 & Chapter 3)
- A methodology for embedding liquids and powders into thin-wall FFF printed structures. (Chapter 4)
- A demonstration of a controlled delay in the release of dissolvable capsules by altering the wall thickness of FFF printed parts. (Chapter 4)
- A novel FFF design to print high-temperature, high-performance polymers on desktop-scale systems. (Chapter 5)
- An understanding of the effects of processing temperatures on mechanical strength and dimensional accuracy of a high-temperature, high-performance, amorphous polymer. (Chapter 6)
- A post-processing technique for solid FFF parts to increase inter-layer adhesion while maintaining the printed parts' shape. (Chapter 6)

### 7.3.2 Broader impacts

By investigating the crystallization kinetics and material properties of the sulfonated PEG polymer series, the information can be used in designing and modifying other semi-crystalline materials for FFF. Semi-crystalline materials are typically not used for FFF due to the sudden change in material properties (e.g. volume, viscosity) as the material crystallizes. By understanding

the crystallization kinetics, developing FFF semi-crystalline materials will become easier to screen for FFF.

The embedding liquid process establishes a new method for achieving a timed release. The process of embedding liquids/powders can be translated into other applications. The ability to time release may be applied to drug delivery, water treatment, or plant treatment.

The heated build environment chamber developed in this work enables desktop FFF machines to print a wider variety of materials to include high-performance materials with high thermal transitions. The chamber developed in this work was designed at a low-cost, which enables more researchers and users to be able to afford this capability and thus bring new materials to the FFF market.

Ideal process parameters were identified for printing ULTEM<sup>®</sup> 1010. However, using the understanding of the relationship between the nozzle temperature and the material flow and the environment temperature with intra-layer bonding and curling can provide a more strategic way of optimizing thermal processing conditions for other polymers. Additionally, the salt-powder post-processing developed can be applied to any amorphous polymer to improve the inter-layer bonding of printed parts.

The combination of this all of the elements of this work demonstrates the ability to change the material, machine, or process to enable the printing of new materials. Combinations of these approaches will greatly increase the available materials for material extrusion AM and will allow for materials to be tailored for specific applications and for taking advantage of AM's ability to produce customized parts.

#### 7.4 Future Work

While this dissertation contained many contributions, there are still many questions that can be answered by further research. Each of the research questions have various unique opportunities for the continuation of work. This section discusses the next steps that could be taken for each of the research areas. Each step also includes the Chapters of relevance.

##### 7.4.1 Pharmaceutical

By designing a new material that is FFF processed at a low-temperature and is dissolvable has enabled the potential for direct incorporation of active ingredients inside of the material for 3D printing. However, in order to use this ability for applications such as pharmaceutical, there is work in the pharmaceutical field that needs to be completed including:

- Testing the SPEG with the Ca<sup>+2</sup> counterion and/or the SPEG with CaCl<sub>2</sub> filler for biocompatibility. (Chapters 2 and 3)
- Testing for undesirable interactions between active agents and the material. (Chapters 2 and 3)

##### 7.4.2 Tailored Dissolution

Outside of the pharmaceutical safety specifications, there is also research in the area of tailoring the dissolution profile. This could include unit cell geometries and/or complex infill patterns to alter how the actives are released. Future work in this area would include:

- Measuring the diffusion of a trackable material contained within the matrix polymer. (Chapters 2, 3, and 4)
- Testing how the geometry of a dissolvable material can alter the release profile and create more complex releases for tailored dissolution. (Chapters 2, 3, and 4)

#### 7.4.3 Structure-process-property relationship

On the aspects of printability, there is potential in gaining a larger understanding of the structure-process-property relationship by further investigation. Listed are ideas for potential future work for continued study of the structure-process-property relationship:

- Explore how spherulite size and crystallization rate influence volumetric shrinkage and the direction of shrinkage. (Chapters 2 and 3)
- Determine if using nucleating agents can control the direction of shrinkage for a semi-crystalline material and reduce/eliminate the warpage for 3D-printing other semi-crystalline polymers. (Chapters 2 and 3)
- Test if creating liquid-tight parts using liquid embedding techniques can be used to increase mechanical strength by decreasing the gaps in the printed roads. (Chapters 4)

#### 7.4.4 Development

Finally, on the manufacturing side, there is still developmental work in order to enable the use of the liquid-embedding methodology. This includes:

- Creating a slicer using liquid embedding techniques to automate creating optimal toolpaths for liquid-tight parts. (Chapters 4)

#### 7.4.5 Modeling high-temperature FFF

The inverted heat chamber work featured a simple model used for a proof of concept of the chamber itself. This model can be expanded to include a more accurate representation of the environment and part temperatures during printing by:

- Incorporating a moving print head into a 3D inverted chamber model to more accurately represent the temperature profile during printing. (Chapter 5)
- Modeling and testing a part being printed in the inverted configuration to calculate the temperature profile of the part and test larger-scale parts ability to adhere to the bed (where mass and gravity may have a larger effect). (Chapter 5)

#### 7.4.6 Designing and Building the Inverted FFF system

The FFF system design created in Chapter 5 was built as a prototype system for testing Hypothesis 2.1. There are design improvements that need to be done in order to be able to use the system for more applications and future research. The main improvements include:

- Building a larger inverted chamber to allow for the printing of larger parts and to verify the inverted thermal model is valid for scale-up. This would include creating a moving bed or a longer print head. (Chapter 5)
- Designing and implementing a cooling mechanism for the printed head that is well insulated from the environment. This can be used to test Ultem 1010 at higher nozzle temperatures and other high-performance polymers. (Chapters 5 and 6)

#### 7.4.7 Further investigation

Chapter 7 introduced two new concepts, salt embedding post-processing and using clarity as a non-destructive evaluation, which require further research and investigation. Listed are suggested focuses for the next steps for these new concepts:

- Determining the optimal particle size for post-processing in embedded salt. (Chapter 6)
- An investigation of surface coating materials for powder embedding to protect the part from defects created by the powder and be removed from the part after thermal post-processing. (Chapter 6)

- An in-depth study of the correlation between mechanical strength and optical clarity for transparent materials. (Chapter 6)

## References

- [1] ISO/ASTM, "Standard Terminology for Additive Manufacturing - General Principles - Technologies." ISO/ASTM International 2016, 2015, doi: 10.1520/F2792-12A.2.
- [2] I. Gibson, D. Rosen, and B. Stucker, *Additive Manufacturing Technologies 3D Printing, Rapid Prototyping, and Direct Digital Manufacturing*, Second Edi. Springer, 2015.
- [3] Wohlers Associates, *Wohlers Report*. 2019.
- [4] A. M. S. Ibrahim, R. R. Jose, B. T. Lee, and S. J. Lin, "Three-dimensional printing in Developing Countries," *PRS Glob. Open*, 2015, doi: 10.1097/GOX.0000000000000298.
- [5] C. L. Ventola, "Medical Applications for 3D Printing: Current and Projected Uses.," *P&T*, vol. 39, no. 10, pp. 704–711, 2014, doi: 10.1016/j.infsof.2008.09.005.
- [6] J. Norman, R. D. Madurawe, C. M. V Moore, M. A. Khan, and A. Khairuzzaman, "A new chapter in pharmaceutical manufacturing : 3D-printed drug products ☆ , ☆☆," *Adv. Drug Deliv. Rev.*, vol. 108, pp. 39–50, 2017, doi: 10.1016/j.addr.2016.03.001.
- [7] M. A. Alhnan, T. C. Okwuosa, M. Sadia, K. Wan, W. Ahmed, and B. Arafat, "Emergence of 3D printed dosage forms : Opportunities and challenges," *Pharm. Res.*, vol. 33, pp. 1817–1832, 2016, doi: 10.1007/s11095-016-1933-1.
- [8] J. Goole and K. Amighi, "3D printing in pharmaceuticals: A new tool for designing customized drug delivery systems," *Int. J. Pharm.*, vol. 499, no. 1–2, pp. 376–394, Feb. 2016, doi: 10.1016/j.ijpharm.2015.12.071.
- [9] L. K. Prasad and H. Smyth, "3D Printing technologies for drug delivery: a review," *Drug Dev. Ind. Pharm.*, vol. 42, no. 7, pp. 1019–1031, Jul. 2016, doi: 10.3109/03639045.2015.1120743.
- [10] J. Norman, R. D. Madurawe, C. M. V. Moore, M. A. Khan, and A. Khairuzzaman, "A new chapter in pharmaceutical manufacturing: 3D-printed drug products," *Adv. Drug Deliv. Rev.*, vol. 108, pp. 39–50, Jan. 2017, doi: 10.1016/j.addr.2016.03.001.
- [11] A. Goyanes *et al.*, "3D printing of medicines: Engineering novel oral devices with unique design and drug release characteristics," *Mol. Pharm.*, vol. 12, no. 11, pp. 4077–4084, Nov. 2015, doi: 10.1021/acs.molpharmaceut.5b00510.
- [12] A. Goyanes, A. B. M. Buanz, G. B. Hatton, S. Gaisford, and A. W. Basit, "3D printing of modified-release aminosaliclate (4-ASA and 5-ASA) tablets," *Eur. J. Pharm. Biopharm.*, vol. 89, pp. 157–162, Jan. 2015, doi: 10.1016/j.ejpb.2014.12.003.
- [13] Stratasys, "Solution Guide: Certified Additive Manufacturing for Aircraft Interiors, ISO 9001:2008 Certified." Stratasys, 2017.
- [14] Sabic, "ULTEM Resin 1010," 2020. .
- [15] C. Zawaski *et al.*, "Embedding of Liquids into Water Soluble Materials via Additive Manufacturing for Timed Release," *Solid Free. Fabr. Proc.*, pp. 2047–2059, 2017.
- [16] T. C. Okwuosa, C. Soares, V. Gollwitzer, R. Habashy, P. Timmins, and M. A. Alhnan, "On demand manufacturing of patient-specific liquid capsules via co-ordinated 3D printing and liquid dispensing," *Eur. J. Pharm. Sci.*, vol. 118, no. February, pp. 134–143, 2018, doi: 10.1016/j.ejps.2018.03.010.
- [17] A. Melocchi, F. Parietti, G. Loreti, A. Maroni, A. Gazzaniga, and L. Zema, "3D printing by fused deposition modeling ( FDM ) of a swellable / erodible capsular device for oral pulsatile release of drugs," *J. Drug Deliv. Sci. Technol.*, vol. 30, pp. 360–367, 2015, doi:

- 10.1016/j.jddst.2015.07.016.
- [18] M. D. Billy Dunn, "NDA Approval 207958," 2015. doi: Reference ID: 3800218.
- [19] D. G. Yu, X. L. Yang, W. D. Huang, J. Liu, Y. G. Wang, and H. Xu, "Tablets with material gradients fabricated by three-dimensional printing," *J. Pharm. Sci.*, vol. 96, no. 9, pp. 2446–2456, Sep. 2007, doi: 10.1002/jps.20864.
- [20] D. G. Yu *et al.*, "Oral fast-dissolving DDD fabricated using 3DP," in *2008 2nd International Conference on Bioinformatics and Biomedical Engineering*, May 2008, pp. 1602–1605, doi: 10.1109/ICBBE.2008.729.
- [21] W. Wu, Q. Zheng, X. Guo, J. Sun, and Y. Liu, "A programmed release multi-drug implant fabricated by three-dimensional printing technology for bone tuberculosis therapy," *Biomed. Mater.*, vol. 4, p. 065005, Dec. 2009, doi: 10.1088/1748-6041/4/6/065005.
- [22] M. Kyobula *et al.*, "3D inkjet printing of tablets exploiting bespoke complex geometries for controlled and tuneable drug release," *J. Control. Release*, vol. 261, no. June, pp. 207–215, Sep. 2017, doi: 10.1016/j.jconrel.2017.06.025.
- [23] A. Goyanes, F. Fina, A. Martorana, D. Sedough, S. Gaisford, and A. W. Basit, "Development of modified release 3D printed tablets (printlets) with pharmaceutical excipients using additive manufacturing," *Int. J. Pharm.*, vol. 527, no. 1–2, pp. 21–30, Jul. 2017, doi: 10.1016/j.ijpharm.2017.05.021.
- [24] A. M. Pekkanen *et al.*, "Poly(ether ester) ionomers as water-soluble polymers for material extrusion additive manufacturing processes," *ACS Appl. Mater. Interfaces*, vol. 9, no. 14, pp. 12324–12331, Apr. 2017, doi: 10.1021/acsami.7b01777.
- [25] A. T. Stevenson, R. Dickerman, C. E. Zawaski, C. B. Williams, and A. R. Whittington, "Ionic sulfonated polyethylene glycols incorporating  $\alpha$ -amylase for multi-processing applications."
- [26] L. Rodgers and V. Jaker, "Semi-crystalline build materials," US 2015/0252190 A1, 2015.
- [27] Y. Li, Z. Yao, Z. Chen, S. Qiu, C. Zeng, and K. Cao, "High melt strength polypropylene by ionic modification: Preparation, rheological properties and foaming behaviors," *Polymer (Guildf.)*, vol. 70, pp. 207–214, Jul. 2015, doi: 10.1016/j.polymer.2015.06.032.
- [28] E. B. Orler, B. H. Calhoun, and R. B. Moore, "Crystallization kinetics as a probe of the dynamic network in lightly sulfonated syndiotactic polystyrene ionomers," *Macromolecules*, vol. 29, no. 18, pp. 5965–5971, Jan. 1996, doi: 10.1021/ma960003p.
- [29] J. A. Johnson *et al.*, "Phase-controlled, heterodyne laser-induced transient grating measurements of thermal transport properties in opaque material," *J. Appl. Phys.*, vol. 111, no. 2, p. 023503, Jan. 2012, doi: 10.1063/1.3675467.
- [30] J. A. Johnson *et al.*, "Direct measurement of room-temperature nondiffusive thermal transport over micron distances in a silicon membrane," *Phys. Rev. Lett.*, vol. 110, no. 2, p. 025901, Jan. 2013, doi: 10.1103/PhysRevLett.110.025901.
- [31] M. P. Short *et al.*, "Applications of transient grating spectroscopy to radiation materials science," *JOM*, vol. 67, no. 8, pp. 1840–1848, Aug. 2015, doi: 10.1007/s11837-015-1496-3.
- [32] J. Cuffe *et al.*, "Reconstructing phonon mean-free-path contributions to thermal conductivity using nanoscale membranes," *Phys. Rev. B*, vol. 91, no. 24, p. 245423, Jun. 2015, doi: 10.1103/PhysRevB.91.245423.
- [33] A. J. Minnich, "Multidimensional quasiballistic thermal transport in transient grating

- spectroscopy," *Phys. Rev. B*, vol. 92, no. 8, p. 085203, Aug. 2015, doi: 10.1103/PhysRevB.92.085203.
- [34] T. Kim, D. Ding, J. Yim, Y. Jho, and A. J. Minnich, "Elastic and thermal properties of free-standing molybdenum disulfide membranes measured using ultrafast transient grating spectroscopy," *APL Mater.*, vol. 5, no. 8, p. 086105, Aug. 2017, doi: 10.1063/1.4999225.
- [35] C. Li, Y. Ma, and Z. Tian, "Thermal switching of thermoresponsive polymer aqueous solutions," *ACS Macro Lett.*, vol. 7, no. 1, pp. 53–58, Jan. 2018, doi: 10.1021/acsmacrolett.7b00938.
- [36] Y. Yan, R. Zhang, G. Hong, and X. Yuan, "Research on the bonding of material paths in melted extrusion modeling," *Mater. Des.*, vol. 21, no. 2, pp. 93–99, Apr. 2000, doi: 10.1016/S0261-3069(99)00058-8.
- [37] J. E. Seppala and K. D. Migler, "Infrared thermography of welding zones produced by polymer extrusion additive manufacturing," *Addit. Manuf.*, vol. 12, pp. 71–76, Oct. 2016, doi: 10.1016/j.addma.2016.06.007.
- [38] Q. Sun, G. M. Rizvi, C. T. Bellehumeur, and P. Gu, "Effect of processing conditions on the bonding quality of FDM polymer filaments," *Rapid Prototyp. J.*, vol. 14, no. 2, pp. 72–80, Mar. 2008, doi: 10.1108/13552540810862028.
- [39] C. Ajinjeru *et al.*, "Determination of melt processing conditions for high performance amorphous thermoplastics for large format additive manufacturing," *Addit. Manuf.*, vol. 21, pp. 125–132, 2018, doi: 10.1016/j.addma.2018.03.004.
- [40] Y. B. Li, W. J. Weng, K. Cheng, P. Y. Du, G. Shen, and G. R. Han, "Complexes of Ca(II) with polymers as precursors for preparation of amorphous calcium phosphate," *Mater. Sci. Technol.*, vol. 20, no. 9, pp. 1075–1078, Sep. 2004, doi: 10.1179/026708304225019740.
- [41] C. Duty *et al.*, "A viscoelastic model for evaluating extrusion-based print conditions," *Solid Free. Fabr. Symp.*, pp. 495–506, 2017.
- [42] E. L. Gilmer *et al.*, "Model analysis of feedstock behavior in fused filament fabrication: Enabling rapid materials screening," *Polymer (Guildf.)*, vol. 152, pp. 51–61, Sep. 2018, doi: 10.1016/j.polymer.2017.11.068.
- [43] C. Bellehumeur, L. Li, Q. Sun, and P. Gu, "Modeling of bond formation between polymer filaments in the fused deposition modeling process," *J. Manuf. Process.*, vol. 6, no. 2, pp. 170–178, Jan. 2004, doi: 10.1016/S1526-6125(04)70071-7.
- [44] J. E. Seppala, S. Hoon Han, K. E. Hillgartner, C. S. Davis, and K. B. Migler, "Weld formation during material extrusion additive manufacturing," *Soft Matter*, vol. 13, no. 38, pp. 6761–6769, 2017, doi: 10.1039/C7SM00950J.
- [45] P. C. Painter and M. M. Coleman, *Structure and morphology*. DEStech Publications, Inc., 2009.
- [46] A. Bellini and S. Güçeri, "Mechanical characterization of parts fabricated using fused deposition modeling," *Rapid Prototyp. J.*, vol. 9, no. 4, pp. 252–264, Oct. 2003, doi: 10.1108/13552540310489631.
- [47] S. H. Ahn, M. Montero, D. Odell, S. Roundy, and P. K. Wright, "Anisotropic material properties of fused deposition modeling ABS," *Rapid Prototyp. J.*, vol. 8, no. 4, pp. 248–257, 2002, doi: 10.1108/13552540210441166.
- [48] A. M. Peterson, "Review of acrylonitrile butadiene styrene in fused filament fabrication: A plastics engineering-focused perspective," *Addit. Manuf.*, vol. 27, no. March, pp. 363–

- 371, 2019, doi: 10.1016/j.addma.2019.03.030.
- [49] N. E. Zander, M. Gillan, and R. H. Lambeth, "Recycled polyethylene terephthalate as a new FFF feedstock material," *Addit. Manuf.*, vol. 21, no. January, pp. 174–182, 2018, doi: 10.1016/j.addma.2018.03.007.
- [50] N. E. Zander, M. Gillan, Z. Burckhard, and F. Gardea, "Recycled polypropylene blends as novel 3D printing materials," *Addit. Manuf.*, vol. 25, no. October 2018, pp. 122–130, 2019, doi: 10.1016/j.addma.2018.11.009.
- [51] C. A. Chatham, C. E. Zawaski, D. C. Bobbitt, R. B. Moore, T. E. Long, and C. B. Williams, "Semi-Crystalline Polymer Blends for Material Extrusion Additive Manufacturing Printability: A Case Study with Poly(ethylene terephthalate) and Polypropylene," *Macromol. Mater. Eng.*, vol. 304, no. 5, pp. 1–11, 2019, doi: 10.1002/mame.201800764.
- [52] C. E. Zawaski *et al.*, "Tuning the material properties of a water-soluble ionic polymer using different counterions for material extrusion additive manufacturing," *Polymer (Guildf.)*, vol. 176, pp. 283–292, 2019.
- [53] A. A. D'souza and R. Shegokar, "Polyethylene glycol (PEG): a versatile polymer for pharmaceutical applications," *Expert Opin. Drug Deliv.*, vol. 13, no. 9, pp. 1257–1275, 2016, doi: 10.1080/17425247.2016.1182485.
- [54] I. Gibson, D. Rosen, and B. Stucker, *Additive Manufacturing Technologies*. Springer, 2008.
- [55] K. Sawallisch, *Compounding of sheet molding compound*, vol. 23, no. 1. 1984.
- [56] D. Rosato, D. Rosato, and M. Rosato, "Molding Materials," in *Injection Molding Handbook*, Third edit., New York: Springer Science+Buisness Media, 2000, pp. 501–511.
- [57] A. J. Poslinski, M. E. Ryan, R. K. Gupta, S. G. Seshadri, and F. J. Frechette, "Rheological Behavior of Filled Polymeric Systems I. Yield Stress and Shear-Thinning Effects," *J. Rheol. (N. Y. N. Y.)*, vol. 32, no. 7, pp. 703–735, 1988, doi: 10.1122/1.549987.
- [58] A. C. Karmaker and J. A. Youngquist, "Injetion Molding of polypropylene reinfoced with short jute fibers," *J. Appl. Phys.*, vol. 62, pp. 1147–1151, 1996.
- [59] Z. Xie, X. Wu, A. J. Giacomini, G. Zhao, and W. Wang, "Suppressing shrinkage/warping of PBT injection molded parts with fillers," *Polym. Compos.*, vol. 39, no. 7, pp. 2377–2384, 2018, doi: 10.1002/pc.24218.
- [60] M. Spoerk, J. Sapkota, G. Weingrill, T. Fischinger, F. Arbeiter, and C. Holzer, "Shrinkage and warpage optimization of expanded-perlite-filled polypropylene composites in extrusion-based additive manufacturing," *Macromol. Mater. Eng.*, vol. 302, no. 10, pp. 1–13, 2017, doi: 10.1002/mame.201700143.
- [61] C. Ajinjeru *et al.*, "The Influence of Rheology on Melt Processing Conditions of Amorphous Thermoplastics for Big Area Additive Manufacturing (BAAM)," *Solid Free. Fabr. 2016*, pp. 754–761, 2016.
- [62] B. Khatri, K. Lappe, D. Noetzel, K. Pursche, and T. Hanemann, "A 3D-printable polymer-metal soft-magnetic functional composite-development and characterization," *Materials (Basel)*, vol. 11, no. 189, 2018, doi: 10.3390/ma11020189.
- [63] C. Kukla, J. Gonzalez-Gutierrez, I. Duretek, S. Schuschnigg, and C. Holzer, "Effect of particle size on the properties of highly-filled polymers for fused filament fabrication," *AIP Conf. Proc.*, vol. 1914, p. (190006-1)-(190006-4), 2017, doi: 10.1063/1.5016795.
- [64] K. E. Strawhecker and E. Manias, "Crystallization behavior of poly(ethylene oxide) in the presence of Na<sup>+</sup> montmorillonite fillers," *Chem. Mater.*, vol. 15, no. 4, pp. 844–849,

- 2003, doi: 10.1021/cm0212865.
- [65] Y. Li, Q. Ma, C. Huang, and G. Liu, "Crystallization of poly (ethylene glycol) in poly (methyl methacrylate) networks," *Mater. Sci.*, vol. 19, no. 2, pp. 147–151, 2013, doi: 10.5755/j01.ms.19.2.4430.
- [66] B. Crist and J. M. Schultz, "Polymer spherulites : A critical review," *Prog. Polym. Sci.*, vol. 56, pp. 1–63, 2016, doi: 10.1016/j.progpolymsci.2015.11.006.
- [67] G. Wypych, "Plasticizers Use and Selection for Specific Polymers," in *Handbook of Plasticizers*, 2nd ed., 2012, pp. 309–419.
- [68] R. N. Rethon, *Particulate Fillers for Polymers*, vol. 12, no. 9. Repra Technology Limited, 2002.
- [69] B. D. M. Matos *et al.*, "Evaluation of commercially available polylactic acid (PLA) filaments for 3D printing applications," *J. Therm. Anal. Calorim.*, vol. 137, no. 2, pp. 555–562, 2019, doi: 10.1007/s10973-018-7967-3.
- [70] V. Nagarajan, K. Zhang, M. Misra, and A. K. Mohanty, "Overcoming the Fundamental Challenges in Improving the Impact Strength and Crystallinity of PLA Biocomposites: Influence of Nucleating Agent and Mold Temperature," *ACS Appl. Mater. Interfaces*, vol. 7, no. 21, pp. 11203–11214, Jun. 2015, doi: 10.1021/acsami.5b01145.
- [71] S. K. (Harvard U. Bhatia and S. (Massachusetts I. of T. Sharma, "3D-Printed Prosthetics Roll Off the Presses," *Am. Inst. Chem. Eng.*, no. May, 2014.
- [72] K. S. Chung, D. A. Shin, K. N. Kim, Y. Ha, D. H. Yoon, and S. Yi, "Vertebral Reconstruction with Customized 3-Dimensional-Printed Spine Implant Replacing Large Vertebral Defect with 3-Year Follow-up," *World Neurosurg.*, vol. 126, pp. 90–95, 2019, doi: 10.1016/j.wneu.2019.02.020.
- [73] N. A. Chartrain, C. B. Williams, and A. R. Whittington, "A review on fabricating tissue scaffolds using vat photopolymerization," *Acta Biomater.*, vol. 74, pp. 90–111, 2018, doi: 10.1016/j.actbio.2018.05.010.
- [74] M. Sadia *et al.*, "Adaptation of pharmaceutical excipients to FDM 3D printing for the fabrication of patient-tailored immediate release tablets," *Int. J. Pharm.*, vol. 513, no. 1–2, pp. 659–668, 2016, doi: 10.1016/j.ijpharm.2016.09.050.
- [75] T. C. Okwuosa, D. Stefaniak, B. Arafat, A. Isreb, and K. Wan, "A Lower Temperature FDM 3D Printing for the Manufacture of Patient-Specific Immediate Release Tablets," *Pharm. Res.*, pp. 2704–2712, 2016, doi: 10.1007/s11095-016-1995-0.
- [76] A. Melocchi, F. Parietti, A. Maroni, A. Foppoli, A. Gazzaniga, and L. Zema, "Hot-melt extruded filaments based on pharmaceutical grade polymers for 3D printing by fused deposition modeling," *Int. J. Pharm.*, vol. 509, no. 1–2, pp. 255–263, 2016, doi: 10.1016/j.ijpharm.2016.05.036.
- [77] A. Goyanes *et al.*, "Fabrication of controlled-release budesonide tablets via desktop (FDM) 3D printing," *Int. J. Pharm.*, vol. 496, no. 2, pp. 414–420, 2015, doi: 10.1016/j.ijpharm.2015.10.039.
- [78] K. Pietrzak, A. Isreb, and M. A. Alhnan, "A flexible-dose dispenser for immediate and extended release 3D printed tablets," *Eur. J. Pharm. Biopharm.*, vol. 96, pp. 380–387, 2015, doi: 10.1016/j.ejpb.2015.07.027.
- [79] W. E. Katstra, R. D. Palazzolo, C. W. Rowe, B. Giritlioglu, P. Teung, and M. J. Cima, "Oral dosage forms fabricated by Three Dimensional Printing E," *J. Control. Release*, vol. 66, pp.

- 1–9, 2000.
- [80] S. A. Khaled, J. C. Burley, M. R. Alexander, J. Yang, and C. J. Roberts, “3D printing of five-in-one dose combination polypill with defined immediate and sustained release profiles,” *J. Control. Release*, vol. 217, pp. 308–314, 2015, doi: 10.1016/j.jconrel.2015.09.028.
- [81] S. A. Khaled, J. C. Burley, M. R. Alexander, and C. J. Roberts, “Desktop 3D printing of controlled release pharmaceutical bilayer tablets,” *Int. J. Pharm*, vol. 461, pp. 105–111, 2014.
- [82] J. Skowryra, K. Pietrzak, and M. A. Alhnan, “Fabrication of extended-release patient-tailored prednisolone tablets via fused deposition modelling (FDM) 3D printing,” *Eur. J. Pharm. Sci.*, vol. 68, pp. 11–17, 2015, doi: 10.1016/j.ejps.2014.11.009.
- [83] D. Wurster and J. Seitz, “Investigation of Drug Release from Solids III: Effect of a Changing Surface-Weight Ratio on the Dissolution Rate,” *J. Am. Pharm.*, vol. 49, no. 6, pp. 335–338, 1960.
- [84] M. D. Billy Dunn, “NDA Approval 207958,” 2015. [Online]. Available: [https://www.accessdata.fda.gov/drugsatfda\\_docs/applletter/2015/207958Orig1s000ltr.pdf](https://www.accessdata.fda.gov/drugsatfda_docs/applletter/2015/207958Orig1s000ltr.pdf).
- [85] M. K. Gupta *et al.*, “3D Printed Programmable Release Capsules,” *Nano Lett.*, vol. 15, no. 8, pp. 5321–5329, 2015, doi: 10.1021/acs.nanolett.5b01688.
- [86] H. Y. Karasulu and G. Ertan, “Different geometric shaped hydrogel theophylline tablets: Statistical approach for estimating drug release,” *Farmaco*, vol. 57, no. 11, pp. 939–945, 2003, doi: 10.1016/S0014-827X(02)01297-1.
- [87] A. Goyanes, P. Robles, A. Buanz, A. W. Basit, and S. Gaisford, “Effect of geometry on drug release from 3D printed tablets,” *Int. J. Pharm.*, vol. 494, no. 2, pp. 657–663, 2015, doi: 10.1016/j.ijpharm.2015.04.069.
- [88] A. Goyanes, A. B. M. Buanz, A. W. Basit, and S. Gaisford, “Fused-filament 3D printing (3DP) for fabrication of tablets,” *Int. J. Pharm.*, vol. 476, pp. 88–92, 2014, doi: 10.1016/j.ijpharm.2014.09.044.
- [89] K. Cheng, J. Zhu, X. Song, L. Sun, and J. Zhang, “Studies of Hydroxypropyl Methylcellulose Donut-Shaped Tablets,” *Drug Dev. Ind. Pharm.*, vol. 25, no. 9, pp. 1067–1071, 1999, doi: 10.1081/DDC-100102271.
- [90] Y. Zhou and X. Y. Wu, “Finite element analysis of diffusional drug release from complex matrix systems. I. Complex geometries and composite structures 1,” *J. Control. Release*, vol. 49, pp. 277–288, 1997.
- [91] J. P. Cleave, “Some geometrical considerations concerning the design of tablets,” *J. Pharm. Pharmacol.*, vol. 17, no. 11, pp. 698–702, 1965, doi: 10.1111/j.2042-7158.1965.tb07591.x.
- [92] B. K. Lee, Y. Hee, J. Suk, Y. Chan, J. Dong, and Y. Woo, “Fabrication of drug-loaded polymer microparticles with arbitrary geometries using a piezoelectric inkjet printing system,” *Int. J. Pharm.*, vol. 427, no. 2, pp. 305–310, 2012, doi: 10.1016/j.ijpharm.2012.02.011.
- [93] Y. Sun and S. Soh, “Printing Tablets with Fully Customizable Release Profiles for Personalized Medicine,” *Adv. Mater.*, vol. 27, pp. 7847–7853, 2015, doi: 10.1002/adma.201504122.
- [94] M. Schmitz, A. Leister, N. Dezfuli, J. Riemann, F. Müller, and M. Mühlhäuser, “Liquido:

- Embedding liquids into 3D printed objects to sense tilting and motion," *Conf. Hum. Factors Comput. Syst. - Proc.*, vol. 07-12-May-, pp. 2688–2696, 2016, doi: 10.1145/2851581.2892275.
- [95] T. C. Okwuosa, B. C. Pereira, B. Arafat, and M. Cieszynska, "Fabricating a Shell-Core Delayed Release Tablet Using Dual FDM 3D Printing for Patient-Centred Therapy," *Pharm. Res.*, pp. 427–437, 2017, doi: 10.1007/s11095-016-2073-3.
- [96] A. Maroni, A. Melocchi, F. Parietti, A. Foppoli, L. Zema, and A. Gazzaniga, "3D printed multi-compartment capsular devices for two-pulse oral drug delivery," *J. Control. Release*, vol. 268, no. October, pp. 10–18, 2017, doi: 10.1016/j.jconrel.2017.10.008.
- [97] A. Moon, P. Kashya, P. Takdhat, G. Jawalkar, and T. Anup, "Formulation and In-Vitro Characterization Of Calcitriol Soft Gelatin Capsule," *World J. Pharm. Res.*, vol. 7, no. 5, pp. 1590–1612, 2018, doi: 10.20959/wjpr20185-11346.
- [98] N. A. Meisel, A. M. Elliott, and C. B. Williams, "A procedure for creating actuated joints via embedding shape memory alloys in PolyJet 3D printing," *J. Intell. Mater. Syst. Struct.*, vol. 26, no. 12, pp. 1498–1512, 2015, doi: 10.1177/1045389X14544144.
- [99] D. Espalin, D. W. Muse, E. MacDonald, and R. B. Wicker, "3D Printing multifunctionality: Structures with electronics," *Int. J. Adv. Manuf. Technol.*, vol. 72, no. 5–8, pp. 963–978, 2014, doi: 10.1007/s00170-014-5717-7.
- [100] A. M. Gaikwad, G. L. Whiting, D. A. Steingart, and A. C. Arias, "Highly flexible, printed alkaline batteries based on mesh-embedded electrodes," *Adv. Mater.*, vol. 23, no. 29, pp. 3251–3255, 2011, doi: 10.1002/adma.201100894.
- [101] V. Iyer, J. Chan, and S. Gollakota, "3D printing wireless connected objects," *ACM Trans. Graph.*, vol. 36, no. 6, 2017, doi: 10.1145/3130800.3130822.
- [102] E. G. Gordeev, A. S. Galushko, and V. P. Ananikov, "Improvement of quality of 3D printed objects by elimination of microscopic structural defects in fused deposition modeling," *PLoS One*, vol. 13, no. 6, 2018, doi: 10.1371/journal.pone.0198370.
- [103] S. Sinha and N. A. Meisel, "Influence of Embedding Process on Mechanical Properties of Material Extrusion Parts," in *Solid Freeform Fabrication 2016*, 2016, pp. 847–863.
- [104] R. J. Zaldivar, D. B. Witkin, T. McLouth, D. N. Patel, K. Schmitt, and J. P. Nokes, "Influence of processing and orientation print effects on the mechanical and thermal behavior of 3D-Printed ULTEM® 9085 Material," *Addit. Manuf.*, vol. 13, pp. 71–80, 2017, doi: 10.1016/j.addma.2016.11.007.
- [105] E. G. Rippie and J. R. Johnson, "Regulation of Dissolution Rate by Pellet Geometry," *J. Pharm. Sci.*, vol. 58, no. 4, pp. 428–431, 1969.
- [106] K. Szykiedans, W. Credo, and D. Osiński, "Selected mechanical properties of PETG 3-D prints," *Procedia Eng.*, vol. 177, pp. 455–461, 2017, doi: 10.1016/j.proeng.2017.02.245.
- [107] S. R. G. Bates, I. R. Farrow, and R. S. Trask, "3D printed polyurethane honeycombs for repeated tailored energy absorption," *Mater. Des.*, vol. 112, pp. 172–183, 2016, doi: 10.1016/j.matdes.2016.08.062.
- [108] D. W. Hutmacher, T. Schantz, I. Zein, K. W. Ng, S. H. Teoh, and K. C. Tan, "Mechanical properties and cell cultural response of polycaprolactone scaffolds designed and fabricated via fused deposition modeling," *J. Biomed. Mater. Res.*, vol. 55, no. 2, pp. 203–216, 2001, doi: 10.1002/1097-4636(200105)55:2<203::AID-JBM1007>3.0.CO;2-7.
- [109] F. Ning, W. Cong, J. Qiu, J. Wei, and S. Wang, "Additive manufacturing of carbon fiber

- reinforced thermoplastic composites using fused deposition modeling,” *Compos. Part B Eng.*, vol. 80, pp. 369–378, 2015, doi: 10.1016/j.compositesb.2015.06.013.
- [110] S. J. Leigh, R. J. Bradley, C. P. Purssell, D. R. Billson, and D. A. Hutchins, “A simple, low-cost conductive composite material for 3D printing of electronic sensors,” *PLOS ONE*, vol. 7, no. 11, 2012, doi: 10.1371/journal.pone.0049365.
- [111] J. Gonzalez-Gutierrez, S. Cano, S. Schuschnigg, C. Kukla, J. Sapkota, and C. Holzer, “Additive manufacturing of metallic and ceramic components by the material extrusion of highly-filled polymers: A review and future perspectives,” *Materials (Basel)*, vol. 11, no. 5, 2018, doi: 10.3390/ma11050840.
- [112] Y. Choi, C. Kim, H. Jeong, and J. Youn, “Influence of bed temperature on heat shrinkage shape error in FDM additive manufacturing of the ABS-engineering plastic,” *World J. Eng. Technol.*, vol. 4, pp. 186–192, 2016, doi: 10.4236/wjet.2016.43D022.
- [113] W. Swanson, P. Turley, P. Leavitt, P. Karwoski, J. LaBossiere, and R. Skubie, “High temperature modeling apparatus,” US 6722872 B1, 2004.
- [114] C. Yang, X. Tian, D. Li, Y. Cao, F. Zhao, and C. Shi, “Influence of thermal processing conditions in 3D printing on the crystallinity and mechanical properties of PEEK material,” *J. Mater. Process. Technol.*, vol. 248, no. May, pp. 1–7, 2017, doi: 10.1016/j.jmatprotec.2017.04.027.
- [115] B. N. Turner and S. a. Gold, “A review of melt extrusion additive manufacturing processes: II. Materials, dimensional accuracy, and surface roughness,” *Rapid Prototyp. J.*, vol. 21, no. 3, pp. 250–261, 2015, doi: 10.1108/RPJ-01-2013-0012.
- [116] W. J. Swanson, P. W. Turley, P. J. Leavitt, J. Karwoski, Peter, J. E. Labossiere, and R. L. Skuble, “High-temperature modeling method,” US7,297,304 B2, 2007.
- [117] B. N. Turner, R. Strong, and S. a. Gold, “A review of melt extrusion additive manufacturing processes: I. Process design and modeling,” *Rapid Prototyp. J.*, vol. 20, no. 3, pp. 192–204, 2014, doi: 10.1108/RPJ-01-2013-0012.
- [118] P. Han, A. Tofangchi, A. Deshpande, S. Zhang, and K. Hsu, “An approach to improve interface healing in FFF-3D printed Ultem 1010 using laser pre-deposition heating,” *Procedia Manuf.*, vol. 34, pp. 672–677, 2019, doi: 10.1016/j.promfg.2019.06.195.
- [119] C. Sweeney, M. Green, and M. Saed, “Microwave-Induce localized heating of CNT filled polymer composites for enhanced inter-bead diffusive bonding of fused filament fabricated parts,” US 2016/0325491, 2016.
- [120] D. Ravoori, H. Prajapati, V. Talluru, A. Adnan, and A. Jain, “Nozzle-integrated pre-deposition and post-deposition heating of previously deposited layers in polymer extrusion based additive manufacturing,” *Addit. Manuf.*, vol. 28, no. January, pp. 719–726, 2019, doi: 10.1016/j.addma.2019.06.006.
- [121] L. Cherdo, “13 Professional PEEK 3D printers (Also ULTEM®, PEI and high-performance materials),” *Aniwaa Pte. Ltd*, 2018. <https://www.aniwaa.com/best-peek-3d-printer-pei-ultem/> (accessed Aug. 02, 2018).
- [122] Aon3D, “Aon3D AON-M2,” *aon3d Inc.*, 2018. <https://www.aon3d.com/> (accessed Apr. 18, 2018).
- [123] Apium, “Apium P220,” *Apium Additive Technologies GmbH*, 2018. .
- [124] INTAMSYS, “INTAMSYS Funmat HT,” *INTAMSYS TECHNOLOGY CO. LTD.*, 2017. <https://www.intamsys.com/> (accessed Aug. 01, 2018).

- [125] Oo-kuma, "Oo-kuma Katana." <http://www.oo-kuma.com/> (accessed Aug. 01, 2018).
- [126] Roboz, "Roboz One + 400," *Web agency BRAINPULL*, 2018. <https://www.roboze.com/en/> (accessed Aug. 01, 2018).
- [127] Rokit, "Rokit 3Dison AEP," *www.3disonprinter.com*. <http://en.3disonprinter.com/index.php> (accessed Aug. 01, 2018).
- [128] Stratasys, "Fortus 400mc," *Stratasys Ltd.*, 2018. <http://www.stratasys.com/> (accessed Aug. 01, 2018).
- [129] Tractus3D, "Tractus3D T650P," *Tractus3D*, 2018. <https://tractus3d.com> (accessed Aug. 01, 2018).
- [130] VeraShape VSHAPER Pro, "VSHAPER," *VSHAPER*, 2018. <http://vshaper.com/en/> (accessed Aug. 01, 2018).
- [131] H. Bheda and R. Reese, "Fused Filament Fabrication using liquid cooling," US2016/0271880 A1, 2016.
- [132] J. M. Gardner, C. J. Stelter, E. A. Yashin, and E. J. Siochi, "High temperature thermoplastic additive manufacturing using low-cost, open-source hardware," 2016. doi: 10.13140/RG.2.2.20690.15049.
- [133] R. Crockett, D. Petersen, and K. Cooper, "Fused Deposition Modeling in microgravity," *Solid Free. Fabr. Proc.*, pp. 671–678, 1999.
- [134] G. Wagner *et al.*, "Design and Development of a Multi-Tool Additive Manufacturing System," *Solid Free. Fabr. Proc.*, pp. 2005–2023, 2017.
- [135] Stratasys, "PPSF Production-grade thermoplastic for fortus 3D Printers." Stratasys Inc., 2017.
- [136] Stratasys, "Fortus 360mc/400mc 3D Production System User Guide." Stratasys Inc., 2014.
- [137] G. P. Radar, E. Resistivity, D. Forensic, R. Methods, and N. Ireland, "ASTM D638: Standard Test Method for Tensile Properties of Plastics." ASTM International, West Conshohocken, PA, 2015, doi: <https://doi.org/10.1520/C0186-15A>.
- [138] J. Seppala, K. E. Hillgartner, C. S. Davis, and K. Migler, "Thermography and weld strength characterization of thermoplastic 3D printing," *SPE ANTE Indianap.*, pp. 42–44, 2016.
- [139] "3DBenchy," 2016. <http://www.3dbenchy.com/> (accessed Aug. 01, 2018).
- [140] Stratasys, "ULTEM 1010 Resin," 2018, [Online]. Available: <https://www.stratasys.com/materials/search/ultem1010>.
- [141] J. M. Gardner, G. Sauti, J. Kim, R. J. Cano, and R. A. Wincheski, "Additive Manufacturing of Multifunctional Components Using High Density Carbon Nanotube Yarn Filaments," pp. 0–7, 2019.
- [142] H. Wu, M. Sulkis, J. Driver, A. Saade-castillo, A. Thompson, and J. H. Koo, "Multi-functional ULTEM™ 1010 composite filaments for additive manufacturing using Fused Filament Fabrication ( FFF )," *Addit. Manuf.*, vol. 24, no. October, pp. 298–306, 2018, doi: 10.1016/j.addma.2018.10.014.
- [143] A. Das *et al.*, "Current understanding and challenges in high temperature additivemanufacturing of engineering thermoplastic polymers," *Addit. Manuf.*, 2020, doi: <https://doi.org/10.1016/j.addma.2020.101218>.
- [144] T.-M. Wang, J.-T. Xi, and Y. Jin, "A model research for prototype warp deformation in the FDM process," *Int. J. Adv. Manuf. Technol.*, vol. 33, pp. 1087–1096, 2007, doi: 10.1007/s00170-006-0556-9.

- [145] N. Watanabe, M. L. Shofner, and D. W. Rosen, "Tensile Mechanical Properties of Polypropylene composites fabricated by material extrusion," pp. 633–646, 2017.
- [146] N. Watanabe, M. L. Shofner, N. Treat, and D. W. Rosen, "A Model for Residual Stress and Part Warpage Prediction in Material Extrusion with Application to Polypropylene," pp. 2437–2455, 2016.
- [147] M. Montero, S. Roundy, D. Odell, S. Ahn, and P. K. Wright, "Material Characterization of Fused Deposition Modeling ( FDM ) ABS by Designed Experiments," *Sicuettt if Manuf. Eng.*, pp. 1–21, 2001.
- [148] N. Aliheidari, J. Christ, R. Tripuraneni, S. Nadimpalli, and A. Ameli, "Interlayer adhesion and fracture resistance of polymers printed through melt extrusion additive manufacturing process," *Mater. Des.*, vol. 156, pp. 351–361, 2018, doi: 10.1016/j.matdes.2018.07.001.
- [149] E. L. Gilmer, C. Mansfield, J. M. Gardner, E. J. Siochi, D. G. Baird, and M. J. Bortner, "Characterization and Analysis of Polyetherimide: Realizing Practical Challenges of Modeling the Extrusion-Based Additive Manufacturing Process," *ACS Symp. Ser.*, vol. 1315, pp. 69–84, 2019, doi: 10.1021/bk-2019-1315.ch005.
- [150] C. Zawaski and C. Williams, "Design of a low-cost, high-temperature inverted build environment to enable desktop-scale additive manufacturing of performance polymers," *Addit. Manuf.*, vol. 33, no. February, 2020, doi: 10.1016/j.addma.2020.101111.
- [151] J. Bartolai, T. W. Simpson, and R. Xie, "Predicting strength of additively manufactured thermoplastic polymer parts produced using material extrusion," *Rapid Prototyp. J.*, vol. 24, no. 2, pp. 321–332, 2018, doi: 10.1108/RPJ-02-2017-0026.
- [152] S. Bhandari, R. A. Lopez-Anido, and D. J. Gardner, "Enhancing the interlayer tensile strength of 3D printed short carbon fiber reinforced PETG and PLA composites via annealing," *Addit. Manuf.*, vol. 30, 2019.
- [153] K. R. Hart, R. M. Dunn, J. M. Sietins, C. M. Hofmeister Mock, M. E. Mackay, and E. D. Wetzel, "Increased fracture toughness of additively manufactured amorphous thermoplastics via thermal annealing," *Polymer (Guildf.)*, vol. 144, pp. 192–204, 2018.
- [154] S. Rangisetty and L. D. Peel, "The effect of infill patterns and annealing on mechanical properties of additively manufactured thermoplastic composites," pp. 1–12, 2017.
- [155] R. P. Wool, B.-L. Yuan, and O. J. McGarel, "Welding of Polymer Interfaces," *Polym. Eng. Sci.*, vol. 29, no. 19, pp. 1340–1367, 1989.
- [156] S. H. Ahn, C. S. Lee, and W. Jeong, "Development of translucent FDM parts by post-processing," *Rapid Prototyp. J.*, vol. 10, no. 4, pp. 218–224, 2004, doi: 10.1108/13552540410551333.
- [157] D. T. Nguyen *et al.*, "3D-Printed Transparent Glass," vol. 1701181, pp. 1–5, 2017, doi: 10.1002/adma.201701181.
- [158] M. E. Mackay, Z. R. Swain, C. R. Banbury, D. D. Phan, and D. A. Edwards, "The performance of the hot end in a plasticating 3D printer," *J. Rheol. (N. Y. N. Y.)*, vol. 61, no. 2, pp. 229–236, 2017, doi: 10.1122/1.4973852.